TECHNICAL AND ECONOMIC INTEGRATION OF VOLTAGE SOURCE CONVERTER BASED HIGH VOLTAGE DIRECT CURRENT TRANSMISSION IN POWER SYSTEMS

A Dissertation

by

OMAR ARMANDO URQUIDEZ

Submitted to the Office of Graduate and Professional Studies of
Texas A&M University
in partial fulfillment of the requirements for the degree of

DOCTOR OF PHILOSOPHY

Chair of Committee,	Le Xie
Committee Members,	B. Don Russell
	Steven Puller
	Jose Silva-Martinez
Head of Department,	Miroslav Begovic

May 2016

Major Subject: Electrical Engineering

ABSTRACT

New challenges face the electrical system everyday. These new challenges may need to be addressed with more than just conventional AC solutions. Voltage Source Converter based High Voltage DC (VSC-HVDC) systems, although unconventional, may provide promising solutions to these challenges, but integration of these advanced devices into normal power system planning and operation continues to be slow. This research seeks to improve integration of VSC-HVDC into power system planning and operations by addressing both the technical and economic hurdles to integration.

First, a ranking algorithm of prioritizing the incorporation of a VSC-based HVDC transmission line for improved economic dispatch is presented. This algorithm, termed as Smart Targeted Planning (STP), proposes a line shadow price-based weighting approach to ranking the potential economic impact of incorporating a new VSC-based HVDC link along existing transmission lines. This work allows for improved integration of VSC-HVDC in the planning stages.

Second, a singular value sensitivity (SVS) based supplementary control algorithm is proposed for enhancing the quasi-steady-state voltage stability in AC power systems. The algorithm computes the optimal control policy for VSC power so that the system voltage stability margin is maintained. Also introduced is the singular value capability space of the embedded VSC-HVDC system which builds intuition for system operators to visualize how much the embedded VSC-HVDC system can migrate the system away from voltage instability.

Third, a novel control algorithm is proposed for power system small signal dy-

namic performance improvement by use of an embedded voltage source converter (VSC) based high voltage direct current (HVDC) system. Embedded HVDC refers to a meshed AC grid with all HVDC terminals connected within the same AC grid. The concept of steady-state and dynamic impedance of the HVDC system is introduced as a novel time-scale separation of the impact of HVDC on the AC grid. In this system, the impedance of the connecting transmission lines is the same in the dynamic model as that in the steady-state model. The proposed control will have the VSC-HVDC mimic impedance in the dynamic model while not affecting the steady-state model. This allows the VSC-HVDC system to target improvement for dynamic problems while maintaining independence to use a different control to improve steady-state problems. To obtain optimal parameters for the enhanced small signal impedance mimicry (ESSIM) control, a sensitivity based optimal control loop is also proposed. The efficacy of the proposed algorithm is shown via case studies on a classic two area system and on the IEEE 10 generator 39 bus system.

Finally, a multi-time scale techno-economic benefit mapping framework is proposed to aid in better economic integration of advanced transmission devices like VSC-HVDC. The proposed approach is to clearly map technical benefits to their corresponding economic causes and economic effects. The end result will be a scalar metric by which all devices can be compared. The proposed approach will address multi-time scale technical benefits and the resulting economic causes and effects providing clarity, transparency, and granularity to allow for a better one-to-one comparison of conventional and unconventional power system devices.

DEDICATION

To my parents who toiled in the agricultural fields of West Texas to give my brothers and me the opportunities they themselves were denied and to my beloved wife Marleni who knows, loves, supports and understands me more than anyone has in my life.

ACKNOWLEDGEMENTS

My sincerest thanks goes out to my committee members, Dr. B. Don Russell, Dr. Steven Puller, and Dr. Jose Silva-Martinez for their aid and guidance as part of my advisory committee. I would also like to thank my research colleagues, Yang Chen, Xinbo Geng, Meng Wu, Sadegh Modarresi, Chen Yang, James Carroll, Hiawang Zhong, Xiaowen Lai, and Yang Bai for their support as academics and most importantly as friends. A special thanks goes out to Dr. Anupam Thatte and Dr. Yingzhong Gu, or as I know them, Anupam and Gary. The example they set for our young academic research group is worth more than can be described with words. They have had and will continue to have a lasting effect on those of us that came after them.

I would also like to show my appreciation to ABB Corporate Research for their monetary support during my phd research. Also much gratitude goes out to several industry leaders for their personal and academic support, most especially to Dr. Le Tang of ABB Inc., Dr. Wayne Galli of Clean Line Energy Partners, and Neil Kirby of Alstom Grid Inc.

Finally, my highest appreciation goes out to my advisor, my mentor and my dearest friend, Dr. Le Xie. His wisdom and kindness is unparalleled. He helped me to grow not only as an academic but even more so as a person. I am lucky to have met and been apart of the great things he is and will continue to achieve.

TABLE OF CONTENTS

LIST OF FIGURES

FIGURE Page

LIST OF TABLES

TABLE Page

1. INTRODUCTION*

1.1 Motivation and Overview

In the last decade local, state, and national policies have driven renewable energy development such that its penetration in electrical power markets has skyrocketed. Much of the new renewable energy production has come from the development of large wind and solar projects. These energy sources pose three grand challenges to large power system operation.

1. These types of sources come with increased power variability. This variability in the longer term (diurnal time frame) causes variability in system characteristics like flow congestion patterns, quasi-steady-state voltage stability and small signal stability.

2. Large renewable energy projects tend not to be near the load centers they serve. This is tasking the long distance transmission infrastructure and pushing stability margins.

3. Wind and solar installations utilize numerous power electronic controllers. Recent literature suggests that these control systems are exacerbating power system problems like subsynchronous resonance and inter-area oscillation phenomena.

*This section is in part a reprint of the material in the following papers: (1) Reprinted with permission from O. A. Urquidez and L. Xie, "Smart Targeted Planning of VSC-Based Embedded HVDC via Line Shadow Price Weighting," *IEEE Transactions on Smart Grid*, vol. 6, no. 1, pp. 431-440, Jan. 2015. Copyright 2015, IEEE. (2) Reprinted with permission from O. A. Urquidez and L. Xie, "Singular Value Sensitivity Based Optimal Control of Embedded VSC-HVDC for Steady-State Voltage Stability Enhancement," *IEEE Transactions on Power Systems*, vol. 31, no. 1, pp. 216-225, Jan. 2016. Copyright 2016, IEEE.

These new challenges need to be addressed with more than just conventional AC solutions. Voltage Source Converter based High Voltage DC (VSC-HVDC) systems although unconventional, may provide promising solutions to these challenges but integration of these advanced devices into normal power system planning and operation continues to be slow. This research, motivated by the challenges described, seeks to improve integration of VSC-HVDC into power system planning and operations by addressing both the technical and economic hurdles to integration.

1.2 Major Contributions

This research seeks to contribute to improved power system operation and control by providing a holistic approach to better integration of VSC-HVDC in the following ways:

- Increased clarity in system planning for VSC-HVDC by providing a multi-time scale techno-economic mapping framework taking into account various technical features.
- Improved integration of VSC-HVDC into standard planning practices by the creation of a smart targeting algorithm for VSC-HVDC.
- Enhanced system wide quasi-steady-state voltage stability through a proposed supplementary control algorithm for VSC-HVDC.
- Strengthened system wide small signal stability pertaining to inter-area oscillation dampening via intelligent, time-scale specific control of VSC-HVDC.

1.3 Dissertation Outline

The rest of this dissertation is organized as follows.

Chapter 2 presents a novel approach to incorporating voltage source converter (VSC)-based embedded high voltage DC for improving power system economic dispatch efficiency. It presents an analytical formulation to quantify the economic benefits of embedded HVDC by modeling its flow control as an injection-extraction pair in the economic dispatch of the transmission grid. A computationally efficient algorithm is proposed to rank the potential locations of such embedded HVDC. The algorithm is based on expected economic dispatch cost reduction weighted by the historical line shadow prices. The use of a distribution of historical data as a means of weighting also allows for incorporation of diurnal & seasonal influences on congestion patterns. Numerical case studies using the proposed method of locating the embedded HVDC suggest promising results in choosing the location of improved flow control devices.

Chapter 3 presents a novel control algorithm for improving steady-state (quasi-static) voltage stability by use of an embedded Voltage Source Converter (VSC) based High Voltage Direct Current (HVDC) system. Embedded HVDC refers to a meshed AC system with all HVDC terminals connected within the same AC grid. The sensitivity between VSC control input and the voltage stability margin is introduced. Based on this sensitivity, the proposed control algorithm jointly satisfies system-wide voltage stability margin as well as local voltage magnitude requirements. The proposed approach is to first migrate the entire system to have sufficient voltage stability margin, and then to correct any voltage magnitude violation while keeping that stability margin. A contour-based visualization of the VSC capability space for maintaining system voltage stability is introduced, which can effectively illustrate how the singular value sensitivity (SVS) based control achieves both the local and global voltage stability requirements. The efficacy of the proposed algorithm is shown via case studies on a 6 bus and 118 bus system with and without static VAR

compensation.

Chapter 4 presents a novel control algorithm for power system small signal dynamic performance improvement by use of an embedded voltage source converter (VSC) based high voltage direct current (HVDC) system. Embedded HVDC refers to a meshed AC grid with all HVDC terminals connected within the same AC grid. The concept of steady-state and dynamic impedance of the HVDC system is introduced as a novel time-scale separation of the impact of HVDC on the AC grid. In this system, the impedance of the connecting transmission lines is the same in the dynamic model as that in the steady-state model. The proposed control will have the VSC-HVDC mimic impedance in the dynamic model while not affecting the steady-state model. This allows the VSC-HVDC system to target improvement for dynamic problems while maintaining independence to use a different control to improve steady-state problems. To obtain optimal parameters for the enhanced small signal impedance mimicry (ESSIM) control, a sensitivity based optimal control loop is also proposed. The efficacy of the proposed algorithm is shown via case studies on a classic two area system and on the IEEE 10 generator 39 bus system.

Chapter 5 presents a proposed approach to clearly map multi-time scale technical benefits to their corresponding economic causes and economic effects. This will provide clarity, transparency, and granularity allowing for a better one to one comparison of advanced transmission devices. This improved one to one comparison on multiple times scales will aid in the integration of such advanced transmission devices into normal system planning and operation. To illustrate the techno-economic mapping framework, combinations of Technical Features are chosen to create technical cases. The results of these technical cases are presented and discussed in this chapter.

In Chapter 6, the output of the analysis in Chapter 5 is applied to the basic

economic dispatch. By first applying the technical features analyzed in Chapter 5 and then filtering those results through the given standard market system (in this case economic dispatch) the multi-time scale technical abilities of the given advanced transmission device can be translated into an economic effect. This allows devices that render multi-time scale technical benefits to be faithfully compared to other devices without the need for markets for each time scale. Several economic cases studies illustrating this concept are presented and discussed in this chapter.

Chapter 7 summarizes the conclusions of the research and discusses possible directions for further research in the future.

2. SMART TARGETED LOCATING OF VSC BASED EMBEDDED HVDC VIA LINE SHADOW PRICE WEIGHTING*

2.1 Introduction

This chapter is motivated by the need for better transmission planning algorithms that address new planning objectives, incorporate new flexible transmission devices and do so in a more computationally efficient manner.

The objective of transmission planning has changed over the long history of electrical power system development in the United States. The earliest planning objective was to simply increased access as illustrated by early papers focused on nuances of subtransmission that could provide increased access [10, 11]. In the 1970s, optimization techniques were applied to transmission planning that helped to weigh competing interests of functionality and construction costs [12, 13]. The cost of transmission losses were included in the 1980s as was the consideration of net present value of costs and benefits [14, 15, 16]. More recently, even more complex cost objective functions were added that included reliability based value. Reference [17] values this reliability as unserved energy costs. It is valued similarly in [18] in that the reliability is considered as customer outage costs. Chowdhury and Koval took a previously unconsidered approach and value the reliability component using customer survey results [19].

The most recent transmission planning objectives have been in quantifying and including the value of transmission planning results that come from effects seen in competitive markets [20]. This has also been driven by policy implementations such

*This section is in part a reprint of the material in the following papers: (1) Reprinted with permission from O. A. Urquidez and L. Xie, "Smart Targeted Planning of VSC-Based Embedded HVDC via Line Shadow Price Weighting," *IEEE Transactions on Smart Grid*, vol. 6, no. 1, pp. 431-440, Jan. 2015. Copyright 2015, IEEE.

as the Federal Energy Regulatory Commission (FERC) Order 1000 [21]. The norm before this order was to have a socialized cost approach to funding for transmission projects [22]. In many systems, these socialized costs were shared by generators or loads or a combination of the two collective entities. FERC Order 1000 mandates, among other things, that transmission planners quantify which entities benefit economically from transmission projects. It also mandates project costs be allocated to entities that benefit in proportion to how much they benefit. The Electric Reliability Council of Texas (ERCOT) now has a pathway for transmission planning justification based solely on economic criteria [23], which is becoming an industry trend.

Even though the objective has evolved, one thing has been consistent, these approaches have been optimization based. Methods have combined linear programming, dynamic programming, mixed integer programming, and heuristics. Although these methods have been continually advanced, they are all still limited by computational burden when applied to large systems.

Also recently, as flexible transmission devices like FACTS devices and HVDC have become realistic transmission planning alternatives to more wires and capacitor backs, transmission planning methods are moving to include them. The authors in [24] incorporate optimal FACTS device sizing and location for reactive power planning. Kuruganty and Woodford include LCC based HVDC in reliability based transmission planning [25]. These approaches are revisiting different objectives while including new devices choices.

Several observations emerge from the preceding discussion that motivate this work:

1. The transmission planning objective has evolved and it must now include eco-

nomic impacts in competitive markets.

2. The optimization approaches in the mentioned literature suffer from computational burden.

3. Transmission planning methods must now also include flexible transmission devices as they are becoming viable and sometimes necessary alternatives.

The Smart Targeted Planning (STP) method proposed centers its objective on economic impacts, which as discussed, is the newest of the objectives in transmission planning. STP also focuses on a flexible transmission device, the VSC based embedded HVDC system, which has been receiving much more attention in recent literature. Most importantly, the proposed algorithm uses a non-optimization based method and therefore does not suffer from computational burden.

The chapter is organized as follows. In Section II, the foundation for the STP algorithm is formulated. In Section III, the STP algorithm is presented based on the DC load flow approximation which results in the distribution factor matrix. From this an equation for Flexible Line System Capacity (FLSC) is derived. This is weighted by historical shadow price information to produce an expected net system dispatch cost change. Section IV provides the results and analysis of the numerical testing on an ERCOT Simplified 24 bus system and the IEEE 118 bus system. Concluding remarks and future work are suggested in Section V.

2.2 Problem Formulation

2.2.1 DC Power Flow Approximation

The problem formulation is similar to that in [26]. Fig. 2.1 shows the classic two bus system. The complex power flow for this system is described as the following:

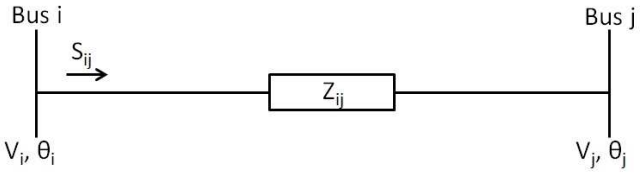

Figure 2.1: Simple Two Bus System.

$$S_{ij} = V_i I_{ij}^* = V_i (\frac{V_i - V_j}{Z_{ij}})^* \tag{2.1}$$

Under the assumption that (1) lines are lossless; (2) voltage magnitudes at all buses are around 1 per unit, and (3) phase angle difference between buses are relatively small, the nonlinear power flow equation can be linearized as the DC power flow:

$$F = diag(b) \cdot A^T \cdot \theta \tag{2.2}$$

The vector of real power injections and the DC power flow is related by the following equation:

$$F = diag(b) \cdot A^T \cdot B_R^{-1} \cdot P \tag{2.3}$$

The compact matrix form of the equation is:

$$F = H \cdot P \tag{2.4}$$

2.2.2 SCED Formulation

The security constrained economic dispatch (SCED) problem is formulated as a linear optimization as shown below:

$$C_{ED} = \min \sum_{i \in G} C_{Gi}(P_{G_i}) \tag{2.5}$$

s.t.

$$P_{Gi}^{min} \leq P_{Gi} \leq P_{Gi}^{max} \tag{2.6}$$

$$F_{Li}^{min} \leq F_{Li} \leq F_{Li}^{max} \tag{2.7}$$

$$\sum P_{Gi} = \sum P_{Di} \tag{2.8}$$

The objective is to minimize the cost of real power produced with respect to the cost functions of each generator. The cost functions used are constant marginal cost functions. Since it is a dispatch problem the set of generators committed for dispatch is assumed fixed. Start up and shut down costs are not considered. The optimization is subject to the equality constraint of real power balance. The optimization is also subject to several inequality constraints such as the real power minimums and maximums of each generator and the real power flow limits of each line.

2.2.3 VSC Model

For this work a VSC based HVDC link will be the fundamental unit of flow control that will be incorporated in the DCOPF based SCED. The VSC converter will be treated as a black box similar to that discussed in [1]. Fig. 2.2 shows a diagram of the black box VSC with respect to real power flow used in [1].

The VSC converter produces an AC voltage waveform at U_{conv}. If this waveform

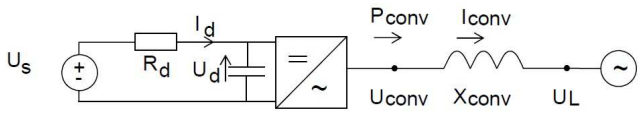

Figure 2.2: Black Box Diagram of VSC Converter for Real Power Flow [1].

is considered in the same way as a voltage source generator the interaction of U_{conv} to U_L is similar to that of the two bus system described in Section II. This means that real power flow from the VSC converter can be described as:

$$P_{conv} = \frac{U_{conv}U_L sin(\theta_{conv,L})}{X_{conv}} \tag{2.9}$$

If the same lossless DC approximation is applied, where it is assumed that $U_{conv} \cong U_L \cong 1$ and $\theta_{conv,L}$ is small, P_{conv} becomes:

$$P_{conv} = b_{conv} \cdot \theta_{conv,L} \tag{2.10}$$

The angle, $\theta_{conv,L}$, is controllable by the VSC converter and thus so is P_{conv}. . The control strategy of the VSC-HVDC link is real power flow control. The link is considered a lossless line so the real power injected at the converter in inverter mode is equal to the real power extracted by the converter acting in rectifier mode but with opposite sign at all times as shown in (4.19).

$$P_I = -P_E \tag{2.11}$$

Fig. 2.3 shows a diagram of the black box VSC with respect to reactive power flow used in [1]. The equation for Q_{conv}, shown in Fig. 2.3 can be developed in a similar fashion from the two bus system in Section II as:

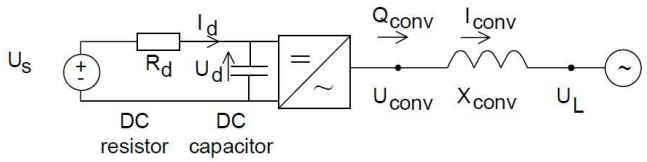

Figure 2.3: Black Box Diagram of VSC Converter for Reactive Power Flow [1].

$$Q_{conv} = \frac{U_{conv}U_L cos(\theta_{conv,L})}{X_{conv}} - \frac{U_{conv}^2}{X_{conv}} \tag{2.12}$$

If the same lossless DC approximation is applied, where it is assumed that $U_{conv} \cong U_L \cong 1$ and $\theta_{conv,L}$ is small, Q_{conv} becomes:

$$Q_{conv} = 0 \tag{2.13}$$

From a system perspective this means that the reactive power is treated as a net zero interaction with the existing AC system. The injection and extraction of real power by the VSC based HVDC link is also treated as a fully controllable real power source limited only by the size of the HVDC link and subject to the constraint (4.19). For the SCED formulation, P_I and P_E are treated as a real power generator and real power load.

$$P_I = P_{G,DC} \tag{2.14}$$

$$P_E = P_{L,DC} \tag{2.15}$$

2.3 Smart Targeted Planning

2.3.1 Flexible Line System Capacity

The addition of a controllable flow element like a VSC HVDC link can be used as a means to control flow patterns on the existing AC system. The change in flow patterns due to the controllable flow of the HVDC link can be considered as flexible line capacity for each affected line. The system effect is termed Flexible Line System Capacity (FLSC).

For a system in a given dispatch state, the flow on each line in the system is described in (4.12). The presence of the HVDC link does not affect the distribution factor matrix, H. The real power injection vector P is changed by the controlled flow of the HVDC link. The following vectors represent this change.

$$P_{INJ} = \begin{bmatrix} 0 \\ P_I \\ \vdots \\ 0 \\ 0 \end{bmatrix}, P_{EXT} = \begin{bmatrix} 0 \\ \vdots \\ P_E \\ 0 \\ 0 \end{bmatrix} where, P_I = -P_E \tag{2.16}$$

So, the change in flow due to the flow on the HVDC link is as follows:

$$\Delta F_f = H \cdot (P_{INJ} + P_{EXT}) \tag{2.17}$$

Eq. (4.25) defines FLSC, a flexible capacity that can be utilized in each dispatch to relax the line flow constraints optimally in each interval.

To investigate the FLSC for all possible existing connections a matrix of injection-

extraction pairs can be used in place of the singular column vector used in (4.25). The reduced incidence matrix of the system is just this matrix of all possible existing connections. So (4.25) becomes,

$$\Delta F_F = H \cdot P_{L\_P} \quad where, \;\; P_{L\_P} = A \tag{2.18}$$

2.3.2 Historical Shadow Price Weighting

To result in a market impact the FLSC can be seen as a tool to provide a set of possible solutions around a historical operating point that is still within constraints. The set is then weighted by the sensitivity metric of shadow prices to arrive at a system dispatch cost delta provided by the FLSC attributable to the flow control upgrade in question. The vector μ, is the shadow price vector which is a result of the original dispatch. It signifies the expected change in dispatch cost to a change in a constraint. The portion of this vector that corresponds to line flow constraints is the shadow price vector for transmission lines. It can be used to weight the FLSC to quantify the effect the HVDC line flow has on system dispatch cost as shown below:

$$\Delta C_{tot} = \mu \cdot \Delta F_f \tag{2.19}$$

Eq. (4.27) can be augmented using (4.26) to give the vector $\Delta C_{TOT,int}$ in (4.28), which represents the cost delta due to the added FLSC for all branches in the system for a particular interval.

$$\Delta C_{TOT,int} = \mu_{int} \cdot \Delta F_F \tag{2.20}$$

The shadow price of a particular interval fully describes the value to the system

for the full duration of the interval, but it cannot describe the value outside of that binding duration. Shadow prices for each interval must be applied only that interval. Diurnal and seasonal patterns will produce differing shadow prices which will in turn produce differing cost deltas. To account for that, the vector $\Delta C_{TOT,int}$ should be summed for all intervals in the year producing $\Delta C_{TOT,yr}$.

$$\Delta C_{TOT,yr} = \sum_{k=1}^{T} \Delta C_{TOT,k} \tag{2.21}$$

Eq. (4.29) yields a vector of cost deltas due to FLSC taking into account diurnal and seasonal patterns. The larger the cost delta is the larger the market impact will be. This vector can then be sorted to provide the upgrade candidates with the maximum market impact.

2.3.3 Application of Smart Targeted Planning

The STP method begins with a dispatch result which will provide the dispatch cost and the shadow price vector, μ. This means that for whatever the planning horizon is, one year, five years, ten years, etc., an initial dispatch must be run that does not include the VSC based embedded HVDC line. The STP method is applied to the information from this original dispatch and a set of predicted cost decreases for each year in the planning horizon, $\Delta C_{TOT,yr}$, is produced. The highest decrease values from this set will point to a candidate set for a redispatch of the system. This redispatch would include the HVDC line and would be run for the whole planning horizon.

The straight forward alternative to the STP method for locating the HVDC line addition is through an Exhaustive Heuristic Search (EHS). This means a dispatch for the planning horizon (one, five, ten years, etc.) would be completed for each possible

location. This is computationally very expensive for long-term planning issues. Thus intuition and experience would be used to produce a candidate set for trials which is not quite thorough and may miss better non-intuitive options. All these reasons speak to the key advantage of the STP method.

2.3.4 Multi-Terminal VSC based Embedded HVDC Systems

Multi-terminal VSC based embedded HVDC systems are a logical extension of the single line two terminal system discussed in this work. Recent projects in the United States such as the Mid-Atlantic Power Pathway Project, the Champlain Hudson Power Express Project, and the Tres Amigas project are of the multi-terminal structure [27][28]. With the exception of the Tres Amigas, these projects are also embedded systems. Although many of the current systems of this configuration are driven by technical necessity, the economic impact is important in micro-siting. It is also possible that with advancement in planning techniques that include devices like VSC based embedded HVDC, like the STP method, that more projects will be identified with economic drivers that are stronger than their technical drivers. The STP method is easily generalizable to include multi-terminal VSC based embedded HVDC systems. When multi-terminals are considered (4.24) becomes (4.30)-(4.31).

$$P_A = \begin{bmatrix} 0 \\ P_a \\ \vdots \\ 0 \\ 0 \end{bmatrix}, P_B = \begin{bmatrix} 0 \\ \vdots \\ P_b \\ 0 \\ 0 \end{bmatrix}, P_C = \begin{bmatrix} 0 \\ 0 \\ \vdots \\ P_c \\ 0 \end{bmatrix} \cdots \tag{2.22}$$

where,

$$0 = P_a + P_b + P_c \ldots \tag{2.23}$$

The rest of the STP method derivation follows in the same way as with the two terminal system. The application in the planning process is also the same.

2.3.5 Smart Targeted Planning with Converter Losses

A key advantage of the STP method is built in to how it weights the flexible line capacity provided by the VSC based embedded HVDC system. The shadow price holds information pertinent to all aspects included in the base dispatch. This means that although in this chapter a simple SCED formulation is utilized a SCED formulation that includes more complex aspects in either the objective function or constraints can be easily substituted and the STP method will still perform as expected. Effects of the inclusion of complex aspects such as line losses, ramp constraints, and others will be represented in the shadow prices used to weight the flexible line capacity. So in general, as long as the complexity of a SCED formulation is represented in the base dispatch, the STP method will be able to account for its effects in the results.

One aspect that would not be available in the base dispatch is the impact of losses in the converters. While early technology used in VSC based embedded HVDC systems had significant losses on the order of 3 to 4% [29], recent technologies show losses in converter stations of less than 1% [30]. This means that for the full power transfer that includes all associated converter stations the total losses are on the order of system line losses. Thus, if a simplification of a lossless system is used, this too can be applied to the losses by the VSC based embedded HVDC system. If losses are to be included in the rest of the system they must also be included for the VSC based embedded HVDC system and thus the STP must be augmented slightly to

account for them.

To account for conversion losses (4.27) becomes (4.36).

$$\Delta C_{tot} = \begin{cases} \mu \cdot \Delta F_f - \lambda^T |a| LF & : \mu \cdot \Delta F_f > \lambda^T |a| LF \\ 0 & : \mu \cdot \Delta F_f \leq \lambda^T |a| LF \end{cases} \tag{2.24}$$

The term $\lambda^T |a| LF$ in (4.36) represents the cost of losses modeled as additional load at the terminal priced at the LMP at the bus the terminal is connected to. This is achieved by using the full incidence matrix, a, weighted by the loss factor, LF, at a price represented by the LMP vector, λ.

Subsequently, (4.28) and (4.29) change accordingly.

2.4 Numerical Examples

2.4.1 ERCOT Modeled 24 Bus System

2.4.1.1 Transmission Grid

In previous work [31], a 24 bus system modeled after the ERCOT transmission system, first introduced in [32], is utilized . This system will again be utilized and is shown in Fig. 2.4. The system has 24 buses and 32 single line branches. It is divided into four zones representing the old North, South, West, and Houston zones in the zonal system pre-2010. The zones are connected by 8 interzonal single line branches. Five of the eight interzonal lines have line limits. Since the original use for this system was an investigation on interzonal congestion all other lines except these five have no line limits. The flow patterns of the system are modeled off of the ERCOT published interzonal shift factors.

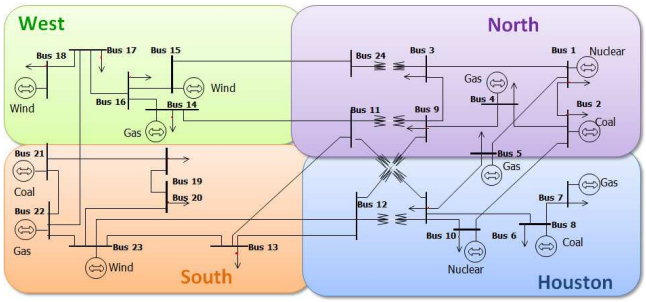

Figure 2.4: ERCOT Simplified 24 Bus Model.

2.4.1.2 Load and Generation

The generation capacity, type and zonal location are also modeled after published data [33] and represented by 13 generators, three of which are wind generators. The load zone amounts and locations are modeled after a 'typical' day and include a diurnal pattern. The 'typical' day is characterized by its peak load of 60,000MW. To extrapolate this load pattern for a yearlong study, the weekly load percentage given in the description of the IEEE RTS 96 [9] is used to scale the load pattern. It is reproduced in Table 2.1. These 52 week data points are then combined to create 12 'typical' monthly diurnal load profiles. For instance, the 'typical' day has a peak load which is 88% of ERCOTs system high [34]. This would correspond to week 30 in Table II of [9] which is averaged with the values of week 26 through 29 to produce the 'typical' day for the month of March. Every other month is scaled accordingly. Simulations on 'typical' days for all 52 weeks were contemplated but although the STP algorithm runs very quickly, the Exhaustive Heuristic Search (EHS) trials take prohibitively long to run. This method of scaling to produce 'typical' days allows for a very good, though not perfect, approximation of both diurnal and seasonal load patterns.

Table 2.1: 52 Week Peak Load[9]

Week	Peak Load	Week	Peak Load
1	86.2	27	75.5
2	90	28	81.6
3	87.8	29	80.1
4	83.4	30	88
5	88	31	72.2
6	84.1	32	77.6
7	83.2	33	80
8	80.6	34	72.9
9	74	35	72.6
10	73.7	36	70.5
11	71.5	37	78
12	72.7	38	69.5
13	70.4	39	72.4
14	75	40	72.4
15	72.1	41	74.3
16	80	42	74.4
17	75.4	43	80
18	83.7	44	88.1
19	87	45	88.5
20	88	46	90.9
21	85.6	47	94
22	81.1	48	89
23	90	49	94.2
24	88.7	50	97
25	89.6	51	100
26	86.1	52	95.2

2.4.1.3 Analysis

Fig. 2.5 compares the results of the Exhaustive Heuristic Search (EHS) versus the results of the STP. Some lines show large decreases in dispatch cost like lines 18 and 27 while others show very little dispatch cost decrease like lines 26 and 12. Even though the absolute numbers differ, both the STP and EHS methods produce sets of lines that begin to separate in terms of their impact on system dispatch cost.

One way to look at the results would be to group the sets according to their dispatch cost impact. For instance, if an upgrade is only feasible with a yearly payback of above $500,000 then the set would consist of 13, 14, 15, 17, 18, 22, 24, and 27. If the threshold were instead $1,000,000, then the candidate set would be 17, 18, 24, and 27. EHS would take an immense amount of time to produce these candidate sets. On the other hand STP, using historical data already produced, could quickly and easily provide these candidates sets which would then be investigated more thoroughly. For the results, no particular threshold is called for so the top ten cost decrease candidates will be analyzed closer.

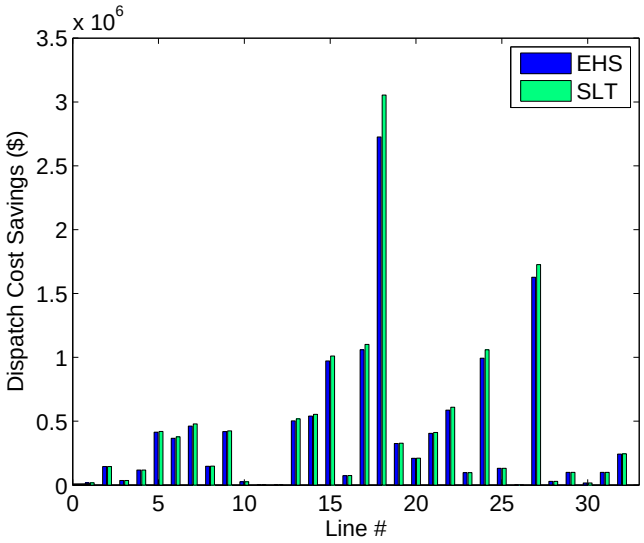

Figure 2.5: STP versus EHS Full Year Dispatch Cost Decrease.

The top ten line candidates that produce the greatest dispatch cost decrease are presented in Table 2.2. It is important to see that both the EHS and STP methods produced the same top ten candidates for flow control.

Intuition would suggest that the flow control upgrade should come on a congested

Table 2.2: Top Ten Flow Control Candidates

EHS			STP			
Rank	Line #	Savings ($)	Rank	Line #	Savings ($)	% diff
1	18	2,726,337	1	18	3,053,666	12.01
2	27	1,627,402	2	27	1,725,805	6.05
3	17	1,059,332	3	17	1,101,277	3.96
4	24	993,804	4	24	1,059,181	6.58
5	15	971,303	5	15	1,010,896	4.08
6	22	587,265	6	22	609,244	3.74
7	14	540,162	7	14	554,225	2.61
8	13	502,152	8	13	519,097	3.37
9	7	461,766	9	7	478,597	3.64
10	9	418,660	10	9	423,885	1.25

corridor line. The congested corridor lines in this system are 5, 9, 17, 18, and 24. Contrary to intuition Table 2.2 shows that line 27 which is not in the set of corridor lines is the second most effective upgrade. Also contrary to intuition, corridor line 5 is not even in the top ten whereas lines not in the congested corridor list such as 15, 22, 14, 13, and 7 together with line 27 as mentioned before, round out the top ten.

2.4.1.4 STP and EHS Result Differences

As seen in both Fig. 2.5 and Table 2.2, the STP method does not produce the exact same absolute results as the EHS method. Both the STP and EHS methods agree that the largest decrease in dispatch cost will come from a flow control upgrade of line 18. The difference between the result from STP and the result from EHS is about 12%. The other top ten candidates have a difference ranging from 6.58% to 1.25%. This is an acceptable error during a pre-planning period where a set of candidates is more important than an exact dispatch cost decrease.

Fig. 2.6 and Fig. 2.7 show the same information as Fig. 2.5 for January and July. In January, discrepancies exist between the results of the STP and EHS methods for

a number of lines but no difference is more pronounced than that for line 18. The difference is over 100%. Conversely in July, there is exactly no difference in the results from the STP and EHS methods for any lines in the system.

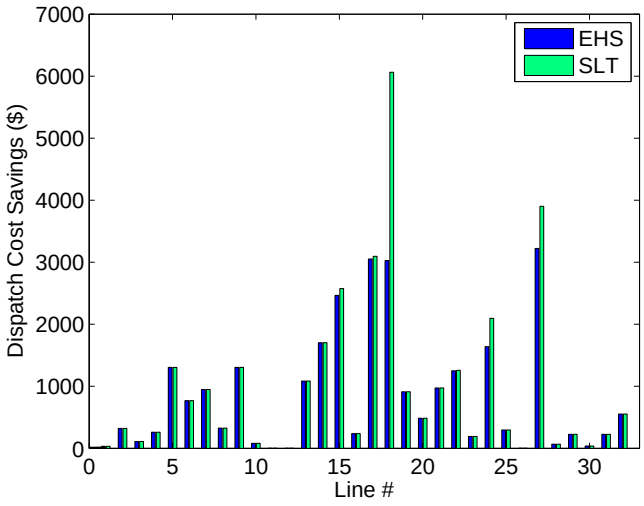

Figure 2.6: STP versus EHS Dispatch Cost Decrease in January.

The STP method is based on the sensitivity metric of shadow pricing of line constraints. In the DC approximated line flow paradigm the FLSC is constant and continuous. The shadow pricing on the other hand is constant only as long as the constraint is active. For lines that are constrained before the flow control upgrade is considered and are still constrained after the upgrade, the resulting dispatch cost decrease will be the same for the STP and EHS methods. It is when a constrained line becomes unconstrained post upgrade and the shadow price goes from a non-zero value to zero that the STP and EHS begin to diverge. The opposite is also true, in that if a line is uncongested pre-upgrade but becomes congested post-upgrade the STP and EHS methods will diverge due to the discontinuous step change of the shadow price from zero to a non-zero number. In July, the load is sufficiently high

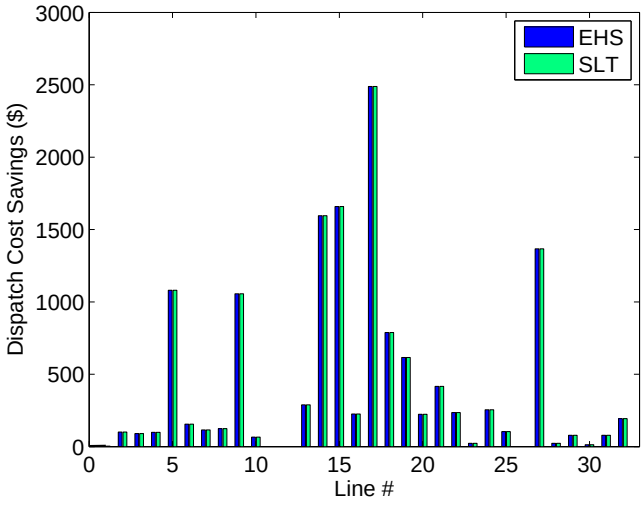

Figure 2.7: STP versus EHS Dispatch Cost Decrease in July,

that although the upgrade provides congestion relief that decreases dispatch cost the active constraint set does not change. In January, the active constraint set does change which leads to the divergence in the results of the STP and EHS methods described.

Although the STP method does not produce the exact same results for dispatch cost decrease as the EHS method, the STP does produce results close enough to provide a set of candidate lines for further investigation. As discussed before, it is the candidate set that is most important in the early points of transmission planning because various other system impact studies must also be performed. An investigation into actual site construction upgrade costs must also be performed. It is only feasible to do these types of further due diligence on a set of upgrade options you have confidence will have an expected market impact.

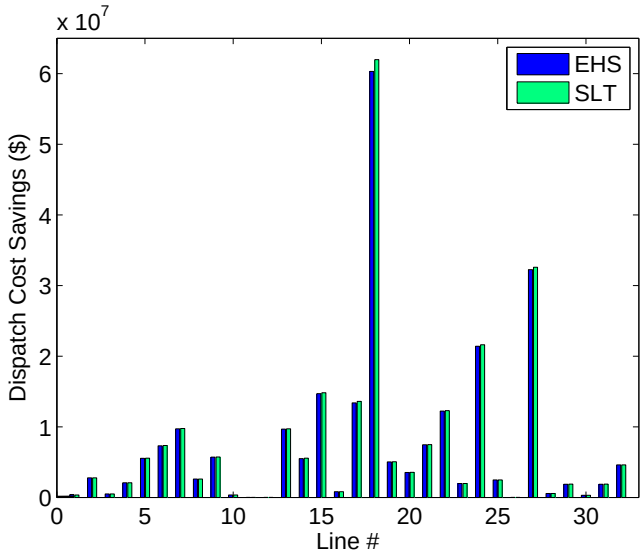

Figure 2.8: STP versus EHS Dispatch Cost Decrease for Remaining Ten Year Horizon.

2.4.1.5 Ten Year Planning Horizon

A planning tool like the STP method must be viable for multiple years in the planning horizon. To illustrate the viability of the STP method in multiple planning years a 10 year study based on the 24 bus ERCOT modeled system is performed. To create the system for a ten year horizon, the load is scaled based off the ten year long-term forecast published by ERCOT [35]. The peak values forecasted are used as indicators of overall growth. The base year used is 2013 from the report and all loads in the simulation are scaled proportionally to the increase in peak load. In year four of the simulation, generation is increased by 10% in order to account for load growth and provided enough generation in the peak times of the year. Also, wind capacity in the simulation is increased by 2% per year. The same process is used to produce Fig. 2.8 as is used to produce Fig. 2.5.

From Fig. 2.8 it can be seen that in the remaining years of the 10 year horizon the

STP method performs very well compared to the EHS method. In fact, it seems to perform even better than in the one year horizon. Most importantly, the candidate set produced by the STP method is the same as that produced by the EHS method. It is an accurate candidate set that is most crucial for the rest of the planning process.

2.4.2 IEEE 118 Bus System

2.4.2.1 Transmission Grid

A modified IEEE 118 bus system, shown in Fig. 2.9 is adapted from [2] for testing. The system consists of 3 zones, 118 buses, 179 single line branches, 54 generators, and 91 loads. Each line has its own line limit but in the base case none were active constraints so all interzonal lines (line numbers 44, 45, 54, 104, 112, 116, 178, 123, 141, 151, and 152) had their respective limits reduced to 90 MW. The OPF model used for testing is a lossless model so only the reactance values of the lines shown in Table III of [2] are used. Transformer tap data in Table IV of [2] is ignored.

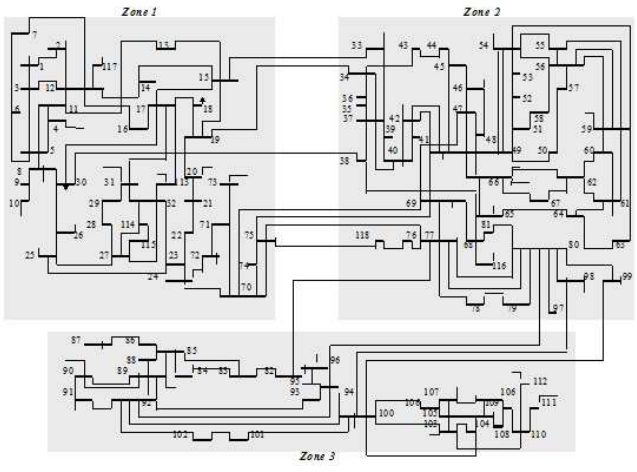

Figure 2.9: IEEE 118 Bus System [2].

2.4.2.2 Generation and Load

Generation capacity, cost, and location were described in [2] and have not been modified except that the cost structure used in the dispatch trials only consider the marginal per MW cost. A diurnal hourly load pattern is used as a 'typical' day. It too is provided in [2]. This is also extrapolated in the same way as was done with the 24 bus system to produce 12 'typical' load patterns for testing. One difference is that the 'typical' day is considered 85% of the yearly peak. Ancillary service reserve and dispatch data in Tables V and VII of [2] are not used for testing.

2.4.2.3 Analysis

Fig. 2.10 shows the annual dispatch cost decrease for STP and EHS trials on all 179 lines in the 118 bus system. It can be seen that the majority of lines do not have significant impact on dispatch cost when flow control is employed. As in the results for the 24 bus system a set of lines with significant impact begins to emerge. In the 24 bus system nearly a third of the lines show significant impact whereas in the 118 bus system the percentage of lines showing significant impact is much lower. It must be noted that the amount of dispatch cost decrease is lower in the 118 bus system than in the 24 bus system. This is due mostly to difference in peak loading. Although the 118 bus system has more buses it has about a tenth of the peak load. The other factors include the differing cost functions in the two systems. The 118 bus system only contains conventional units whose lowest marginal cost function is around \$8 whereas the 24 bus system includes wind resources with negative marginal cost as low as \$-16.

Fig. 2.11 and Table 2.3 show the STP and EHS results for the 10 lines in the 118 bus system that produced the largest system dispatch cost decreases. The STP and EHS methods produce almost identical results with only small discrepancies in

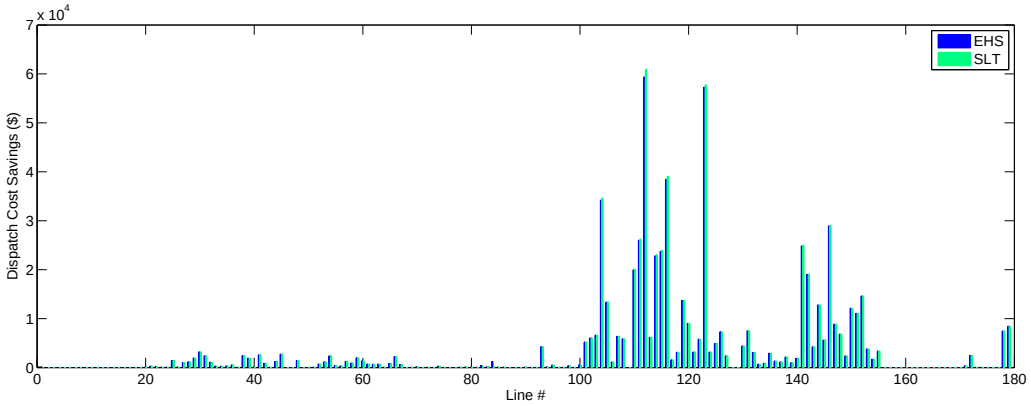

Figure 2.10: STP versus EHS Full Year Dispatch Cost Decrease.

a few lines. Table 2.3 shows that even for the highest performing candidate the STP method only produces a 2.57% difference in dispatch cost decrease versus the EHS method. Seven of the top ten candidates show a less than one percent difference between the two methods. But more importantly, as in the 24 bus system trials, both methods produce the same top performing candidate list. This list can then have other tests performed on them as necessary. It can also be seen that some intuitive candidates like those in the list of congested lines show large benefits from flow control but so do some uncongested lines. In total, the 118 bus system has 11 congested corridor lines. In the top ten lines only 5 are of the congested line set while the other 5 are not. This agrees with the findings in the trials performed on the 24 bus system in that the STP method can find both the intuitive and non-intuitive high performing candidates.

2.4.3 Computational Advantages of STP Method

Decreased computation time is a major advantage for the STP method versus the EHS method. The STP method only needs one base dispatch result per interval in the planning horizon to produce the candidate list. The EHS method needs a

Table 2.3: 118 Bus Top Ten Flow Control Upgrade Candidates

EHS			STP			
Rank	Line #	Savings ($)	Rank	Line #	Savings ($)	% diff
1	112	59,392	1	112	60,920	2.57
2	123	57,281	2	123	57,779	0.87
3	116	38,435	3	116	39,039	1.57
4	104	34,197	4	104	34,653	1.33
5	146	28,971	5	146	29,011	0.14
6	111	26,014	6	111	26,267	0.97
7	141	24,862	7	141	24,941	0.32
8	115	23,783	8	115	23,975	0.81
9	114	22,846	9	114	23,065	0.96
10	110	19,930	10	110	20,099	0.85

dispatch per interval per possible line upgrade. The computation statistics for the 24 bus system and 118 bus system presented earlier are assembled in Table 2.4. In the numerical trials for this, only one 'typical' day is used to represent a month. Each of the 'typical' days has 24 intervals (one hour per interval). So for the numerical trials, the number of intervals dispatched is 288 as shown in Table 2.4.

Table 2.4: Computation Statistics

Method	# of Buses	# of Intervals	Computation Time (s)	Scaled Computation Time (hr)
STP	24	288	103	.87
EHS	24	288	3796	32.07
STP	118	288	494	4.17
EHS	118	288	97978	827.82

The total time needed for the numerical trials on the 24 bus system using the STP method is 103 seconds. If that were scaled to a full year number (instead of a 'typical' day per month) the time needed would be .87 hours. Using the EHS method

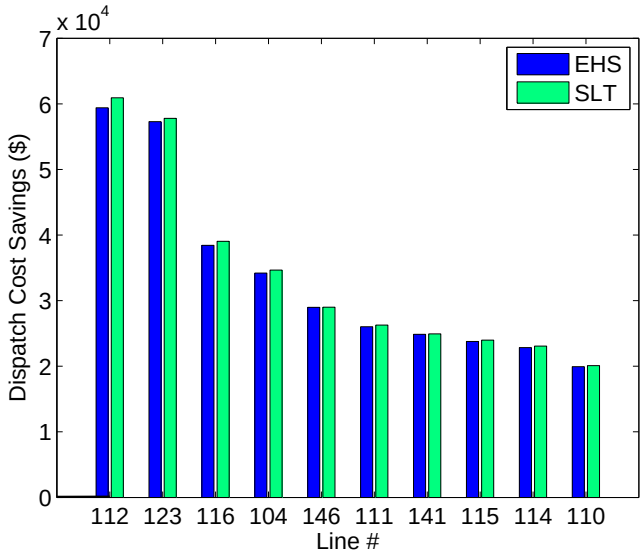

Figure 2.11: Top Ten Flow Control Upgrade Candidates.

on the 24 bus system, the time needed is 3,796 seconds or 63.3 minutes. Scaled to a full year, the time needed would be 32 hours. For the 118 bus system, the time needed for the STP method is 494 seconds or 8.2 minutes. The scaled number is 4.17 hours. For the EHS method on the 118 bus system, the needed computation time is 27.2 hours and when scaled it is 827.8 hours. All simulations were performed using MATLAB version R2012a running on an HP model h8-1080t running a Windows 7 64-bit operating system with an Intel i7 3.47 GHz processor.

It is obvious from the results that as the system becomes larger the necessary time to do an EHS method would be infeasible. Even with an optimized commercial grade dispatch software, an exhaustive search would unlikely be used. Thus intuition and experience would govern the original test set for the search for the best location for the added VSC based embedded HVDC line. The STP method, on the other hand, only needs one base dispatch run to produce a candidate set while also considering all possibilities.

2.4.4 Numerical Trials with Converter Losses

Numerical trials on the ERCOT modeled 24 bus system are repeated. In this set of trials, the converter losses are included in the SCED formulation used by the EHS. The equations developed in Section III E are used for the application of the STP method. The comparison of the results from the EHS and STP methods is shown in Fig. 2.12.

It can be seen that the STP method with converter losses performs with similar precision as the STP method that does not consider losses. The absolute values of the dispatch cost decrease are lower, as can be expected, because the cost of losses in the converters is included. Also noteworthy is that many lines no longer have non-zero values for dispatch cost decrease. This is because the cost of losses from the converters due to flow through the VSC based embedded HVDC system is higher than the possible benefits. In these scenarios, the VSC based embedded HVDC system would not be dispatched.

2.5 Conclusion

In this chapter, a ranking algorithm of prioritizing the incorporation of VSC-based HVDC transmission line for improved economic dispatch is proposed. This algorithm, termed as Smart Targeted Planning (STP), proposes a line shadow price-based weighting approach to ranking the potential economic impact of incorporating a new VSC-based HVDC link along existing transmission lines. The predicted dispatch cost decrease by the STP method is compared to an Exhaustive Heuristic Search (EHS) of all possible line upgrades in an ERCOT-equivalent 24 bus system and in an IEEE 118 bus system.

In simulations on both systems, the much quicker STP algorithm predicted absolute values for dispatch cost decrease very similar to that found by the time intensive

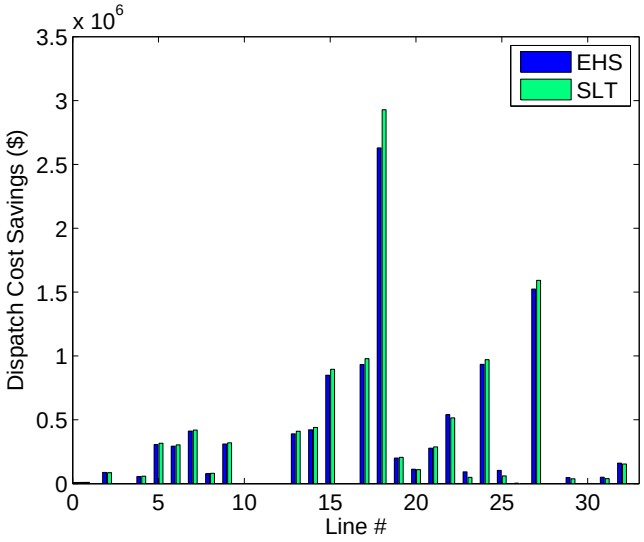

Figure 2.12: STP versus EHS Full Year Dispatch Cost Decrease with Converter Losses.

EHS. More importantly, the STP method suggests the same top ten candidates for line upgrades, many of which were non-intuitive choices.

3. SINGULAR VALUE SENSITIVITY BASED OPTIMAL CONTROL OF EMBEDDED VSC-HVDC FOR STEADY-STATE VOLTAGE STABILITY ENHANCEMENT*

3.1 Introduction

Growth of electrical demand in large power systems has been increasing at a faster rate than the expansion of transmission facilities. This trend, coupled with the increased penetration of variable resources such as wind and solar, which tend to be electrically far from load centers, have been significantly stressing electric transmission systems. The increasing stress on transmission systems is typically manifested by decreasing voltage stability margins in many regions around the world as was the case in the 2003 Italy blackout [36]. As one of the emerging flexible control technologies, VSC based HVDC is becoming a promising solution to enhance AC grid performance[37, 38]. This chapter seeks to improve the voltage stability in large interconnected AC systems by control of VSC based embedded HVDC systems.

The problem of voltage stability has been investigated by many researchers in a large body of literature. One approach of analysis focuses on Thevenin-like equivalents as a means to establish margins to voltage instability [39]. In [40], voltage instability predictors based on Thevenin-like equivalents have been discussed. The challenge has been how to develop a quantifiable metric to describe system operating conditions in view of potential voltage instability. A fast computation method to find the minimum voltage stability margin focuses on the load parameter space feasibility and infeasibility regions [41]. The authors focus on load direction towards infeasi-

*This section is in part a reprint of the material in the following papers: (1) Reprinted with permission from O. A. Urquidez and L. Xie, "Singular Value Sensitivity Based Optimal Control of Embedded VSC-HVDC for Steady-State Voltage Stability Enhancement," *IEEE Transactions on Power Systems*, vol. 31, no. 1, pp. 216-225, Jan. 2016. Copyright 2016, IEEE.

bility. Other research has focused on generation direction (generation pattern) that can maximize the loading margin [42]. Both approaches concentrate on the voltage stability margin with respect to load increases.

An alternative approach in practice is PV curve analysis [7]. System operators such as the Electric Reliability Council of Texas (ERCOT) utilize PV analysis in both system planning and operations [4, 5]. Research in this area has a much longer standing with work in the continuation power flow and load characteristics particular to PV analysis coming in the early 1990s [43, 44]. Another very powerful, yet less utilized analysis method for evaluating voltage stability is to estimate the distance of load flow Jacobian to singularity [45, 46].

Over the past decade there has been a large body of literature on modelling and control of VSCs for the purpose of improving its own reliability [47, 48, 49, 50]. More recently, the VSC based HVDC system has been envisioned as a tool for system support [51, 52, 53, 54]. Refs. [51] and [52] utilize the flexibility of a VSC based non-embedded HVDC system to support voltage in one of the interconnected AC systems while [53] and [54] focus on utilization of embedded VSC-HVDC to improve power swing damping.

Several observations emerge from the preceding discussion that motivate the work in this chapter:

1. Steady-state voltage stability is a long standing power systems problem that still has great relevance today.

2. Analysis of steady-state voltage stability in the industry has focused on PV analysis but another very powerful, yet less utilized analysis method, is singular value of the load flow Jacobian.

3. VSC-HVDC is a new and powerful device and while much interest has focused

on its own stability a new line of research is focusing on how it can be utilized to provide AC system wide benefits.

In this work, a novel approach based on singular value sensitivity based optimal control is proposed to enhance steady-state voltage stability (SSVS). The algorithm utilizes a global metric of SSVS, the singularity of the load flow jacobian. The proposed supplementary control is in the new and exciting field that seeks to utilize VSC-HVDC for global AC power system enhancement. This work is directly targeted at utilizing VSC-HVDC for *power system-side* benefit of improving steady-state voltage stability.

The rest of the chapter is organized as follows. In Section II, both the classical PV analysis representation and the load flow Jacobian based analysis of steady-state (quasi-static) voltage stability (SSVS) is formulated. A methodology that maps existing PV analysis based criteria to a load flow Jacobian is also introduced. In Section III, Singular Value Sensitivity (SVS) based control for SSVS is proposed. Section IV introduces the concept of the VSC based embedded HVDC capability space. Case studies presented in Section V show promising results of SVS based control for VSC based embedded HVDC. Concluding remarks and future research questions are provided in Section VI.

3.2 Problem Formulation

3.2.1 PV Curve Representation of Steady-State Voltage Stability

The introduction to the classic PV curve representation of steady-state voltage stability (SSVS) begins with the derivation of real power transfer from a generator to a load over a transmission line. The real and reactive power demand of the load can be represented as follows:

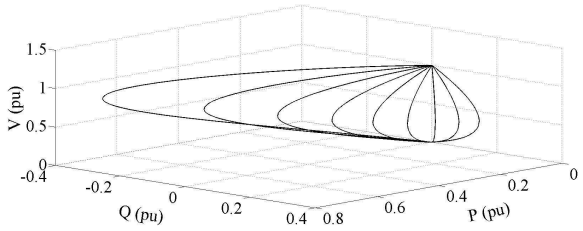

Figure 3.1: Power Transmission Feasibility Meridians.

$$P_D = \frac{|V_L| \sin(\theta_L)}{|Z|} \tag{3.1}$$

$$Q_D = \frac{|V_L|^2}{|Z|} - \frac{|V_L| \cos(\theta_L)}{|Z|} \tag{3.2}$$

Assuming the transmission line to be purely reactive with a value of X, an expression for V_L, the voltage at the load is as follows:

$$|V_L| = \sqrt{\frac{E^2}{2} - Q_D X \pm \sqrt{\frac{E^4}{4} - X^2 P_D^2 - X E^2 Q_D}} \tag{3.3}$$

Fig. 3.1 shows the feasibility meridians that relate P_D, Q_D, and V_L. The projection of these meridians on to the PV plane is what is commonly referred to as the PV curves, shown in Fig. 3.2.

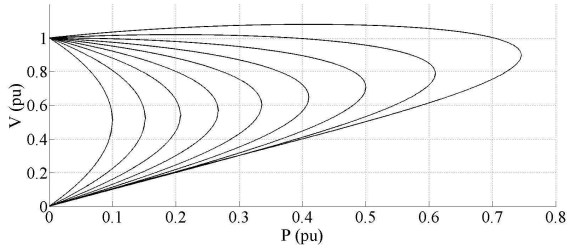

Figure 3.2: PV Curves.

The nose point of the PV curves is the point at which the system is unstable in the sense of steady-state voltage stability. This brief derivation which follows that in [55] is sufficiently general to serve as an introduction to PV analysis, a method of steady-state voltage stability analysis widely used in the industry today.

3.2.2 Steady-State Voltage Stability and the Load Flow Jacobian

Another representation of the SSVS problem in the literature is the analysis of the SSVS problem via the load flow Jacobian. The load flow Jacobian is a static representation of the relationship between small changes in V and θ and the resulting changes in P and Q. The linearized relationship is shown in (4.19).

$$\begin{bmatrix} \Delta P \\ \\ \Delta Q \end{bmatrix} = J \begin{bmatrix} \Delta \theta \\ \\ \Delta V \end{bmatrix} \tag{3.4}$$

The load flow Jacobian can be parsed as follows:

$$J = \begin{bmatrix} J_{P\theta} & J_{PV} \\ \\ J_{Q\theta} & J_{QV} \end{bmatrix}, \tag{3.5}$$

where, $J_{P\theta}$, J_{PV}, $J_{Q\theta}$, and J_{QV} are the sensitivity matrices of (P,Q) with respect to (V,θ).

Expanding (4.19) we get (4.25) and (4.26).

$$\Delta P = J_{P\theta}\Delta\theta + J_{PV}\Delta V \tag{3.6}$$

$$\Delta Q = J_{Q\theta}\Delta\theta + J_{QV}\Delta V \tag{3.7}$$

To find the strict relationship between ΔQ and ΔV, we hold $\Delta P = 0$ and obtain,

$$\Delta\theta = -J_{P\theta}^{-1} J_{PV}\Delta V. \tag{3.8}$$

Substituting (4.27) into (4.26) we obtain the relationship for ΔQ and ΔV as

$$\Delta Q = J_R \Delta V \tag{3.9}$$

where,

$$J_R = J_{QV} - J_{Q\theta} J_{P\theta}^{-1} J_{PV}. \tag{3.10}$$

For voltage stability the singular value vector, $\overline{\sigma}_{J_R}$, must remain strictly positive,

$$\overline{\sigma}_{J_R} > 0. \tag{3.11}$$

From this requirement, we define the critical value σ_c for SSVS as

$$\sigma_c = \min\{\overline{\sigma}_{J_R}\}. \tag{3.12}$$

3.2.3 Singular Value Criteria for Voltage Stability Margin

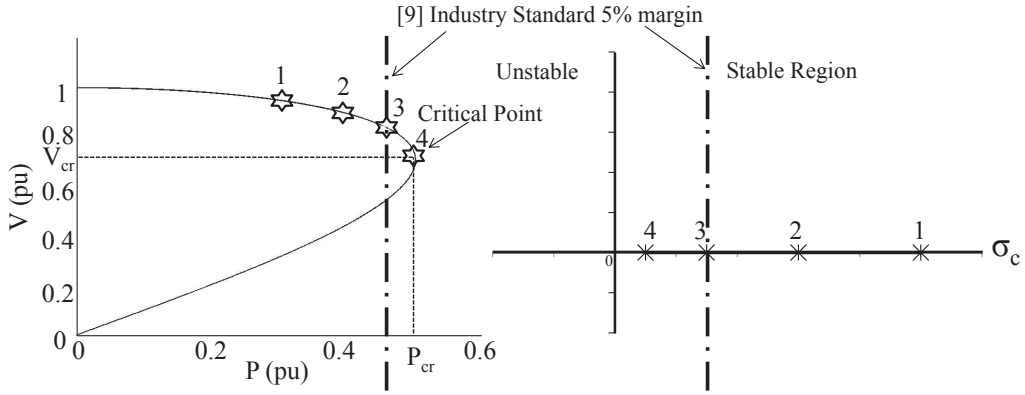

Figure 3.3: Mapping of PV Curve Threshold to Critical Singular Value Space [3][4][5].

In the classical representation, as a power system is stressed the PV curve approaches the critical point as illustrated in Fig. 3.3. Power transfer past that point will result in a voltage collapse. Simultaneously, the smallest singular value, σ_c, of the load flow Jacobian, J_R, approaches zero. For stability the singular values must remain robustly positive. As will be discussed in detail later, the control algorithm proposed uses the metric of smallest singular value of the reduced load flow Jacobian,

J_R, as a target for control.

The goal of threshold criteria mapping is to relate the metric used in Singular Value Sensitivity (SVS) based control to one that is widely used in transmission planning and power system operations. An industry standard is to have a 5% to 10% margin in the PV analysis as the steady-state voltage stability limit. For example, ERCOT uses a 5% margin as a standard [4][5]. The simultaneous movement of the operating point and σ_c, towards the critical point on the PV curve and towards zero, respectively, is illustrated in Fig. 3.3. The industry standard of 5% percent margin is denoted by the dotted vertical line. This point simultaneously corresponds to a particular value of σ_c. This is then used as the threshold in the singular value space and is denoted by the dotted line.

3.3 Singular Value Sensitivity Based Control

3.3.1 Load Flow Jacobian Singular Value Sensitivity

Singular value sensitivity based control depends on the sensitivity of the critical singular value, σ_c, to changes in the system injection vectors P and Q. The Voltage Source Converter (VSC) based embedded HVDC system can control independently some of the values in the P and Q injection vectors. A two terminal VSC based embedded HVDC system has 3 independent control variables, P_{sr}, Q_s, and Q_r, the real power transfer, the reactive power injection at the sending end, and the reactive power injection at the receiving end, respectively. These changes will affect the elements in the reduced Jacobian, J_R, described in (4.29). By changing the elements in J_R, the VSC based embedded HVDC can change the position of the critical singular value, σ_c. The relationship of the independent control variables of the VSC based embedded HVDC and the critical singular value is highly non-linear and dependent on the system operating point.

The algorithm uses small changes in the control variables to find the corresponding sensitivities. It begins by finding the current critical value at operating point k as in (4.36).

$$\sigma_c(P_k, Q_k) = \min\{\overline{\sigma}_{J_R}(P_k, Q_k)\} \tag{3.13}$$

A small change, $\overline{\delta}_{P_{sr}}$, in the injection vector P_k is applied and the resulting critical singular value found as in (4.32).

$$\sigma_c(P_k + \overline{\delta}_{P_{sr}}, Q_k) = \min\{\overline{\sigma}_{J_R}(P_k + \overline{\delta}_{P_{sr}}, Q_k)\} \tag{3.14}$$

The sensitivity to this small change is found via (4.33).

$$a_{1,\Delta P_{sr,k}} = \frac{\sigma_c(P_k + \overline{\delta}_{P_{sr}}, Q_k) - \sigma_c(P_k, Q_k)}{\delta_{P_{sr}}} \tag{3.15}$$

Similarly, $\overline{\delta}_{Q_s}$ and $\overline{\delta}_{Q_r}$ can be applied to find the resulting critical singular values with respect to changes in the reactive power at the sending and receiving end of the VSC based embedded HVDC system as in (4.34) and (4.35).

$$\sigma_c(P_k, Q_k + \overline{\delta}_{Q_s}) = \min\{\overline{\sigma}_{J_R}(P_k, Q_k + \overline{\delta}_{Q_s})\} \tag{3.16}$$

$$\sigma_c(P_k, Q_k + \overline{\delta}_{Q_r}) = \min\{\overline{\sigma}_{J_R}(P_k, Q_k + \overline{\delta}_{Q_r})\} \tag{3.17}$$

In the same manner as (4.33), these resulting critical singular values can then be utilized to find the corresponding sensitivities as in (4.37) and (4.38).

$$a_{1,\Delta Q_{s,k}} = \frac{\sigma_c(P_k, Q_k + \overline{\delta}_{Q_s}) - \sigma_c(P_k, Q_k)}{\delta_{Q_s}} \tag{3.18}$$

$$a_{1,\Delta Q_{r,k}} = \frac{\sigma_c(P_k, Q_k + \overline{\delta}_{Q_r}) - \sigma_c(P_k, Q_k)}{\delta_{Q_r}} \tag{3.19}$$

For brevity, in all further sensitivity derivations Q_s and Q_r will be referred to as

Q. It is important to stress that they are in fact different values but the structure of the equations that are used to derive them are similar.

The optimal control step in the Singular Value Sensitivity control algorithm can be formulated using either a first order or second order approximation as will be explained in Subsection III C. The sensitivities found via (4.33), (4.37), and (4.38) are sufficient for the optimal control step using a first order approximation.

To obtain the second order sensitivities necessary for the optimal control step utilizing a second order approximation, a second perturbation is applied and the sensitivities to this perturbation found via (4.42)-(4.43).

$$a_{1b,\Delta P_{sr,k}} = \frac{\sigma_c(P_k + 2\overline{\delta}_{P_{sr}}, Q_k) - \sigma_c(P_k + \overline{\delta}_{P_{sr}}, Q_k)}{\delta_{P_{sr}}} \tag{3.20}$$

$$a_{1b,\Delta Q_k} = \frac{\sigma_c(P_k, Q_k + 2\overline{\delta}_Q) - \sigma_c(P_k, Q_k + \overline{\delta}_Q)}{\delta_Q} \tag{3.21}$$

Using the values of a_{1a} and a_{1b} the second order sensitivities for $\Delta P_{sr,k}$ and ΔQ_k are found via (4.45) and (4.46), respectively.

$$a_{2,\Delta P_{sr,k}} = \frac{a_{1b,\Delta P_{sr,k}} - a_{1,\Delta P_{sr,k}}}{\delta_{P_{sr}}} \tag{3.22}$$

$$a_{2,\Delta Q_k} = \frac{a_{1b,\Delta Q_k} - a_{1,\Delta Q_k}}{\delta_Q} \tag{3.23}$$

3.3.2 SVS Based Control Algorithm Flow Diagram

The SVS control algorithm is a supplementary control algorithm that only becomes active during heavily stressed scenarios. The trigger for the supplementary control action is a singular value threshold as discussed in Subsection II C, which is termed the Trigger Threshold. Because this is a supplementary control, the principal order is already in place for the control variables of each of the VSC based embedded HVDC systems involved in the control, $P_{sr,i}$, $Q_{s,i}$, and $Q_{r,i}$. The SVS control

algorithm will utilize the control actions $P_{sr,i}$, $Q_{s,i}$, and $Q_{r,i}$ in combination for the wide-area protection and control (WAPC) target of steady-state voltage stability.

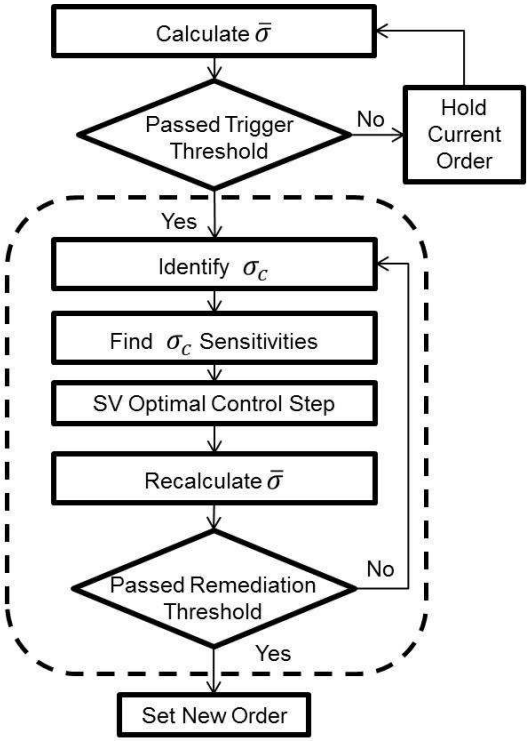

Figure 3.4: SVS Control Flow Diagram.

A block diagram of the SVS control algorithm is shown in Fig. 3.4. The algorithm attempts to provide a new order for $P_{sr,i}$, $Q_{s,i}$, and $Q_{r,i}$ that moves the critical singular value, σ_c, away from 0, passed a predefined singular value with minimum control energy. This value is termed the Remediation Threshold. The upper section of the block diagram shows that during normal operation the supplementary control will continue to loop through calculations of the most current set of system singular values, $\overline{\sigma}$. If any of the values in $\overline{\sigma}$ violate the trigger threshold then SVS control is engaged.

Both the remediation threshold and the trigger threshold would be decided upon in advance by the system operator. The trigger threshold is a lower value that triggers the beginning of the SVS supplementary control. To avoid repeated activation-deactivation cycles, the remediation threshold should be slightly higher than the trigger threshold.

Within the SVS control loop, σ_c is identified and the sensitivities with respect to the control actions are found (4.36-4.46). These sensitivities are then utilized in the optimal control step explained in depth in the next section. The output of the optimal control step is an intermediate order for $P_{sr,i}$, $Q_{s,i}$, and $Q_{r,i}$. This intermediate order is then used to recalculate $\overline{\sigma}$. If all the system singular values are now passed the remediation threshold, the algorithm will stop and the new order will be set and implemented by the VSC based embedded HVDC system. If there are still violations with respect to the remediation threshold the loop will continue to the next iteration. This loop is only used to calculate the new order. This order is not utilized until the algorithm breaks out of the loop.

3.3.3 Optimal Control of VSC-HVDC Parameters

The optimal control step is formulated as a minimization of the control efforts of the independent control variables of all of the VSC based embedded HVDC systems for each iteration whose general form is shown in (4.48).

$$\min_{x} \sum_{i \in L} P_{sr,i,k+1}^2 + Q_{s,i,k+1}^2 + Q_{r,i,k+1}^2 \tag{3.24}$$

s.t.

$$G(x) = 0, g(x) = 0, \ \ \forall \ \ i \in L$$

$$H(x) \leq 0, h(x) \leq 0, \ \ \forall \ \ i \in L$$

The decision variable vector x is defined as $x = [\Delta P_{sr,i,k}, \Delta Q_{s,i,k}, \Delta Q_{r,i,k}]$. The

linear and non-linear equality constraints are $G(x)$ and $g(x)$, respectively. The linear and non-linear inequality constraints are $H(x)$ and $h(x)$, respectively. The most basic linear equality constraints are (4.49)-(4.51) which relate x to the objective function.

$$P_{sr,i,k+1} = P_{sr,i,k} + \Delta P_{sr,i,k}, \ \ \forall \ \ i \in L \tag{3.25}$$

$$Q_{s,i,k+1} = Q_{s,i,k} + \Delta Q_{s,i,k}, \ \ \forall \ \ i \in L \tag{3.26}$$

$$Q_{r,i,k+1} = Q_{r,i,k} + \Delta Q_{r,i,k}, \ \ \forall \ \ i \in L \tag{3.27}$$

The linear inequality constraints (4.52)-(4.59) maintain the VSC based embedded HVDC system control variables within operating limits.

$$P_{sr,i,min} \leq P_{sr,i} \leq P_{sr,i,max}, \ \ \forall \ \ i \in L \tag{3.28}$$

$$Q_{s,i,min} \leq Q_{s,i} \leq Q_{s,i,max}, \ \ \forall \ \ i \in L \tag{3.29}$$

$$Q_{r,i,min} \leq Q_{r,i} \leq Q_{r,i,max}, \ \ \forall \ \ i \in L \tag{3.30}$$

The key constraint is (4.60), which utilizes the a_1 sensitivity coefficients (4.36-4.46). This constraint utilizes a simple first order approximation to constrain the optimal control step to a set of control variable combinations that will achieve the predetermined singular value step size, Λ_σ.

$$\sum_{i \in L} a_{1,\Delta P_{sr,i,k}} \Delta P_{sr,i,k} + a_{1,\Delta Q_{s,i,k}} \Delta Q_{s,i,k} + a_{1,\Delta Q_{r,i,k}} \Delta Q_{r,i,k} = \Lambda_\sigma \tag{3.31}$$

The objective function in (4.48) combined with the constraints (4.49)-(4.60) make the optimal control step a Linearly Constrained Quadratic Programming (LCQP)

problem. Depending on the system operating conditions and the values of $\overline{\delta}_{P_{sr}}$, $\overline{\delta}_{Q_s}$, $\overline{\delta}_{Q_r}$ and Λ_σ, a better approximation may be necessary. Constraint (4.60) can be replaced with (4.61) to provide a simplified second order approximation that better approximates the relationship of the decision variables to the predetermined singular value step size, Λ_σ.

$$\begin{aligned}\sum_{i\in L}(a_{2,\Delta P_{sr,i,k}}\Delta P_{sr,i,k}+a_{1,\Delta P_{sr,i,k}})\Delta P_{sr,i,k}\\ +(a_{2,\Delta Q_{s,i,k}}\Delta Q_{s,i,k}+a_{1,\Delta Q_{s,i,k}})\Delta Q_{s,i,k}\\ +(a_{2,\Delta Q_{r,i,k}}\Delta Q_{r,i,k}+a_{1,\Delta Q_{r,i,k}})\Delta Q_{r,i,k}=\Lambda_\sigma\end{aligned} \tag{3.32}$$

Replacing constraint (4.60) with (4.61) changes the optimal control step from a LCQP problem to a Quadratically Constrained Quadratic Programming (QCQP) problem.

3.3.4 Proposed Algorithm with Local Voltage Correction

The loop of the SVS control algorithm in Fig. 3.4 focuses on the global target of singular value positioning. A second loop, as shown in Fig. 3.5, can be utilized so that the algorithm simultaneously achieves the global target as well as maintaining the local voltage magnitude. If the local voltage magnitude is within bounds the process is complete and the new order is set. If the voltage magnitude is out of bounds then the algorithm proceeds into the voltage correction loop. The voltage correction loop utilizes sensitivities within an optimal control step. Through iterations, it steps the voltage magnitude towards a predefined bandwidth while maintaining the singular value positioning achieved in the first loop. After the voltage magnitude reaches the predefined bandwidth the algorithm breaks out of the loop and the new order is set.

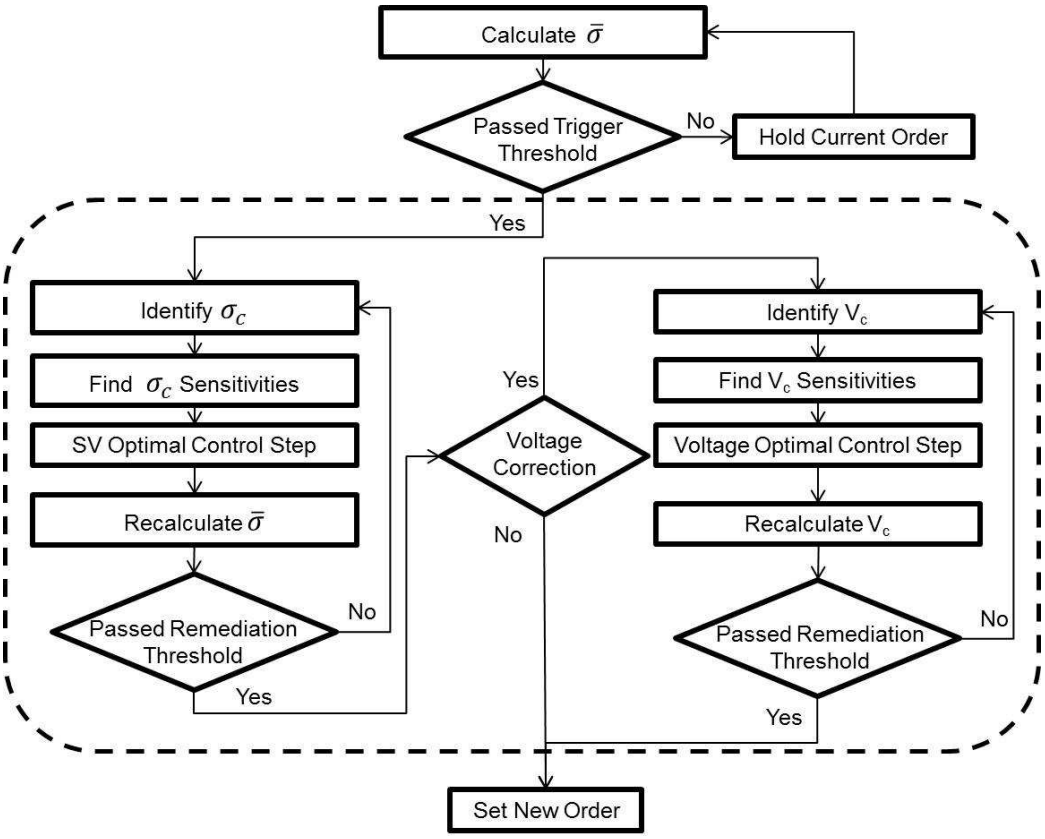

Figure 3.5: SVS Control Flow Diagram.

3.3.5 Optimal Control for Local Voltage Correction

The optimal control step in the voltage correction loop is similar to the optimal control step in the singular value loop. It uses perturbations in the independent control variables of the VSC based embedded HVDC system to find the sensitivities of these perturbations to the critical singular values, σ_c, as well as to the critical voltage magnitude, V_c. The first order sensitivities of V_c are found via (4.62)-(4.54).

$$b_{1,\Delta P_{sr,k}} = \frac{V_c(P_k + \overline{\delta}_{P_{sr}}, Q_k) - V_c(P_k, Q_k)}{\delta_{P_{sr}}} \tag{3.33}$$

$$b_{1,\Delta Q_k} = \frac{V_c(P_k, Q_k + \overline{\delta}_Q) - V_c(P_k, Q_k)}{\delta_Q} \tag{3.34}$$

The second order sensitivities are found via (3.35)-(3.38).

$$b_{1b,\Delta P_{sr,k}} = \frac{V_c(P_k + 2\overline{\delta}_{P_{sr}}, Q_k) - V_c(P_k + \overline{\delta}_{P_{sr}}, Q_k)}{\delta_{P_{sr}}} \tag{3.35}$$

$$b_{1b,\Delta Q_k} = \frac{V_c(P_k, Q_k + 2\overline{\delta}_Q) - V_c(P_k, Q_k + \overline{\delta}_Q)}{\delta_Q} \tag{3.36}$$

$$b_{2,\Delta P_{sr,k}} = \frac{b_{1b,\Delta P_{sr,k}} - b_{1,\Delta P_{sr,k}}}{\delta_{P_{sr}}} \tag{3.37}$$

$$b_{2,\Delta Q_k} = \frac{b_{1b,\Delta Q_k} - b_{1,\Delta Q_k}}{\delta_Q} \tag{3.38}$$

The optimal control step for the voltage correction loop uses the same standard form as the optimal control step in the singular value loop (4.48). Constraints (4.49)-(4.59) also still apply. The main difference comes with the replacement of constraint (4.60) by constraint (3.39) and (3.40).

$$\sum_{i \in L} b_{1,\Delta P_{sr,i,k}} \Delta P_{sr,i,k} + b_{1,\Delta Q_{s,i,k}} \Delta Q_{s,i,k} + b_{1,\Delta Q_{r,i,k}} \Delta Q_{r,i,k} = \Lambda_V \tag{3.39}$$

$$\sum_{i \in L} a_{1,\Delta P_{sr,i,k}} \Delta P_{sr,i,k} + a_{1,\Delta Q_{s,i,k}} \Delta Q_{s,i,k} + a_{1,\Delta Q_{r,i,k}} \Delta Q_{r,i,k} \leq \sigma_{c,i,k} - \Theta_\sigma \tag{3.40}$$

Constraint (3.40) uses a first order approximation relating the decision variables to the critical singular value, σ_c, and maintains the singular value threshold, Θ_σ, already achieved in the singular value loop. Constraint (3.39) uses a first order approximation relating the decision variables to the voltage magnitude, V_c to achieve a predetermined voltage step, Λ_V. The combination of the objective function in (4.48), constraints (4.49)-(4.59) and constraints (3.39) and (3.40) make the optimal control step a LCQP problem.

The optimal control step can utilize (3.41) and (3.42) in place of (3.39) and (3.40) to achieve a better approximation in each iteration of the voltage correction loop.

$$\begin{aligned}\sum_{i\in L}&(b_{2,\Delta P_{sr,i,k}}\Delta P_{sr,i,k}+b_{1,\Delta P_{sr,i,k}})\Delta P_{sr,i,k}\\&+(b_{2,\Delta Q_{s,i,k}}\Delta Q_{s,i,k}+b_{1,\Delta Q_{s,i,k}})\Delta Q_{s,i,k}\\&+(b_{2,\Delta Q_{r,i,k}}\Delta Q_{r,i,k}+b_{1,\Delta Q_{r,i,k}})\Delta Q_{r,i,k}=\Lambda_V\end{aligned}\tag{3.41}$$

$$\begin{aligned}\sum_{i\in L}&(a_{2,\Delta P_{sr,i,k}}\Delta P_{sr,i,k}+a_{1,\Delta P_{sr,i,k}})\Delta P_{sr,i,k}\\&+(a_{2,\Delta Q_{s,i,k}}\Delta Q_{s,i,k}+a_{1,\Delta Q_{s,i,k}})\Delta Q_{s,i,k}\\&+(a_{2,\Delta Q_{r,i,k}}\Delta Q_{r,i,k}+a_{1,\Delta Q_{r,i,k}})\Delta Q_{r,i,k}\leq\sigma_{c,k}-\Theta_\sigma\end{aligned}\tag{3.42}$$

Again, this might be necessary depending on the system operating conditions and the values of $\overline{\delta}_{P_{sr}}$, $\overline{\delta}_{Q_s}$, $\overline{\delta}_{Q_r}$ and Λ_V. This will also change the optimal control step from an LCQP problem to a QCQP problem.

3.4 Embedded VSC based HVDC Capability Space

A test system is prepared to introduce the concept of the embedded VSC based HVDC capability space. A 6 bus test system shown in Fig. 3.6 is an augmented version of the test system in [6]. The VSC based embedded HVDC line connects bus 4 and 5 and has no binding constraint.

The capability space can be formed with respect to the global metric, critical singular value, σ_c, or the local metric, voltage magnitude. The capability space with respect to σ_c is illustrated in Fig. 3.7.

A two terminal VSC based embedded HVDC system has 3 independent variables. To create the capability space in Fig. 3.7 the reactive power injection at bus 4, the sending end terminal, is held constant. The real and reactive power demanded via the AC system connections at bus 5 is varied and σ_c is calculated. It is clear from

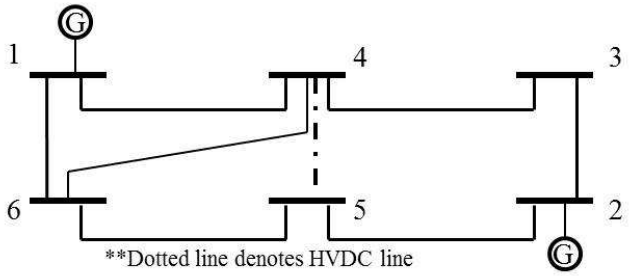

Figure 3.6: 6 Bus Test System [6].

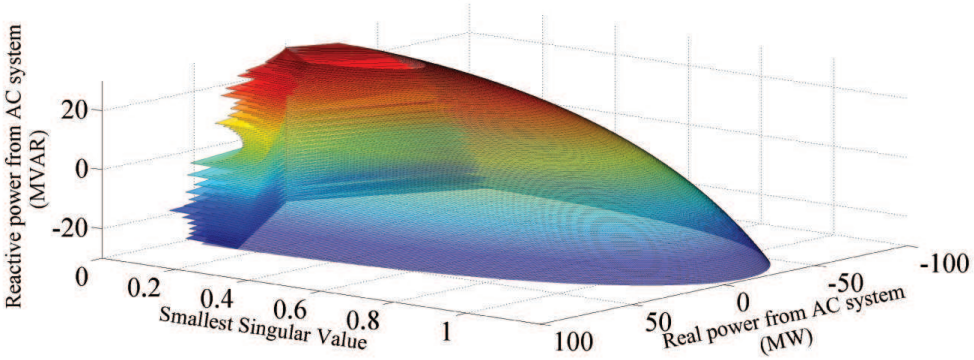

Figure 3.7: VSC HVDC Singular Value Partial Capability Space.

Fig. 3.7 (and consistent with intuition) that the more reactive power demanded via the AC system the lower σ_c becomes. Put another way, the more reactive power supplemented by the VSC based embedded HVDC system the higher σ_c becomes for a given real power transfer.

Fig. 3.7 shows the VSC based embedded HVDC capability space with respect to voltage magnitude at bus 5. The reactive power injection at bus 4 is again held constant while the other variables are varied and the bus 5 voltage magnitude is calculated.

The embedded VSC based HVDC capability spaces in Fig. 3.7 and Fig. 3.8 are

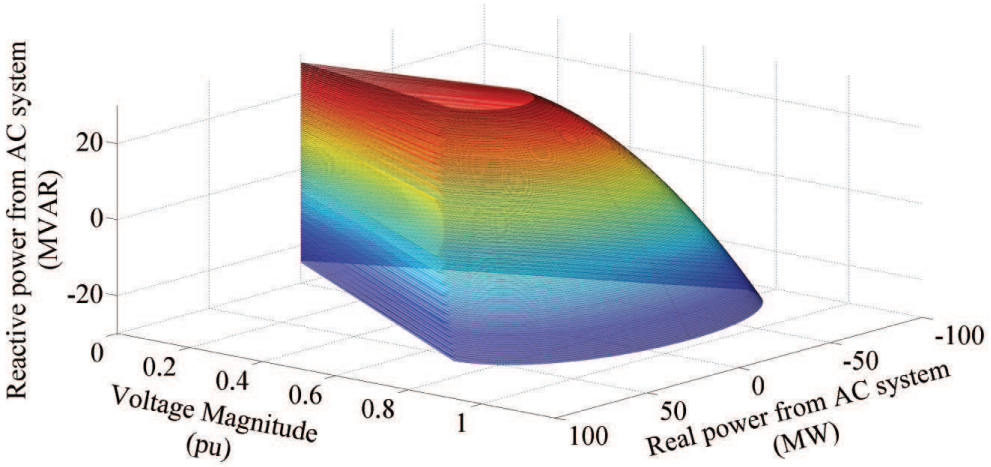

Figure 3.8: VSC HVDC Voltage Magnitude Partial Capability Space.

3d surfaces made of independent control of real and reactive power supplied via the AC system at Bus 5. When the third variable, Q_s, the reactive power injection at the sending end terminal, is varied the capability space creates concentric shells. This is illustrated in Fig. 3.9.

When the amount varied is made smaller and smaller the shells become a 3-dimensional shape. In a more complex VSC based embedded HVDC system with more terminals the capability space should continue to grow in dimension, in line with the number of added independent variables creating capability spaces in higher dimensions.

The capability spaces presented provide vital clarity through the visualization of the VSC based embedded HVDC system's effects on global and local metrics. The incorporation of powerful transmission systems like VSC based embedded HVDC is a large departure from the norm. Intuition into these new paradigms is crucial. Understanding these capability spaces helps to provide that intuition.

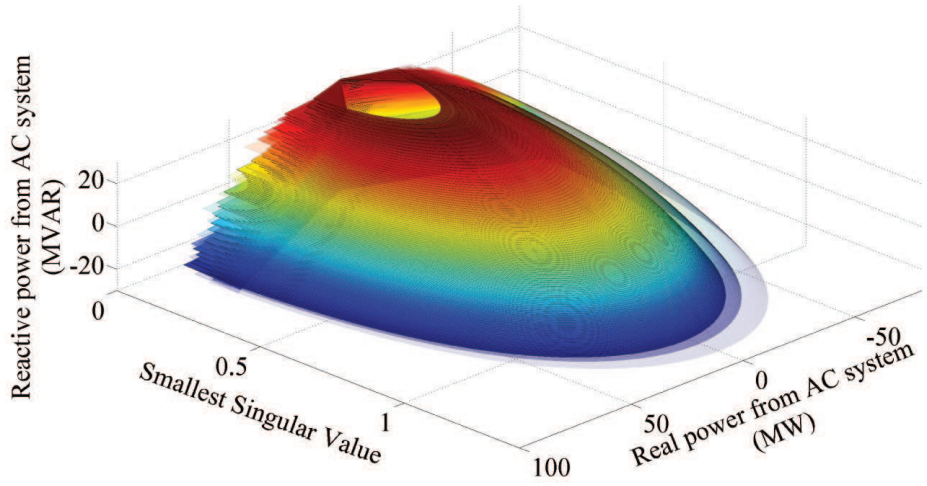

Figure 3.9: VSC HVDC Singular Value Full Capability Space.

3.5 Case Studies

In this Section, we present two case studies of the proposed control algorithm in a 6-bus and an IEEE modified 118-bus system, respectively. For clarity of the experiment, only 2 of the 3 VSC based embedded HVDC control variables are allowed to vary. The control variable, Q_s, of the embedded HVDC system is held constant with a value of 0. This corresponds to the case shown in Fig. 3.7. In actual implementation, all three control variables would be allowed to vary. Allowing Q_s to vary has no appreciable increase in computational burden. Further, although the SVS algorithm is generalizable to include multiple independent VSC-HVDC systems, only one VSC-HVDC system is use in the following numerical trials.

3.5.1 SVS Based Control without Voltage Correction

3.5.1.1 6 Bus Uncompensated System

The SVS based control algorithm without voltage correction is applied to the 6 bus system in Fig. 3.6. The results are presented in Fig. 3.10. The black triangles are the results in each iteration using the optimal control step with a first order approximation. In each iteration, the algorithm is stepping the critical singular value, σ_c, closer to the singular value threshold, Θ_σ, which in this case is 1. The black line represents the results in each iteration using the optimal control step with the second order approximation. They follow closely the results from the optimal control step with first order approximation. Because these results are from the SVS based control algorithm without voltage correction, once σ_c reaches 1 the algorithm breaks out of the loop and the iterations are complete.

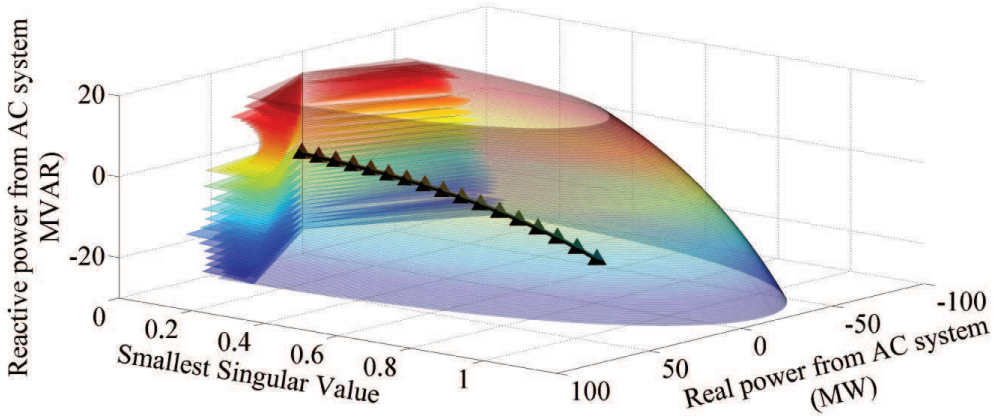

Figure 3.10: Singular Value Capability Space for 6 Bus Uncompensated System.

3.5.1.2 6 Bus Compensated System

The 6 bus system in Fig. 3.6 is augmented to include shunt susceptance for voltage support at the import constrained bus 5. This is a typical system planning strategy to increase import capacity. The SVS based control algorithm without voltage correction is applied to this system and the results are displayed in Fig. 3.11. Again, the optimal control step with first order approximation and second order approximation are represented by the black triangles and a black line, respectively. As with the uncompensated 6 bus system, the algorithm steps closer to the critical singular value threshold until it reaches it. For the compensated system, both the first order and second order approximations follow closely in their results.

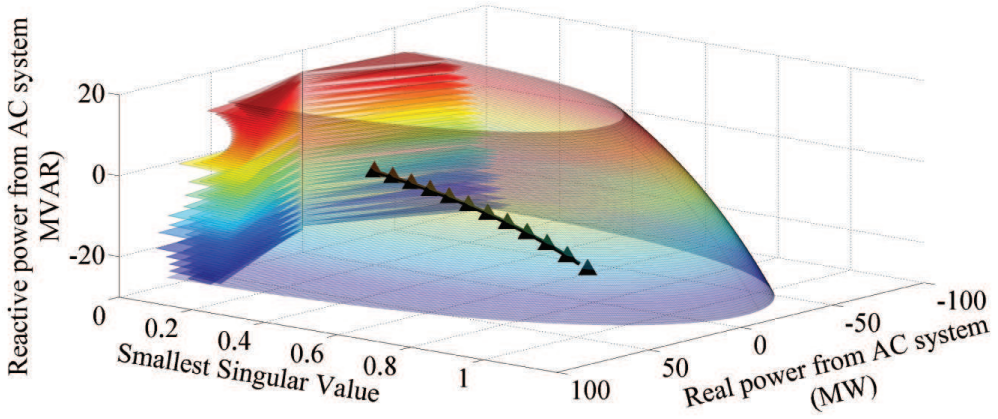

Figure 3.11: Singular Value Capability Space for 6 Bus Compensated System.

Fig. 3.12 shows the results of the same trial, but in the voltage magnitude capability space instead of the singular value capability space. It is evident in Fig. 3.12 that while the results of the SVS based control has provided a new order that achieves the singular value threshold (represented by the colored rainbow), it has

gone past acceptable limits for bus 5 voltage magnitude. This result highlights the motivation for the addition of the voltage correction loop to the SVS based control algorithm.

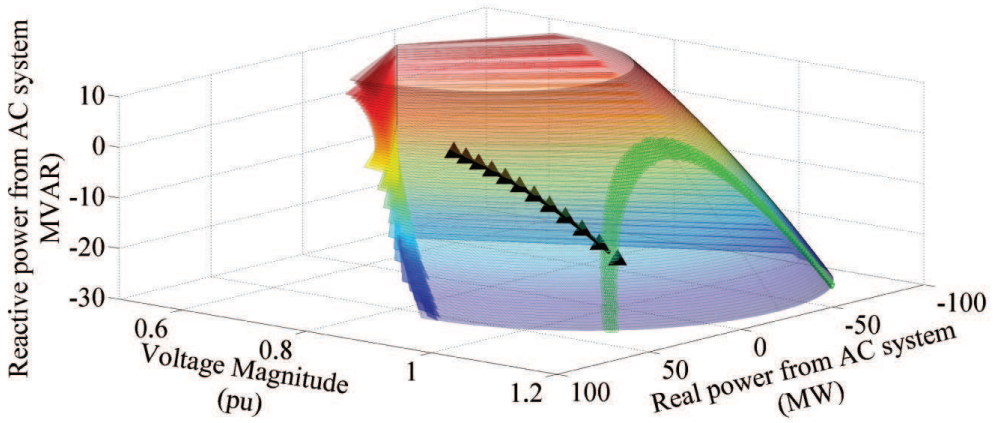

Figure 3.12: Voltage Capability Space for 6 Bus Compensated System.

3.5.2 SVS Based Control with Voltage Correction

3.5.2.1 6 Bus Compensated System

The SVS based control with voltage correction is applied to the 6 bus compensated system. The results are displayed in the voltage capability space in Fig. 3.13. It is evident from the results that the first objective is to efficiently approach the singular value threshold. Then there is an obvious direction change as the algorithm breaks into the voltage correction loop. The results then follow the equal singular value band (shown as a rainbow in the voltage capability plane) towards the acceptable bus 5 voltage limit, which in this case is 1.1 pu.

Within the voltage correction loop, the results stay fairly close to the singular value threshold, but that is not necessary in all cases. It is evident from (3.40) and

(3.42) that the singular value threshold is only a lower bound and has no upper bound in the voltage correction loop.

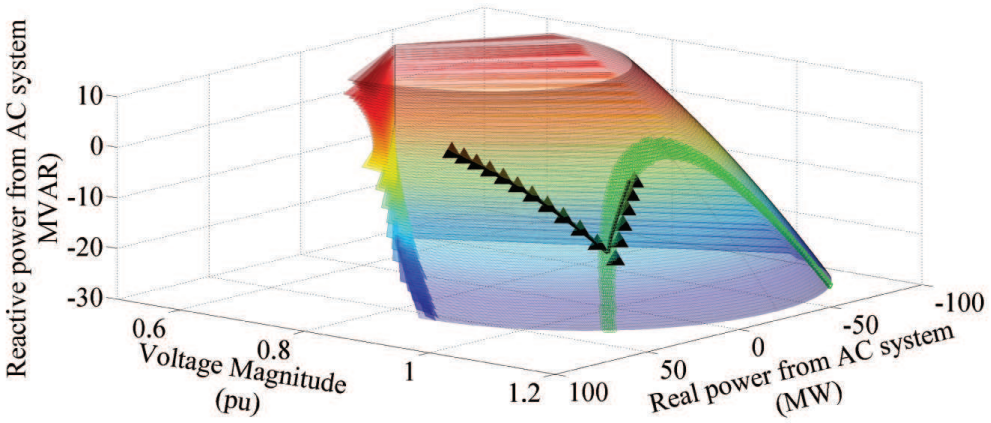

Figure 3.13: Voltage Capability Space for 6 Bus Compensated System with Voltage Correction.

3.5.2.2 IEEE 118 Bus System

The SVS based control algorithm with voltage correction is applied to a modified IEEE 118 bus system. To produce a stressed system for the case studies, the system in [2] is augmented in the following ways: 1) The base bus system parameters are from case118.m produced by Matpower [56]; 2) The reactive power only generators from zone 3 are eliminated; 3) The reactance of the corridor lines from zone 3 to zone 2 are increased to .2 pu; 4) The loads in zone 3 and the generation in zones 1 and 2 are increased equally to produce a stressed system transfer; 5) A two terminal VSC based embedded HVDC system is added connecting bus 80 and bus 96. The SVS based control algorithm with voltage correction is applied to the system and the results are shown for the singular value capability space and the voltage capability space in Fig. 3.14 and Fig. 3.15, respectively.

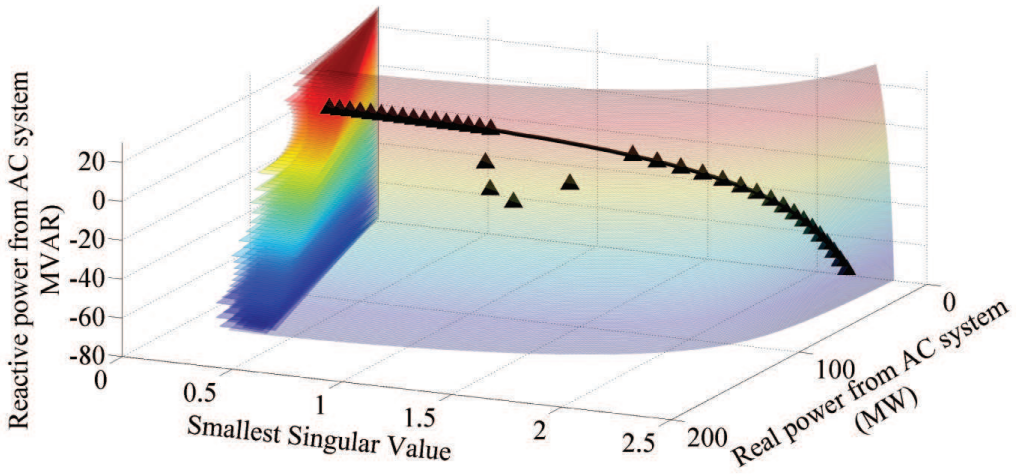

Figure 3.14: Singular Value Capability Space for IEEE 118 Bus System with Voltage Correction.

The iteration path taken by the algorithm to the final result show two distinct regimes for the results using the optimal control step with a first order approximation, shown by black triangles. There is a prominent U shaped dip present when the voltage correction loop begins. After 4 iterations, the trajectory again agrees with that of the optimal control step with the second order approximation, shown by the black line. This is the only major departure seen in the two sets of results. This same departure is evident in the voltage capability space of Fig. 3.15. It takes on a slightly different shape, but the departure is still clear.

The results in Fig. 3.15 differ from those in Fig. 3.13 in that after the voltage correction loop is entered, the voltage at the receiving bus is low compared to the acceptable voltage limits. Therefore, the algorithm must continue to increase the receiving bus voltage. Conversely, in the previous trial, the result of the singular value loop produced a local voltage that was too high and the voltage correction loop had to decrease the receiving bus voltage. This shows that the voltage correction

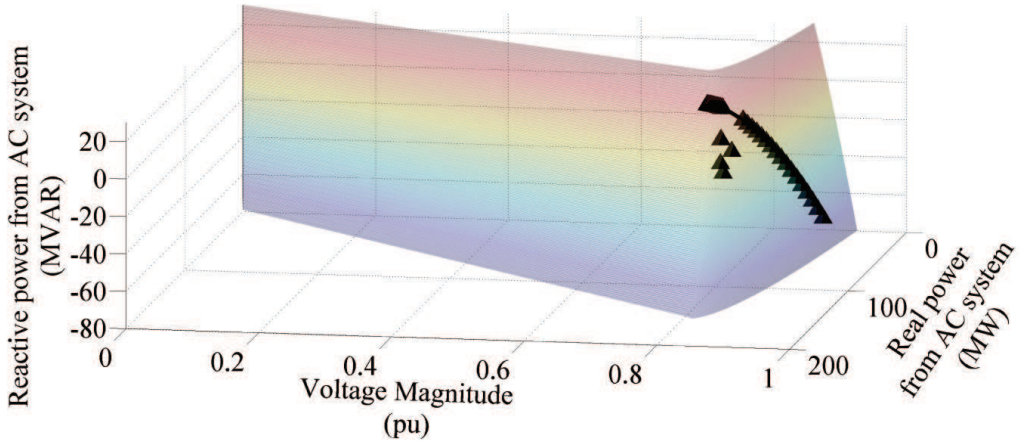

Figure 3.15: Voltage Capability Space for IEEE 118 Bus System with Voltage Correction.

loop provides correction in both directions for the results of the singular value loop. This is important because the operating point at the time the system is stressed may differ greatly in its positioning in the capability spaces. The SVS based control algorithm must be able to handle a range of operating condition and it is shown to do so.

3.5.3 Discussion on Computational Complexity

The proposed control algorithm has two main computational tasks: load flow and optimization. Computation statistics for the numerical trials are presented in Table 3.1 and Table 3.2 for the 118 bus LCQP and QCQP scenarios, respectively.

Table 3.1: LCQP Computation Statistics

Loop	Optimization (s)	Load Flow Sensitivities (s)	Load Flow Threshold Check (s)
Singular Value	.05348	69.296	26.2556
Voltage Correction	1.2881	86.601	33.6445

Table 3.2: QCQP Computation Statistics

Loop	Optimization (s)	Load Flow Sensitivities (s)	Load Flow Threshold Check (s)
Singular Value	1.2263	86.8932	24.3924
Voltage Correction	1.2681	115.678	31.7665

It is clear that the main computational expense in both scenarios (LCQP and QCQP) arises from the load flow calculations. To complete each load flow calculation Matpower version 4.0 was used with MATLAB R2011b (7.13.0.564) on a Lenovo laptop running Windows 7 64-bit operating system with an Intel i5 2.67 GHz processor. Commercial load flow software running on dedicated computers would be used in a practical implementation which would greatly reduce the computation time.

The computational cost of the optimization is much smaller compared to the load flow computational expense. The first reason for this is that the optimization is only run once per iteration. The second reason for this is that the size of the optimization problem is related to the number of control variables which is directly related to the number of VSC-HVDC links. In practical systems, the number of VSC-HVDC links is small (typically only a few at most), therefore, the optimization can be solved efficiently online.

3.5.4 Implementation Considerations

SVP control is intended to be implemented at a central location like a transmission control center. The algorithm utilizes as an input the real and reactive power injections at each bus. Because the steady-state voltage stability problem the algorithm is addressing is on the order of 5 minutes to 10 minutes, the injection values do not need to be instantaneous.

Further, the control input of the SVP algorithm will come from the state estimation. Therefore, this algorithm does not need another module for bad data detection and identification. It will use such routines from the state estimation package to obtain high fidelity input. Once the initial Jacobian is calculated using the values out of the state estimation, all signals are internal to the algorithm until the iterative process is complete and a control order for the VSC-HVDC system is calculated.

Also, it is intended that the SVP algorithm coexist with other actuation possibilities but the SVP algorithm does not consider them concurrently. As a first step, we assume that the SVP algorithm will be conducted before any generation re-dispatch. If the VSC-HVDC system is sufficient to move the system back to a safe state, as it is in the numerical trials, then only the VSC-HVDC system will be utilized. If it is not sufficient, than another actuation possibility must be considered prior to applying the SVP algorithm. It should be noted that there might be benefits in considering all control actions together in a coordinated manner, however, it is beyond the scope of this chapter and will be a fruitful direction for future investigation.

Finally, the ability to improve system wide SSVS utilizing VSC-HVDC is dependent on number, size and location. It is expected that in the siting and sizing of the VSC-HVDC system, its SSVS relief capabilities would be considered along with other technical benefits on different time scales.

3.6 Conclusion

The chapter presents a singular value sensitivity (SVS) based supplementary control algorithm that utilizes the capabilities of VSC based embedded HVDC for enhancing the voltage stability in AC power systems. The algorithm computes the optimal control policy for VSC power which simultaneously maintains the system voltage stability margin and bus-level voltage magnitude bounds. The approach is

to establish the sensitivity between the control input (i.e., the power injection at the VSC terminal) and voltage stability criteria (i.e., the smallest singular value of the load flow Jacobian). Based on the sensitivity, the optimal control policy is obtained via a quadratic programming algorithm.

This work also introduces the singular value capability space of the embedded VSC-HVDC system which builds intuition for system operators to visualize how much the embedded VSC-HVDC system can migrate the system away from voltage instability. Results from the case study on the IEEE 118 bus system suggest that the proposed control algorithm can migrate the system to a more secure operating point with respect to voltage stability, while the voltage correction loop maintains local voltage magnitudes to be within acceptable ranges. The computational complexity is shown to be linearly dependent on the order of the number of VSC embedded HVDC terminals and much less dependent on the bus number of the system. Therefore, the algorithm scales well for a large system.

4. IMPEDANCE MIMICRY CONTROL OF VSC-HVDC FOR POWER GRID SMALL SIGNAL STABILITY ENHANCEMENT

4.1 Introduction

In this chapter a novel approach to utilizing VSC-HVDC for improving large AC power grid dynamic performance is proposed. In particular, this work studies the problem of enhancing small signal stability in large power grids with the presence of VSC-HVDC.

Large AC power system small signal stability has been studied in great detail in the literature dating back all the way to 1920s [57]. More recently, with the increasing penetration of variable resources such as wind and solar, this area has received renewed interest, in particular with how to deal with power electronically interfaced generation in a grid with reduced inertia [58]. Modern systems like the Electric Reliability Council of Texas (ERCOT) are exposed to dynamic problems such as inter-area oscillations associated with long power transmission corridors that serve renewable generation centers [59, 60, 61].

In recent years, advance transmission devices like VSC-HVDC have been considered for a variety of grid enhancement roles including improving the grid small signal stability. Two main veins exist in this line of research, embedded and non-embedded VSC-HVDC system control. Non-embedded VSC-HVDC systems are more common in practice as the initial utilization of HVDC systems was for asynchronous grid connection. Non-embedded systems have the advantage of utilizing real power from another system for stabilization such as seen in [62] which utilizes the strength of a connecting grid to stabilize a weaker grid. Also studied have been AC concept emulation techniques like inertia and droop emulation [63, 64] which also benefit from

real power import/export. These non-embedded systems have also been shown to improve subsynchronous resonance [65].

Embedded HVDC systems, although less common in practice, have also garnered significant research interest for small signal stability enhancement. These systems do not have the ability to import or export real power which makes there control a bit more constrained. Grid stabilization techniques using wide area measurements have been explored utilizing linearized supplementary controllers [66, 67, 68]. The algorithms that do not rely on fast wide area measurements have also been developed using decentralization techniques [69].

Several observations emerge from the preceding discussion that motivate the work in this chapter:

1. Although long standing and well understood, small signal stability enhancement has renewed interest due to increased renewable penetration.

2. Advanced transmission devices are being seen more and more as tools that can improve dynamic performance of large power systems.

3. Some non-embedded control techniques for VSC-HVDC systems have featured emulation of AC concepts like droop and inertia that can aid in integration and adoption in real systems.

In this chapter a novel approach to supplementary control of VSC-HVDC systems for grid level small signal stability enhancement is proposed. Small Signal Impedance Mimicry (SSIM) and Enhanced Small Signal Impedance Mimicry (ESSIM) are introduced as AC concept emulation techniques which should aid in integration and adoption of these control features. The damping ratio analysis of the eigenvalues of the system state matrix for the interconnected system is used as a metric. The al-

gorithm aims to utilize updated operating conditions to find the optimal parameters for SSIM and ESSIM control.

The chapter is organized as follows. In Section II, small signal stability analysis and the general impedance mimicry concept is formulated. In Section III, the small signal impedance mimicry (SSIM) control for VSC-HVDC is described. In Section IV, enhanced small signal impedance mimicry (ESSIM) control for VSC-HVDC is introduced. Case studies in Section V on a small two-area system and the New England 39 bus system show promising results utilizing the proposed control strategies. Concluding remarks and future research directions are provided in Section VI.

4.2 Problem Formulation

4.2.1 Power System Small Signal Dynamical Models

The small signal analysis formulation used in this chapter can be found in [70]. The derivation begins with a multi-machine dynamic system represented by the differential algebraic equations (DAE) in (4.1)-(4.4),

$$\Delta\dot{x} = A_1\Delta x + B_1\Delta I_g + B_2\Delta V_g + E_1\Delta u \tag{4.1}$$

$$0 = C_1\Delta x + D_1\Delta I_g + D_2\Delta V_g \tag{4.2}$$

$$0 = C_2\Delta x + D_3\Delta I_g + D_4\Delta V_g + D_5\Delta V_l \tag{4.3}$$

$$0 = D_6\Delta V_g + D_7\Delta V_l \tag{4.4}$$

where, A_1, B_1, B_2, C_1, C_2, D_1, D_2, D_3, D_4, D_5, D_6, D_7, and E_1 are matrices representing the linearized sensitivities for the DAE model defined in [70]. The dynamic and algebraic state variables Δx, ΔI_g, ΔV_g, ΔV_l, and Δu are likewise defined in [70].

The derivation of the linear state matrix A_{sys} begins by defining K_1 and K_2 as shown in (4.5) and (4.6).

$$K_1 = D_4 - D_3 \cdot D_1^{-1} \cdot D_2 \tag{4.5}$$

$$K_2 = C_2 - D_3 \cdot D_1^{-1} \cdot C_1 \tag{4.6}$$

Then A', B', C', and D' are defined in (4.7), (4.8), (4.9), and (4.10), respectively.

$$A' = A_1 - B_1 \cdot D_1^{-1} \cdot C_1 \tag{4.7}$$

$$B' = \begin{bmatrix} B_2 - B_1 \cdot D_1^{-1} & 0 \end{bmatrix} \tag{4.8}$$

$$C' = \begin{bmatrix} K_2 \\ 0 \end{bmatrix} \tag{4.9}$$

$$D' = \begin{bmatrix} K_1 & D_5 \\ D_6 & D_7 \end{bmatrix} \tag{4.10}$$

The matrices A', B', C', and D' now include influences from the algebraic relationships of the grid connections of the various machines. This is what differentiates them from the set of matrices A, B, C, and D. Finally these primed matrices can be combined to create A_{sys} as shown in (4.11), which incorporates all the dynamics of the various machines and the algebraic relations of the connections at a given operating point into one system state matrix.

$$A_{sys} = A' - B' \cdot D'^{-1} \cdot C' \tag{4.11}$$

The state matrix A_{sys} will be the foundation of the small signal analysis presented here. The eigenvalues and eigenvectors of A_{sys} are utilized extensively not only

in analysis but also parameter selection for the proposed Enhanced Small Signal Impedance Mimicry (ESSIM) control introduced later.

4.2.2 Impedance Mimicry

The classic inter-area oscillation problem introduced in [7], centers around power transfer over a "weak" line, in other words over a high impedance connection. Typical real world solutions tend to focus on decreasing the effective impedance of these high impedance corridors through AC solutions like additional parallel lines and/or series compensation. In this section, a method to utilize a VSC-HVDC link to mimic impedance is introduced. This mimicked impedance can then be flexibly changed as needed for different operating conditions.

The derivation first begins with understanding how the real and reactive power summation at a bus is affected by the change of an impedance connected to it. The expressions for real and reactive power bus summation are shown in (4.12) and (4.13), respectively.

$$P_L(V_i) - \sum_{k=1}^{n} V_i V_k Y_{ik} cos(\theta_i - \theta_k - \alpha_{ik}) = 0 \tag{4.12}$$

$$Q_L(V_i) - \sum_{k=1}^{n} V_i V_k Y_{ik} sin(\theta_i - \theta_k - \alpha_{ik}) = 0 \tag{4.13}$$

An impedance connecting bus i and bus j can be defined by its admittance parameters as in (4.14) and (4.15).

$$y_{ij} = g_{ij} + jb_{ij} \tag{4.14}$$

or similarly as,

$$y_{ij} = |y_{ij}|\angle\alpha_{ij} \tag{4.15}$$

Utilizing the definition in (4.15), expressions for the real and reactive power flow over this connection can be defined as (4.16) and (4.17), respectively.

$$P_{ij} = |V_i|^2|y_{ij}|cos(-\alpha_{ij}) + |V_i||V_j||y_{ij}|cos(\theta_i - \theta_j - \alpha_{ij}) \tag{4.16}$$

$$Q_{ij} = |V_i|^2|y_{ij}|sin(-\alpha_{ij}) + |V_i||V_j||y_{ij}|sin(\theta_i - \theta_j - \alpha_{ij}) \tag{4.17}$$

If the injection/extraction of real and reactive power from this bus is actually supplied by the new "impedance" connection mimicked by the VSC-HVDC terminal the bus summation expression would change to that shown in (4.18) and (4.19),

$$P_L(V_i) - \sum_{k=1}^{n} V_i V_k Y_{ik} cos(\theta_i - \theta_k - \alpha_{ik}) + P'_{ij} = 0 \tag{4.18}$$

$$Q_L(V_i) - \sum_{k=1}^{n} V_i V_k Y_{ik} sin(\theta_i - \theta_k - \alpha_{ik}) + Q'_{ij} = 0 \tag{4.19}$$

where,

$$P'_{ij} = P^{(s)}_{DC} = P_{ij} \tag{4.20}$$

and,

$$Q'_{ij} = Q^{(s)}_{DC} = Q_{ij} \tag{4.21}$$

On the other end of the VSC-HVDC link, the receiving end injection/extraction

for real and reactive power would be similar, as shown in (4.22) and (4.23).

$$P'_{ji} = P^{(r)}_{DC} = P_{ji} \tag{4.22}$$

$$Q'_{ji} = Q^{(r)}_{DC} = Q_{ji} \tag{4.23}$$

It should be noted that because the "impedance" connection is mimicked by the VSC-HVDC link the parameters for this mimicked impedance in (4.16) and (4.17) can be chosen by the operator and more importantly, changed as operating conditions change.

4.2.3 Impedance Mimicry with Parallel AC Lines

In a real system, the mimicked impedance would most likely be parallel to the existing "weak" tie-line. In this scenario, the combined admittance can be found via (4.24).

$$Y'_{ij} = Y^{AC}_{ij} + Y^{DC}_{ij} \tag{4.24}$$

And, the control order for the VSC-HVDC link can be found via (4.25)-(4.28) for both the sending and receiving end of the line.

$$P^{(s)}_{DC} = P'_{ij} - P^{AC}_{ij} \tag{4.25}$$

$$Q^{(s)}_{DC} = Q'_{ij} - Q^{AC}_{ij} \tag{4.26}$$

$$P^{(r)}_{DC} = P'_{ji} - P^{AC}_{ji} \tag{4.27}$$

$$Q^{(r)}_{DC} = Q'_{ji} - Q^{AC}_{ji} \tag{4.28}$$

4.3 Small Signal Impedance Mimicry Control

Based on the time scales, the injection/extraction of a VSC-HVDC terminal into an AC grid can be conceived as a combination of a fixed steady-state value and small perturbations around that value as expressed in (4.29) and (4.30).

$$P_{DC}^{(i)} = P_{DC,0}^{(i)} + \Delta P_{DC}^{(i)} \tag{4.29}$$

$$Q_{DC}^{(i)} = Q_{DC,0}^{(i)} + \Delta Q_{DC}^{(i)} \tag{4.30}$$

Using this understanding, the expression for $\Delta P_{DC}^{(i)}$ implementing small signal impedance mimicry can be found by linearizing (4.16) around the current operating point to obtain (4.31).

$$\Delta P_{ij} = \frac{\partial P_{ij}}{\partial \theta_i}\Delta\theta_i + \frac{\partial P_{ij}}{\partial V_i}\Delta V_i + \frac{\partial P_{ij}}{\partial \theta_j}\Delta\theta_j + \frac{\partial P_{ij}}{\partial V_j}\Delta V_j \tag{4.31}$$

where,

$$\frac{\partial P_{ij}}{\partial \theta_i} = -|V_{io}||V_{jo}||y_{ij}|sin(\theta_{io} - \theta_{jo} - \alpha_{ij}) \tag{4.32}$$

$$\frac{\partial P_{ij}}{\partial V_i} = 2|V_{io}||y_{ij}|cos(-\alpha_{ij}) + |V_j||y_{ij}|cos(\theta_{io} - \theta_{jo} - \alpha_{ij}) \tag{4.33}$$

$$\frac{\partial P_{ij}}{\partial \theta_j} = |V_{io}||V_{jo}||y_{ij}|sin(\theta_{io} - \theta_{jo} - \alpha_{ij}) \tag{4.34}$$

$$\frac{\partial P_{ij}}{\partial V_j} = |V_{io}||y_{ij}|cos(\theta_{io} - \theta_{jo} - \alpha_{ij}) \tag{4.35}$$

Similarly, the small signal impedance mimicry expression for reactive power $\Delta Q_{DC}^{(i)}$, can be found via (4.36).

$$\Delta Q_{ij} = \frac{\partial Q_{ij}}{\partial \theta_i}\Delta\theta_i + \frac{\partial Q_{ij}}{\partial V_i}\Delta V_i + \frac{\partial Q_{ij}}{\partial \theta_j}\Delta\theta_j + \frac{\partial Q_{ij}}{\partial V_j}\Delta V_j \tag{4.36}$$

where,

$$\frac{\partial Q_{ij}}{\partial \theta_i} = |V_{io}||V_{jo}||y_{ij}|cos(\theta_{io} - \theta_{jo} - \alpha_{ij}) \tag{4.37}$$

$$\frac{\partial Q_{ij}}{\partial V_i} = 2|V_{io}||y_{ij}|sin(-\alpha_{ij}) + |V_j||y_{ij}|sin(\theta_{io} - \theta_{jo} - \alpha_{ij}) \tag{4.38}$$

$$\frac{\partial Q_{ij}}{\partial \theta_j} = -|V_{io}||V_{jo}||y_{ij}|cos(\theta_{io} - \theta_{jo} - \alpha_{ij}) \tag{4.39}$$

$$\frac{\partial Q_{ij}}{\partial V_j} = |V_{io}||y_{ij}|sin(\theta_{io} - \theta_{jo} - \alpha_{ij}) \tag{4.40}$$

Therefore, the small signal control order for the sending and receiving ends of the VSC-HVDC link can be expressed as,

$$\Delta P_{DC}^{(s)} = \Delta P_{ij}(y'_{DC}, \alpha'_{DC}) \tag{4.41}$$

$$\Delta Q_{DC}^{(s)} = \Delta Q_{ij}(y'_{DC}, \alpha'_{DC}) \tag{4.42}$$

$$\Delta P_{DC}^{(r)} = \Delta P_{ji}(y'_{DC}, \alpha'_{DC}) \tag{4.43}$$

$$\Delta Q_{DC}^{(r)} = \Delta Q_{ji}(y'_{DC}, \alpha'_{DC}) \tag{4.44}$$

where as shown in (4.41) - (4.44), the simulated line flow from bus i to bus j, and vice versa, are functions of the chosen line parameters y'_{DC} and α'_{DC}.

4.3.1 Small Signal Impedance Mimicry Implementation

The control diagram for SSIM control is shown in Fig. 4.1. In the figure the dotted lines are information signals while the solid lines are power connections. The SSIM control is intended for embedded VSC-HVDC systems. Voltage measurements are taken at each terminal and the signals are sent to the SSIM controller. The output of the SSIM control is added to the steady-state control orders from the primary steady-state controller. This is then sent to the converter stations to be implemented.

It is intended that the control center will be sending updated steady-state control signals that originate either via dispatch orders or other grid improvement strategies like those proposed in [71]. The control center can also update the parameter settings for the SSIM control as operating conditions change on the system.

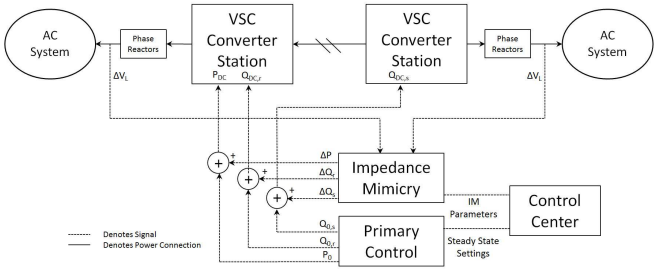

Figure 4.1: Small Signal Impedance Mimicry Control Diagram.

4.4 Enhanced Small Signal Impedance Mimicry Control

Small signal impedance mimicry control (SSIM) can be improved by better understanding what is happening to the eigenvalue positioning of the system state matrix A_{sys} when y'_{DC} and α'_{DC} are chosen to improve small signal dynamics.

What is occurring is that SSIM is changing the small signal sensitivities of real and reactive power injections at the connecting buses to the state variables θ_i, V_i, θ_j, and V_j. This small signal relationship is represented in (4.4). As y'_{DC} and α'_{DC} in SSIM control change, some changes to the sensitivities in (4.4) improve the eigenvalue positioning of A_{sys} and some worsen it. Therefore, if instead of choosing y'_{DC} and α'_{DC} for SSIM control, the key sensitivities of the state variables to the real and reactive power injections are chosen, SSIM control can be enhanced.

The key sensitivities for real power are $\frac{\partial P_i}{\partial \theta_i}$, $\frac{\partial P_i}{\partial \theta_j}$, $\frac{\partial P_j}{\partial \theta_i}$, and $\frac{\partial P_j}{\partial \theta_j}$. For reactive power, the key sensitivities are $\frac{\partial Q_i}{\partial V_i}$, $\frac{\partial Q_i}{\partial V_j}$, $\frac{\partial Q_j}{\partial V_i}$, and $\frac{\partial Q_j}{\partial V_j}$. Enhanced small signal impedance mimicry (ESSIM) aims to optimally and independently chose an adder to these sensitivities to better position the eigenvalues of the system state matrix A_{sys}. Eqns. (4.45) - (4.48) show how c_1, c_2, c_3, and c_4 are added to the existing sensitivities that affect the small signal injections of real and reactive power at bus i.

$$\frac{\partial P'_i}{\partial \theta_i} = \frac{\partial P_i}{\partial \theta_i} + c_1 \tag{4.45}$$

$$\frac{\partial P'_i}{\partial \theta_j} = \frac{\partial P_i}{\partial \theta_j} + c_2 \tag{4.46}$$

$$\frac{\partial Q'_i}{\partial V_i} = \frac{\partial Q_i}{\partial V_i} + c_3 \tag{4.47}$$

$$\frac{\partial Q'_i}{\partial V_j} = \frac{\partial Q_i}{\partial V_j} + c_4 \tag{4.48}$$

At the receiving end, bus j, equal and opposite changes to the sensitivities are shown in (4.49) - (4.52). This maintains the impedance mimicry and makes certain no net real power is exchanged between the HVDC system and the AC grid.

$$\frac{\partial P'_j}{\partial \theta_i} = \frac{\partial P_j}{\partial \theta_i} - c_1 \tag{4.49}$$

$$\frac{\partial P'_j}{\partial \theta_j} = \frac{\partial P_j}{\partial \theta_j} - c_2 \tag{4.50}$$

$$\frac{\partial Q'_j}{\partial V_i} = \frac{\partial Q_j}{\partial V_i} - c_3 \tag{4.51}$$

$$\frac{\partial Q'_j}{\partial V_j} = \frac{\partial Q_j}{\partial V_j} - c_4 \tag{4.52}$$

4.4.1 Optimal Control Step

In ESSIM, c_1, c_2, c_3, and c_4 are the chosen parameters instead of y'_{DC} and α'_{DC}. Choosing y'_{DC} and α'_{DC} is fairly straight forward, in that the small signal impedance is either increased or decreased to improved the eigenvalue positioning of the system state matrix A_{sys}. In ESSIM, an optimal control algorithm is proposed to choose the parameters c_1, c_2, c_3, and c_4.

Because of the highly non-linear relationship between the control parameters c_1, c_2, c_3, and c_4 and the positioning of the eigenvalues of A_{sys} an iterative process is used that has at its center an optimal control step.

In each step k, the optimization formulated in (4.53) is used. The objective function is a minimization of the control sensitivities, subject to several linear equality constraints, $G(x) = 0$.

$$\min_x \sum {c_1^{(k)}}^2 + {c_2^{(k)}}^2 + {c_3^{(k)}}^2 + {c_4^{(k)}}^2 \tag{4.53}$$

s.t.

$$G(x) = 0$$

The first set of linear equality constraints are those shown in (4.54) - (4.57) which relate the decision variables to the objective function in each iteration.

$$c_1^{(k)} = \Delta c_1 + c_1^{(k-1)} \tag{4.54}$$

$$c_2^{(k)} = \Delta c_2 + c_2^{(k-1)} \tag{4.55}$$

$$c_3^{(k)} = \Delta c_3 + c_3^{(k-1)} \tag{4.56}$$

$$c_4^{(k)} = \Delta c_4 + c_4^{(k-1)} \tag{4.57}$$

The key linear equality constraint is (4.58). It constrains the optimization to achieving a predefined damping ratio step, Λ in each step.

$$\Delta c_1 \cdot \Delta d_1 + \Delta c_2 \cdot \Delta d_2 + \Delta c_3 \cdot \Delta d_3 + \Delta c_4 \cdot \Delta d_4 = \Lambda \tag{4.58}$$

The first order sensitivities of Δc_1, Δc_2, Δc_3, and Δc_4 to the damping ratio of an oscillatory mode of interest (in this case inter-area oscillation) are Δd_1, Δd_2, Δd_3, and Δd_4. The sensitivity Δd_1 can be found via (4.59).

$$\Delta d_1 = \frac{re\{\lambda'_{new}\}}{\sqrt{re\{\lambda'_{new}\}^2 + imag\{\lambda'_{new}\}^2}} \tag{4.59}$$

where,

$$\lambda'_{new} = \lambda^{k-1} + \lambda_{sens} \tag{4.60}$$

Eq. (4.61) represents the eigenvalue sensitivity due to small changes in the system state matrix A_{sys}.

$$\lambda_{sens} = v_L^T \cdot A_{del} \cdot v_R \tag{4.61}$$

where,

$$A_{del} = A_{sys,o} - A_{sys}^{(k-1)} \tag{4.62}$$

Similarly, utilizing (4.59)- (4.62), Δd_2, Δd_3, and Δd_4 can be found.

4.5 Case Studies

4.5.1 Two Area System

In this section case studies are performed on the well-known 11 bus, two area system [7] to illustrate the efficacy of Small Signal Impedance Mimicry control and Enhanced Small Signal Impedance Mimicry control. The two-area system is displayed in Fig. 4.2. The steady-state parameters are based on those presented in [7]. The four generators are represented by the seventh order dynamic system found in [70] with the machine and exciter parameters found in Table 4.1 and Table 4.2, respectively. The machine dynamics parameters R_s and D for all machines are 0 and .01, respectively. Generator 1 and 2 are in area 1 and generator 3 and 4 are in area 2 and connected with a weak AC line as shown in Fig. 4.2. For the case studies the VSC-HVDC is connected in parallel the two AC lines connecting bus 7 and bus 8. For the base system analysis the VSC-HVDC system is assumed to have 0 MW and 0 MVAR output at steady-state and no dynamic controllers.

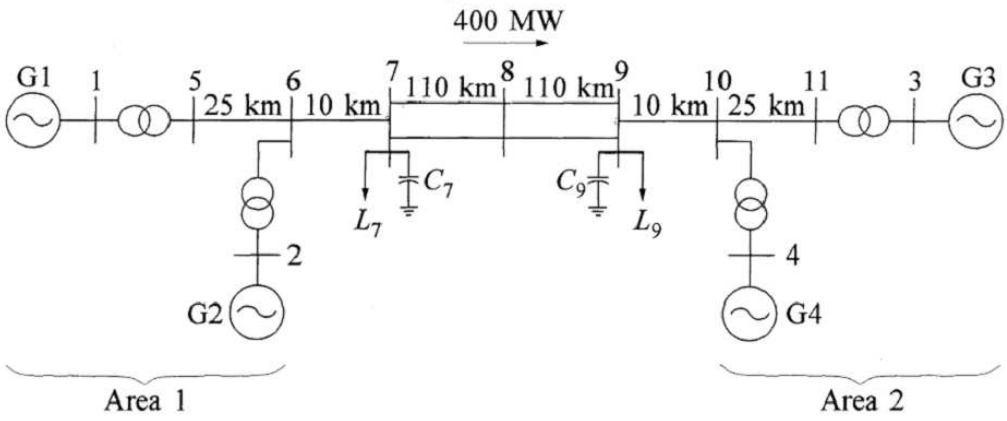

Figure 4.2: Two Area System [7].

Table 4.1: Two Area System Machine Dynamic Parameters

Gen #	X_d	X'_d	X_q	X'_q	H	T'_d	T'_q
1	1.8	.237	1.7	.55	6.5	8	.4
2	1.8	.237	1.7	.55	6.5	8	.4
3	1.8	.237	1.7	.55	6.5	8	.4
4	1.8	.237	1.7	.55	6.5	8	.4

Linear analysis of this base system, uncovers an expected inter-area oscillation with a frequency of .775 Hz with a damping ratio of 1%. The system is simulated at this operating point with a disturbance at 5 seconds. The disturbance is an input impulse change of the exciter voltage reference point on generator 1 of .03 pu. The time domain simulation of the system is shown in Fig. 4.3. It can be seen that the frequencies of generators 1 and 2 are oscillating against those of generators 3 and 4. It can also be seen from Fig. 4.3 that the inter-area oscillation settling time is quite long.

Table 4.2: Two Area System Exciter Parameters

Gen #	KA	TA	TE	KE	KF	TF
1	20	.055	.36	1	.125	1.8
2	20	.055	.36	1	.125	1.8
3	20	.055	.36	1	.125	1.8
4	20	.055	.36	1	.125	1.8

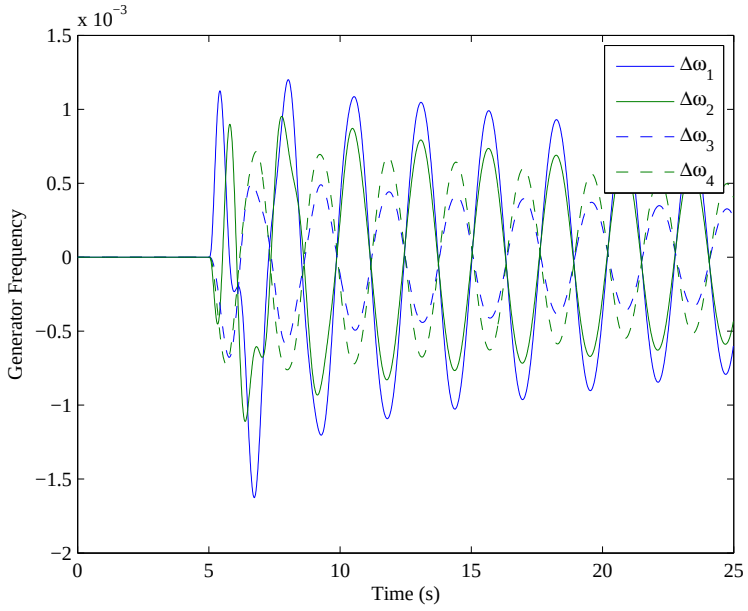

Figure 4.3: Base Case Inter-area Oscillation - Two Area System.

4.5.1.1 Small Signal Impedance Mimicry

To improve the damping of the inter-area oscillation seen in Fig. 4.3, Small Signal Impedance Mimicry control is engaged. To find the most appropriate tie line impedance a heuristic search is completed. The results of which are shown in Fig. 4.4. The dynamic impedance is shown on the x-axis.

In a fully AC system (no SSIM control) the dynamic impedance is the same as the steady-state impedance for the tie-line. The beginning dynamic impedance of

the AC tie line is .495 pu as shown on the far left of the graph. At that point the damping ratios for all the eigenvalues of the combined system are found on the y axis. The smallest damping ratio and that associated with the inter-area oscillation is at 1%.

To improve the damping of this oscillation the tie-line dynamic impedance is increased. The best damping achieved by SSIM control is 3.16% as is achieved when the combined AC and DC dynamic impedance is .815 pu. A damping ratio of 3% is considered industry standard [72] while other utilities allow even lower damping ratios [73]. Thus, with the inclusion of SSIM control at the tie-line the damping ratio has gone from unacceptable to acceptable.

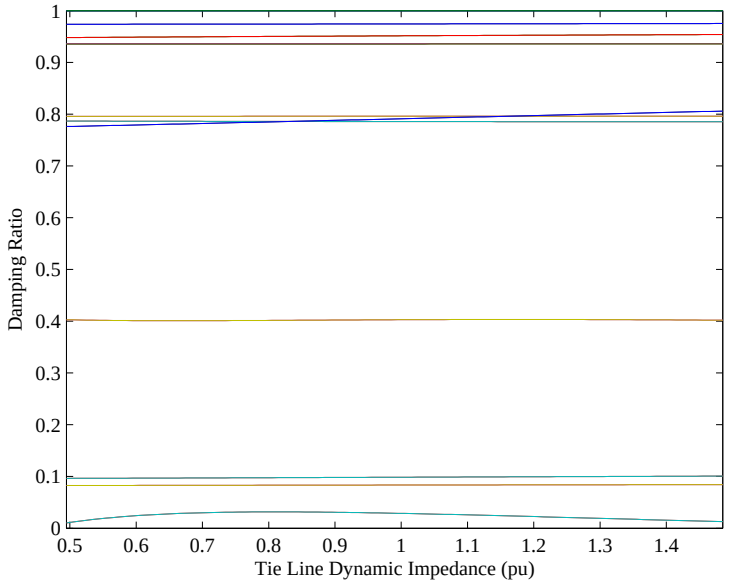

Figure 4.4: Small Signal Impedance Mimicry Damping Ratio.

Fig. 4.5 shows the time domain simulation of the generator frequency deviation of generator 1 for the base case with 1% damping and the improved system with

SSIM control included with 3% damping.

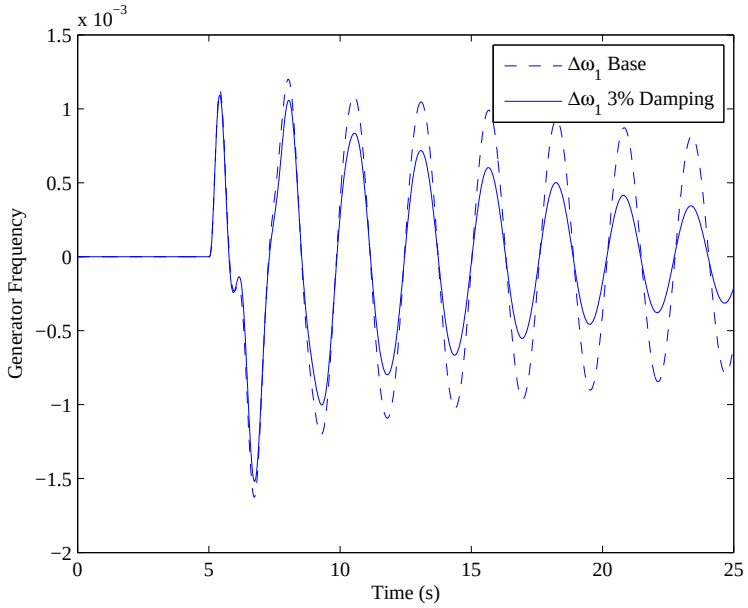

Figure 4.5: Base Case and 3 % Damping Case Time Simulation.

4.5.1.2 Enhanced Small Signal Impedance Mimicry

As discussed in Section 4.4, results can be improved by applying ESSIM which focuses more closely on the key sensitivities of an impedance connection. ESSIM control is applied to the same two area system introduced in Section 4.5.1. The parameters of the ESSIM control is not found heuristically as was the case for SSIM control but rather is found via (4.53) as introduced in Section 4.4. In the following trials, Case I is the base case with no ESSIM control. Case II, Case III and Case IV represent inter-area damping targets of 3%, 10%, and 20%, respectively. The results for the sensitivity parameters are shown in Table 4.3. It can be seen from the results that in Case II, the participation of sensitivity in the ESSIM control is fairly

consistent. While in Cases III and Case IV the c_2 sensitivity starts to play a much bigger role.

Table 4.3: EIM Sensitivities

	c1	c2	c3	c4
Case I	0	0	0	0
Case II	-.05131	.057901	.031797	.03593
Case III	-20208	.27805	.142195	.151358
Case IV	-.24744	.631753	.163953	.170199

The time domain simulations utilizing ESSIM control with the sensitivity parameters in Table 4.3 are shown in Fig. 4.6 with the frequency deviation of generator 1 on the y axis and the time on the x axis.

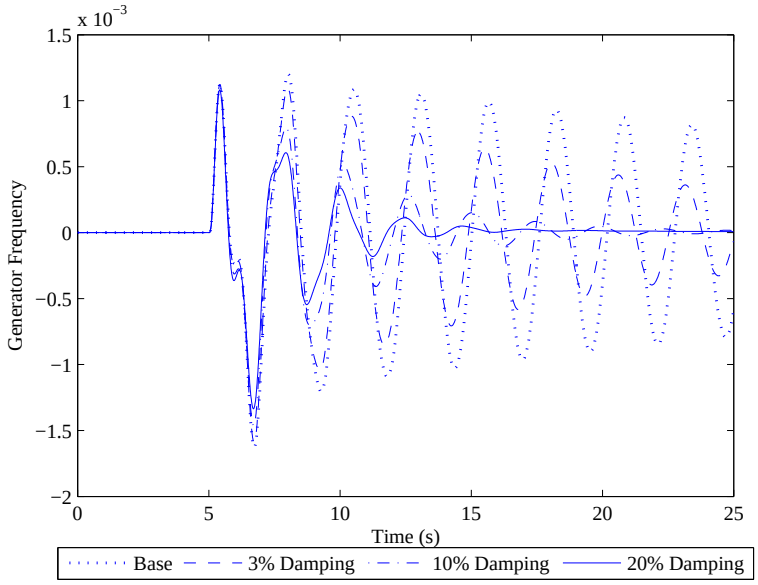

Figure 4.6: Enhanced Small Signal Impedance Mimicry Time Simulation.

4.5.2 39 Bus 10 Machine New England System

While the 3% damping of the inter-area oscillation in Case II would be sufficient for many systems, ESSIM control has the capability of achieving much faster settling of the inter-area oscillation. This is due not only to the capability of the algorithm but also to the placement of the VSC-HVDC terminals as well as the two area system configuration. To show the efficacy of the proposed ESSIM control the more complicated IEEE 39 bus New England system is introduced and tested. The configuration is shown in Fig. 4.7.

The New England system has 10 machines and an inter-area oscillation between the generators representing the New England system and generator 1 which represents the connection with the New York system. This is evident in the time domain simulation shown in Fig. 4.8.

There are two weak tie lines between the two areas. One tie line is between bus 39 and bus 31. The other is between bus 39 and 37. For the trials the VSC-HVDC terminals are connected between bus 39 and 31. The steady-state parameters for this system can be found in [8]. Small changes of note from this reference are as follows: 1) The bus numbers have been rearranged slightly; 2) Bus 1 real power demand has been changed from 1104 MW to 1954 MW to increase power transfer across the corridor; 3) Impedance values of line 1-31 have been changed so that line 39-31 represents the corridor. The dynamic models are the same as those used in the two area system with the machine and exciter parameters found in Table 4.4 and Table 4.5, respectively. Machine parameters R_s and D for all machines are 0 and .01, respectively.

Utilizing (4.53), parameters for the ESSIM control are found that satisfy an inter-area damping requirement of 5%. The time domain simulation showing the generator

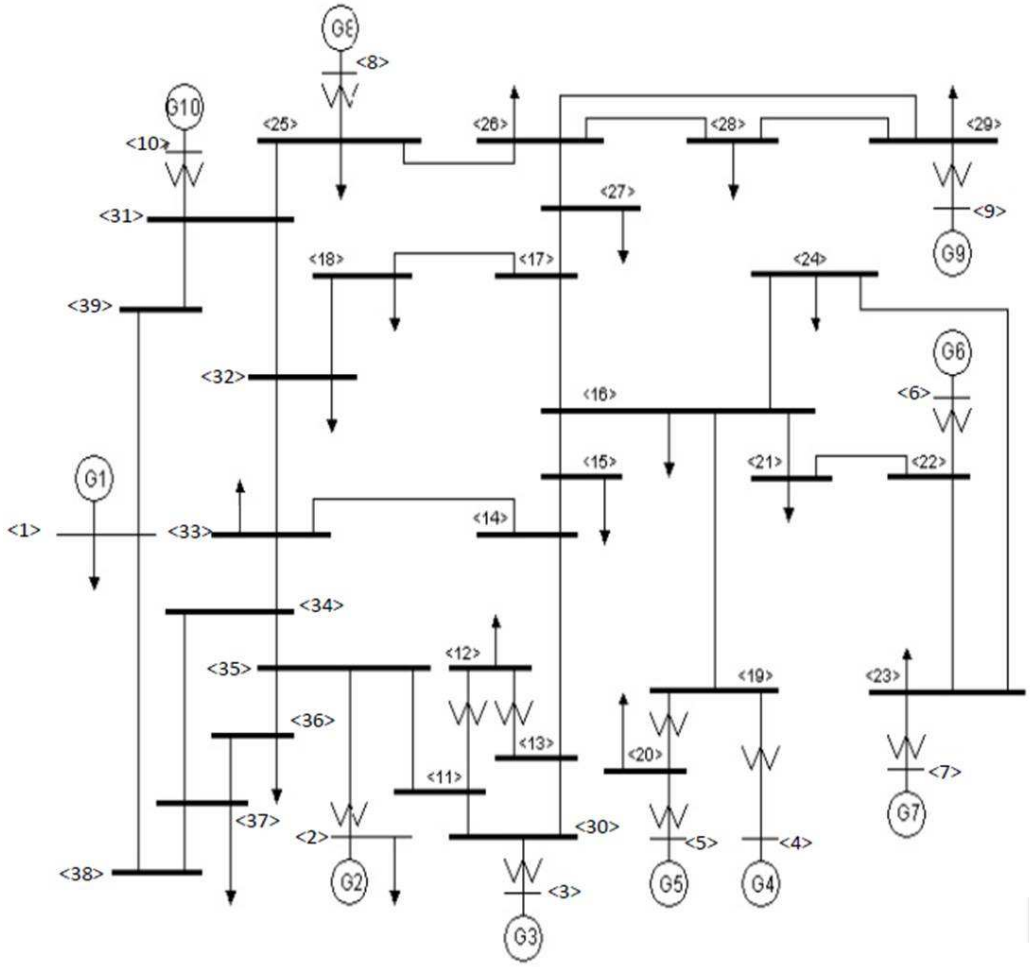

Figure 4.7: New England 39 Bus, 10 Machine System [8].

1 frequency deviation for the base case with no ESSIM control and the case with a 5% provided by ESSIM control is shown in Fig. 4.9. The disturbance is a voltage reference impulse change on the exciter of generator 10 and the disturbance occurs at 5 seconds.

It can be seen from Fig. 4.9 that with ESSIM control employed the oscillation is very quickly damped with respect to the base case.

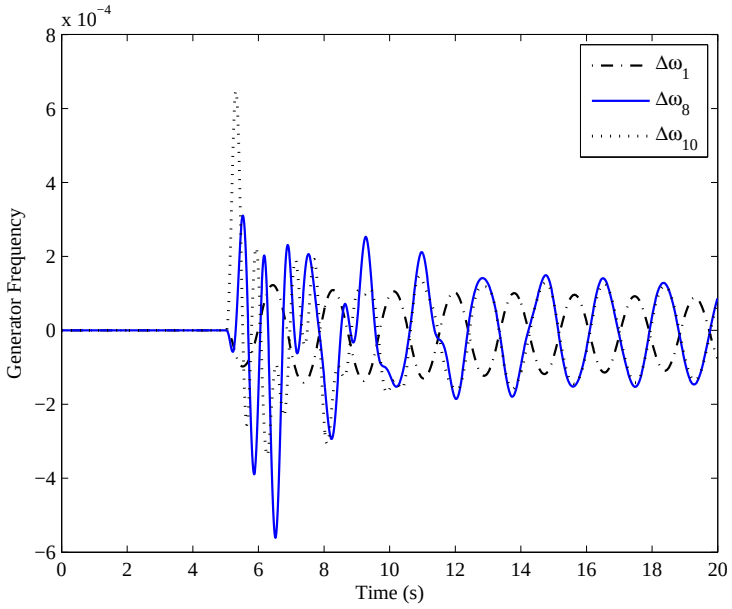

Figure 4.8: New England 39 bus System Inter-area Oscillation.

4.6 Conclusion

This work presents a novel control strategy based on an emulation of a well understood AC concept, impedance. Small Signal Impedance Mimicry (SSIM) control is a supplementary control that utilizes the flexibility of a embedded VSC-HVDC system to independently control real and reactive power at its terminals. Utilizing this feature, SSIM control can mimic a given impedance. The flexibility of the VSC-HVDC system also allows for the impedance to be separated into steady-state and dynamic (small signal) impedance. This frees up the control effort on the steady-state for the VSC-HVDC system to participate in other grid enhancement strategies aimed at steady-state control such as voltage stability improvement [71].

Enhanced Small Signal Impedance Mimicry (ESSIM) builds on the intuitiveness of SSIM and finds an optimal set of parameters for the VSC-HVDC supplementary control particular to the given operating point. Case studies performed on both

Table 4.4: New England System Machine Dynamic Parameters

Gen #	X_d	X'_d	X_q	X'_q	H	T'_d	T'_q
1	.02	.006	.019	.008	500	7	.7
2	.295	.0697	.282	.17	30.3	6.56	1.5
3	.2495	.0531	.237	.0876	35.8	5.7	1.5
4	.262	.0436	.258	.166	28.6	5.69	1.5
5	.67	.132	.62	.166	26	5.4	.44
6	.254	.05	.241	.0814	34.8	7.3	.4
7	.295	.049	.292	.186	26.4	5.66	1.5
8	.29	.057	.28	.0911	24.3	6.7	.41
9	.2106	.057	.205	.0587	34.5	4.79	1.96
10	.1	.031	.069	.008	42	10.2	1.5

Table 4.5: New England System Exciter Parameters

Gen #	KA	TA	TE	KE	KF	TF
1-10	20	.05	.36	1	.125	1.8

the two-area multi-machine system and the IEEE 39 bus New England system show promising results in utilizing the control for small-signal oscillation damping.

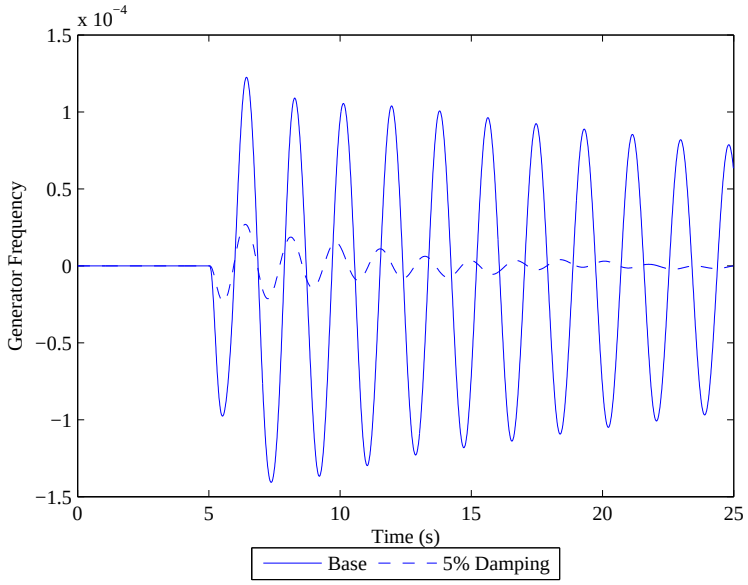

Figure 4.9: Enhanced Small Signal Impedance Mimicry Time Simulation - NE System.

5. MULTI-TIME SCALE TECHNO-ECONOMIC MAPPING: FRAMEWORK AND TECHNICAL CASE STUDIES

5.1 Introduction

New advanced transmission devices such as Flexible AC Transmission Systems (FACTS) and Voltage Source Converter based High Voltage DC (VSC-HVDC) provide a litany of technical benefits, unfortunately, these technical benefits sometimes come at a high monetary cost. This issue is one of many that have helped to relegate advanced transmission devices to technical niche applications rather than a standard planning alternative. In this section, a multi-time scale techno-economic benefit mapping framework is proposed to aid in better economic integration of advanced transmission devices like VSC-HVDC.

The addition of any device into a large power system will have both a technical and economic effect on the system. The impact of the effect depends on the nature and size of the device. From a technical stand point, each device will have different multi-time scale technical features. Some features may be more prominently showcased in one time-scale or another.

Conventional devices (i.e. transformers, AC lines, series & shunt compensators, generators, etc.) tend to have a mixed negative/positive, multi-time scale technical influence. With the inclusion of fast switching power electronics and fast controllers, new devices like FACTS and VSC-HVDC are able to influence multiple time scales more independently. Thus, whereas conventional devices might render technical benefits in one time scale and have adverse effects in another, these newer devices can utilize time-scale dependent control algorithms to maximize the positive influence seen on multiple time scales. The problem is how do you compare these multi-time

scale technical portfolios.

The proposed approach is to clearly map these technical benefits to their corresponding economic causes and economic effects. The end result will be a scalar metric by which all devices can be compared. Current industry standards only focus on steady-state power flow influences and their effects on system operating costs. The proposed approach will address multi-time scale technical benefits and the resulting economic causes and effects. This will provide clarity, transparency, and granularity allowing for a better one to one comparison of devices. This improved one to one comparison on multiple times scales will aid in the integration of advanced transmission devices into normal system planning and operation.

5.2 Mapping Design

Technical features included in the proposed approach are flow control, Quasi-steady-state voltage stability (QSVS), small signal stability, frequency support, and fast transient voltage stability. Economic causes include line flow limits, flexible line capacity, loss reduction, and decreased reliability must run (RMR) contracts. The economic effect is system operating cost which is made up of several components outlined in the following definitions:

$$C_{OP} = C_{EP} + C_{AS} + C_R \tag{5.1}$$

where,

$$C_{EP} = C_{ED} + C_{UC} \tag{5.2}$$

The economic benefit of a device could then be calculated as in (5.3) and compared one with the economic benefit of other devices.

$$B_{device} = C_{OP,orig} - C_{OP,new} \tag{5.3}$$

The multi-time scale techno-economic mapping framework is illustrated in Fig. 5.1.

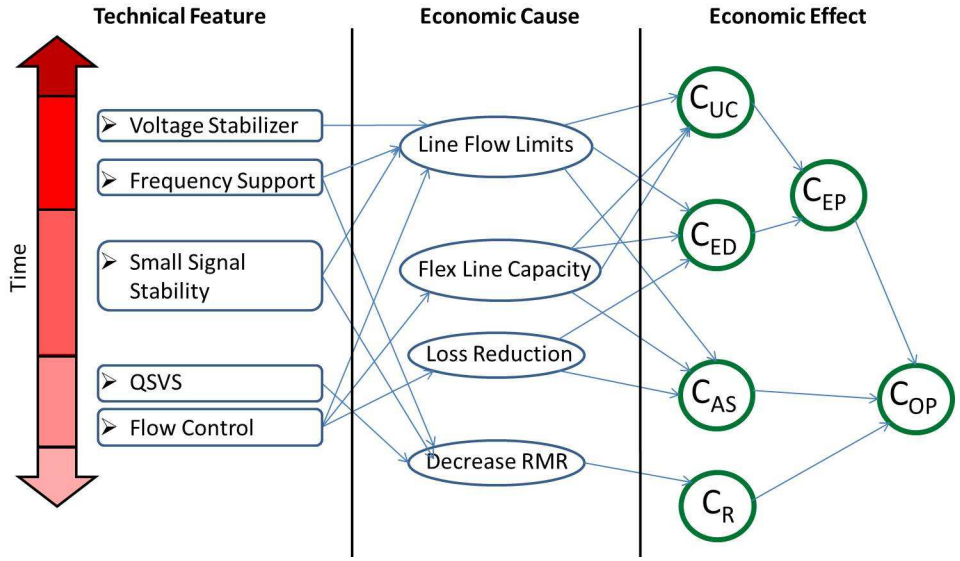

Figure 5.1: Techno-Economic Benefit Mapping.

The technical features are aligned from bottom to top from slower to faster power system phenomena. The arrows show the mapping connections between technical features, economic causes, and economic effects.

To illustrate the techno-economic mapping framework, combinations of Technical Features are chosen to create technical cases. The results of these technical cases are presented and discussed in this chapter. In the techno-economic mapping framework these results are termed Economic Causes. In chapter 6, these Economic Causes will filter through the economic benefit analysis and result in Economic Effects.

5.3 Technical Cases

Combinations of several technical features associated with a device make up the technical cases. The device chosen for the illustration is a two terminal VSC-HVDC

system. The multi-time scale technical features associated with the VSC-HVDC system and applied in the technical cases are steady-state flow control, Quasi-Static Voltage Stability (QSVS) improvement, and Small Signal Stability Enhancement. The algorithms used will be those introduced in other chapters including Singular Value Sensitivity (SVS) control for QSVS improvement and Enhanced Impedance Mimicry (EIM) control for improved small signal stability performance.

The system studied is the two area system described in chapter 4. This system is stressed by incrementing load in area 2 and compensating with generation in area 1. This is done to increase the tie-line flow from area 1 to area 2. This method exacerbates both the steady-state voltage stability and the small signal stability of the system. The smallest singular value of the reduced load flow Jacobian and the damping ratio of the small signal eigen-structure are found at each increment.

5.3.1 Multi-time Scale Stability Thresholds

5.3.1.1 Quasi-static Voltage Stability

The system is considered unstable in the steady-state voltage stability sense when the smallest singular value of the reduced load flow Jacobian becomes negative. In this work, this also corresponds to an inability to converge to a load flow solution. Most systems will not tolerate operating a system too near this stability limit so it is customary to operate with a limit that includes a 5% or 10% margin. This is the voltage stability threshold that is used as a limit in this work.

5.3.1.2 Small Signal Stability

The system is considered unstable in the small signal sense when the dynamic system linearized at a given operating has a positive damping ratio. The damping ratio has been defined in a previous chapter. Most systems will not operate near this limit so it is customary to have a damping ratio margin of 1%, 3% or 5% depending

on the system and oscillation considered. For the cases in this work, a 5% damping margin is utilized as the small signal stability threshold.

5.3.2 Case Descriptions

- Case 0
  - Case 0 is considered the base case. No HVDC system is connected.
- Case 1
  - In Case 1 a VSC-HVDC system is connected across the area 1 to area 2 corridor. The system is only used for real power transfer. The capacity of the real power transfer over the HVDC line is 100 MW.
- Case 2
  - Case 2 is the same as case 1 except that EIM control is utilized at each increment to improve the small signal stability limit.
- Case 3
  - Case 3 utilizes the steady-state flow control used in Case 1 and then utilizes the SVS control to improve the QSVS limit at each increment.
- Case 4
  - Case 4 is the same as Case 3 except that in each increment after the SVS control solution is implemented the EIM control is utilized to improve small signal stability.
- Case 5
  - Case 5 is the same as Case 4 except that the QSVS threshold is changed from the SSV=.6257 value which pertains to a 5% MW flow margin to SSV=1.

5.3.3 Technical Case Study Results

5.3.3.1 Case 0

The smallest singular value of the load flow Jacobian, representing how close the system is to the QSVS limit, for each iteration is shown versus the tie-line corridor flow in Figure 5.2a. Applying the 5% margin rule the QSVS limit is found to be 591 MW over the transfer corridor.

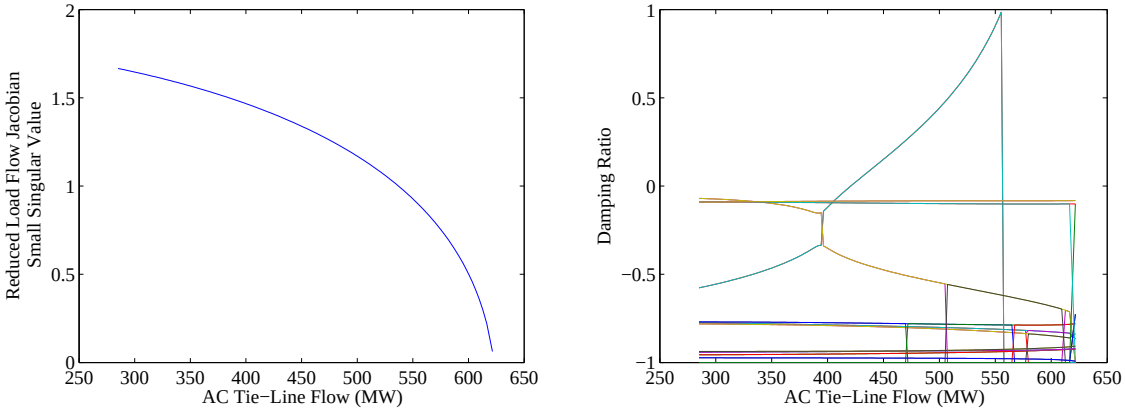

(a) Trajectory of SSV. (b) Trajectory of Damping Ratios.

Figure 5.2: Case 0: QSVS and Small Signal Time Scale Analysis

At each iteration the damping ratio of all the eigenvalues is found. When the damping ratios are plotted against the AC tie-line flow the results show a migration of key damping ratios. The small signal analysis results for Case 0 can be found in Figure 5.2b. The damping ratio threshold of 5% damping is applied to find the small signal transfer limit. As shown in Figure 5.2b the small signal stability transfer limit is 411 MW. The transfer limit of the corridor is the most restrictive limit and in Case 0 that is the small signal stability limit of 411 MW.

5.3.3.2 Case 1

The results for the Case 1 QSVS analysis are displayed in Figure 5.3a. The figure shows that the AC tie-line limit with 5% margin is 570 MW. This does not include the VSC-HVDC real power transfer of 100 MW. So the corridor limit which includes both the AC tie line flow and the VSC-HVDC real power transfer is 670 MW. It is interesting to note, and probably could have been predicted, that the addition of the 100 MW capacity for real power transfer via the VSC-HVDC line results in less than a 100 MW corridor transfer limit increase.

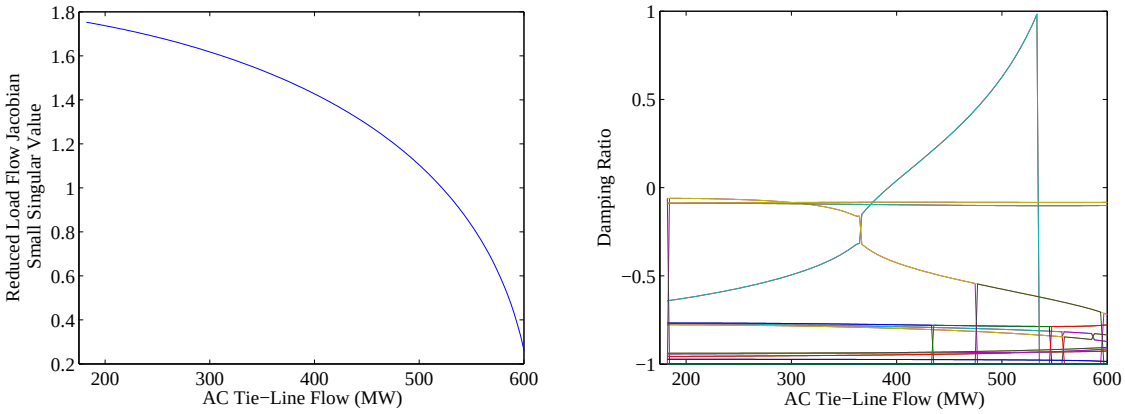

(a) Trajectory of SSV. (b) Trajectory of Damping Ratios.

Figure 5.3: Case 1: QSVS and Small Signal Time Scale Analysis

Figure 5.3b presents the small signal stability analysis for Case 1. The AC tie-line flow limit is 382 MW. Combining this with the VSC-HVDC real power transfer of 100 MW yields a corridor transfer limit of 482 MW. The binding limit again is the small signal stability limit. This results in a corridor transfer limit of 482 MW which is a 71 MW limit increase compared to Case 0. It is interesting to note that the

addition of 100 MW VSC-HVDC real power transfer only yields a corridor transfer limit of 71 MW.

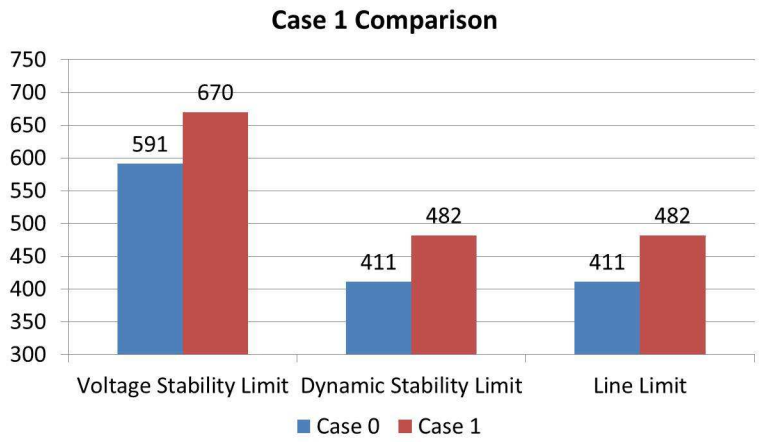

Figure 5.4: Case 1 vs Case 0.

Figure 5.4 shows the multi-time scale limits of Case 0 and Case 1 and how they result in the operating transfer limit for the corridor. It is easy to see from Figure 5.4 that although the addition of the 100 MW real power transfer increase the QSVS limit to 670 MW the limiting limit of small signal stability does not allow for this transfer value and is instead limiting the transfer to 482 MW.

5.3.3.3 Case 2

The results for the QSVS analysis in Case 2 are shown in Figure 5.5a. It can be seen that Figure 5.5a and Figure 5.3a of Case 1 are exactly the same. This makes sense because only the EIM control of the VSC-HVDC system is employed in Case 2. EIM does not change the steady-state injections of the VSC-HVDC system, thus the QSVS analysis should yield the same results. The Case 2 QSVS AC tie line transfer limit is 491 and thus the corridor transfer limit is 591 MW.

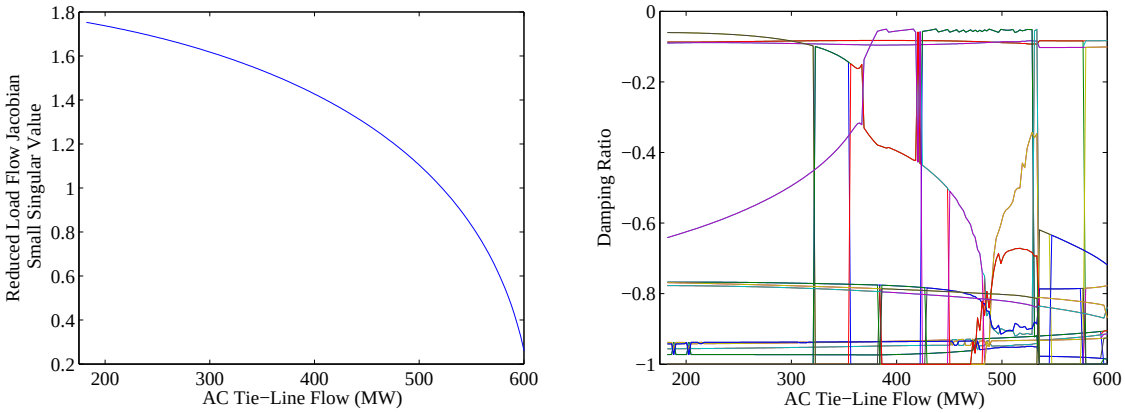

(a) Trajectory of SSV.

(b) Trajectory of Damping Ratios.

Figure 5.5: Case 2: QSVS and Small Signal Time Scale Analysis

The small signal stability analysis results for Case 2 are shown in Figure 5.5b. The data shown in Figure 5.5b is similar to that shown in Figure 5.3b of Case 1 until the AC tie line flow approaches 482 MW. At that point in Case 1 the critical eigenvalue which in this case represents an inter-area real power oscillation dips below the 5% damping ratio threshold. The EIM control engages and recalculates the necessary Impedance Mimicry parameters such that the resulting linearized system has a new damping ratio that is beyond the 5% threshold. In each iteration after that the EIM control is engaged and is able to produce a set of Impedance Mimicry parameters that result in a 5% damping. This is the case until the AC tie line flow reaches 533 MW. At that point the EIM fails to find a feasible solution that produces a 5% damping ratio of the inter-area oscillation. Combing the 533 MW flow over the AC tie line with the 100 MW real power transfer via the VSC-HVDC system yields a combined corridor transfer of 633 MW. This is slightly stricter than the QSVS transfer limit and thus is the corridor transfer operating limit. The results of Case 2 compared to Case 0 are shown in Figure 5.6.

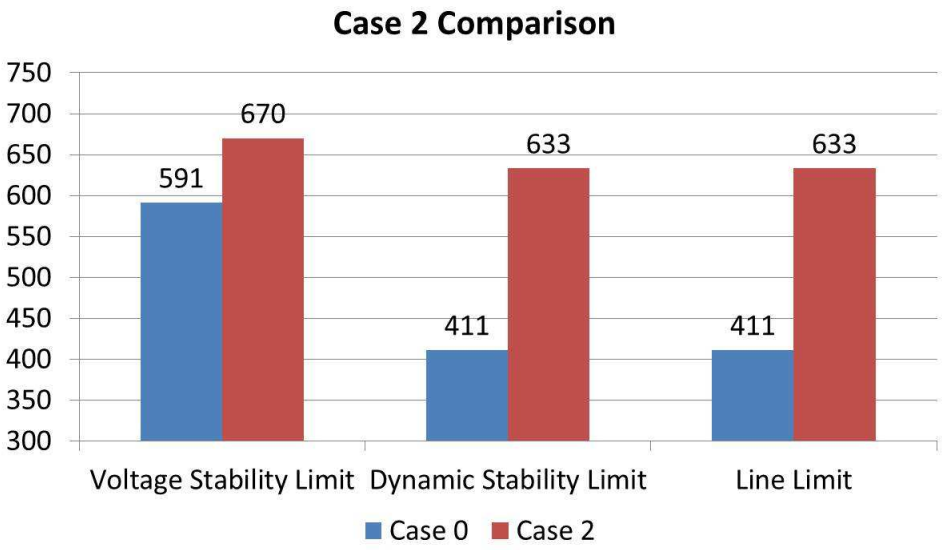

Figure 5.6: Case 2 vs Case 0.

As is shown in Figure 5.4 of Case 1 the QSVS has increased to 670 MW. In Case 2, the addition of the EIM algorithm has resulted in an increase of the overall corridor limit to 633 MW a 222 MW increase over the Case 0 result. This equates to a 54% increase in transfer capacity over the corridor.

5.3.3.4 Case 3

The QSVS analysis results for Case 3 are shown in Figure 5.7a. In Case 3, the SVS control is enabled which targets increasing the QSVS limit. The 5% margin threshold yields a smallest singular value threshold of .6257. As the iterations progress once the SSV dips below the threshold the SVS is engaged to improve the SSV to .6257. This is why in Figure 5.7a a flattening of the SSV curve can be seen around SSV= .6257. With the SVS engaged the QSVS limit has increased to 700 MW.

The small signal results for Case 3 are shown in Figure 5.7b. As can be seen in Figure 5.7b the data is similar to that shown in Figure 5.5b of Case 2 until the

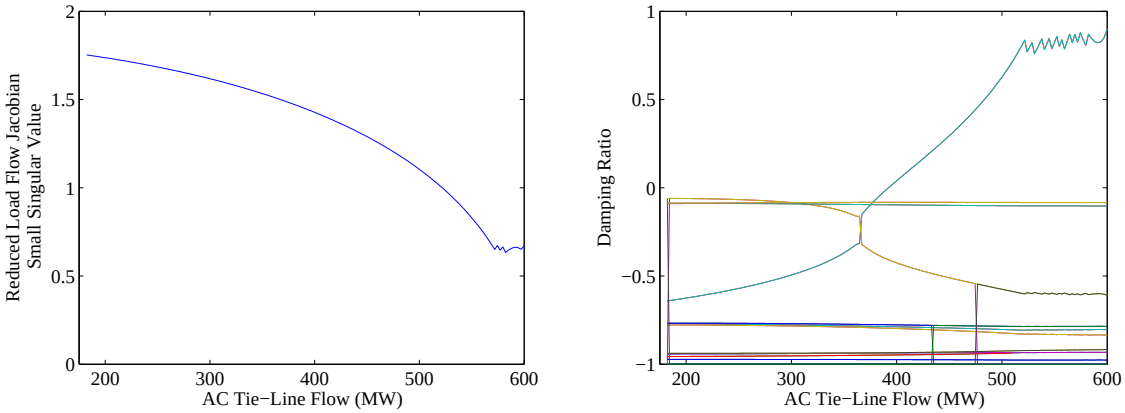

(a) Trajectory of SSV.

(b) Trajectory of Damping Ratios.

Figure 5.7: Case 3: QSVS and Small Signal Time Scale Analysis

SVS is engaged around the AC tie line flow of 521 MW. When the SVS is utilized it has an effect on the eigen structure of the system. This effect can be seen on the right of Figure 5.7b. Unfortunately, this effect is not enough to improve the critical eigenvalue before the damping ratio is beyond the operating threshold of 5% damping. Thus, in Case 3 the small signal stability limit for the AC tie line is still 382 MW resulting in a small signal stability corridor limit of 482 MW.

Figure 5.8 compares the results of Case 3 and Case 0. It can be seen from Figure 5.8 that the utilization of SVS has increased the QSVS stability 109 MW over Case 0. The small signal stability limit increase of 71 MW over Case 0 is the same as that shown in Case 1. Since the small signal stability limit is the binding limit for the corridor employing SVS control has not had a material effect on the operating limit of the corridor which is still just 482 MW, which is the same as if SVS had not be utilized.

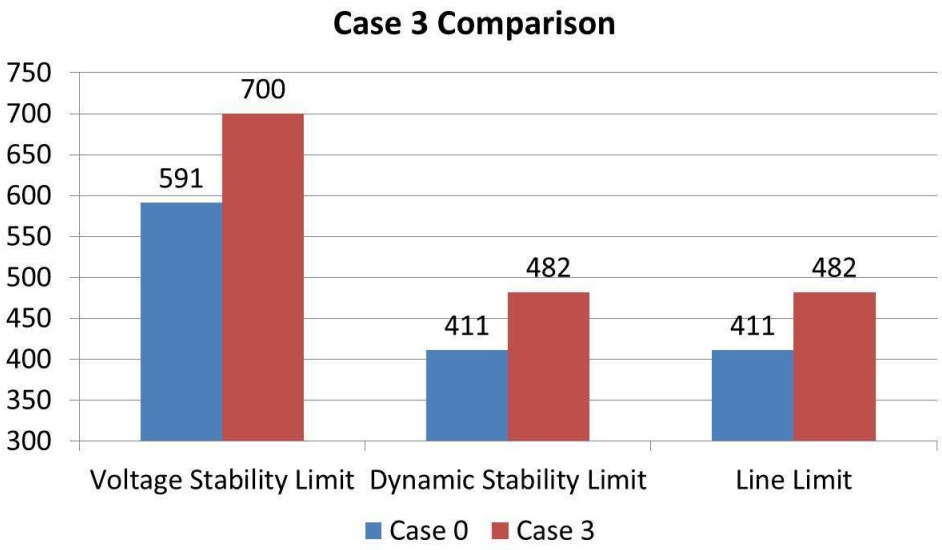

Figure 5.8: Case 3 vs Case 0.

5.3.3.5 Case 4

The QSVS analysis for Case 4 is presented in Figure 5.9a. The effect of SVS control can be seen on the right side of Figure 5.9a. It is similar to that seen in Case 3. With SVS engaged the QSVS AC tie line limit is 600 MW and thus the total corridor limit is 700 MW as is seen in Case 3.

The results of the small signal stability analysis are presented in Figure 5.9b. Figure 5.9b shows that the AC tie line flow limit for small signal stability is 533 MW. This makes small signal stability limit for the corridor 633 MW.

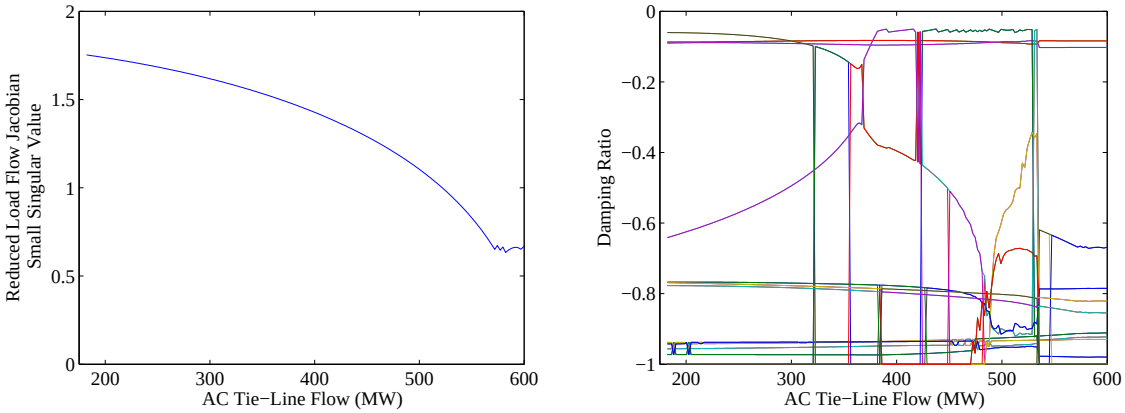

(a) Trajectory of SSV.

(b) Trajectory of Damping Ratios.

Figure 5.9: Case 4: QSVS and Small Signal Time Scale Analysis

The 633 MW small signal stability limit is smaller than the improved QSVS limit and thus is the binding operating limit for the corridor. This is evident in Figure 5.10.

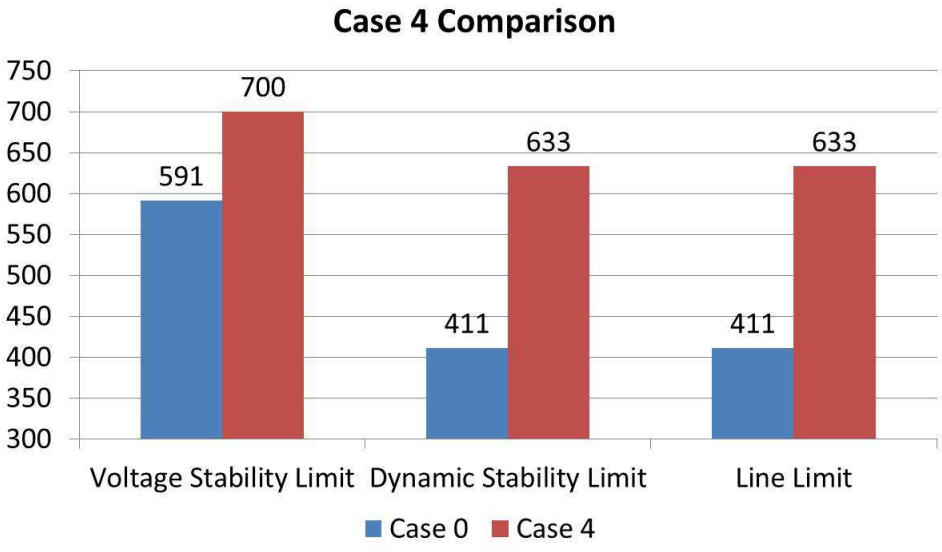

Figure 5.10: Case 4 vs Case 0.

Even though both the SVS and the EIM controls are engaged the binding limit for the corridor is still the same as Case 2. Comparing Figure 5.5b and Figure 5.9b, it can be seen that the SVS control is not engaged before the small signal stability limit has been reached. Thus the SVS control has no effect on the ability for the EIM control to increase the small signal stability transfer limit.

5.3.3.6 Case 5

The results for the QSVS analysis of Case 5 is presented in Figure 5.11a. The SVS control can be seen to have engaged when the AC tie line flow had reached around 522 MW. This is because Case 5 has a higher SSV threshold that the other cases. The previous cases utilizing SVS control had a SSV threshold equal to .6257 which corresponded to a 5% MW margin. In Case 5 the threshold was raised to SSV=1 so the SVS control engaged early in the iterations that in the previous cases. The importance of this becomes evident in the small signal stability analysis.

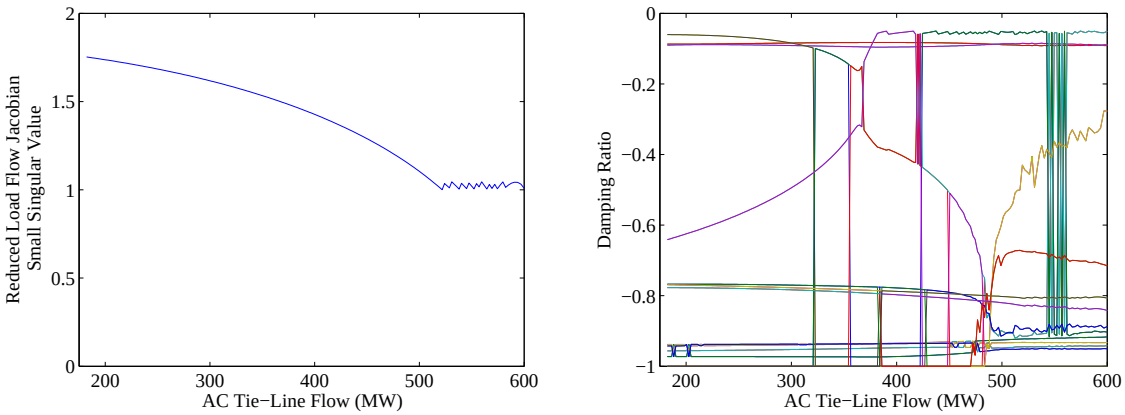

(a) Trajectory of SSV. (b) Trajectory of Damping Ratios.

Figure 5.11: Case 5: QSVS and Small Signal Time Scale Analysis

The small signal stability analysis results for Case 5 are presented in Figure 5.11b.

In Figure 5.11b the small signal stability limit for the AC tie line is shown to be 600 MW which means that the combined small signal stability corridor limit is 700 MW, a 67 MW improvement over the Case 4 small signal stability limit.

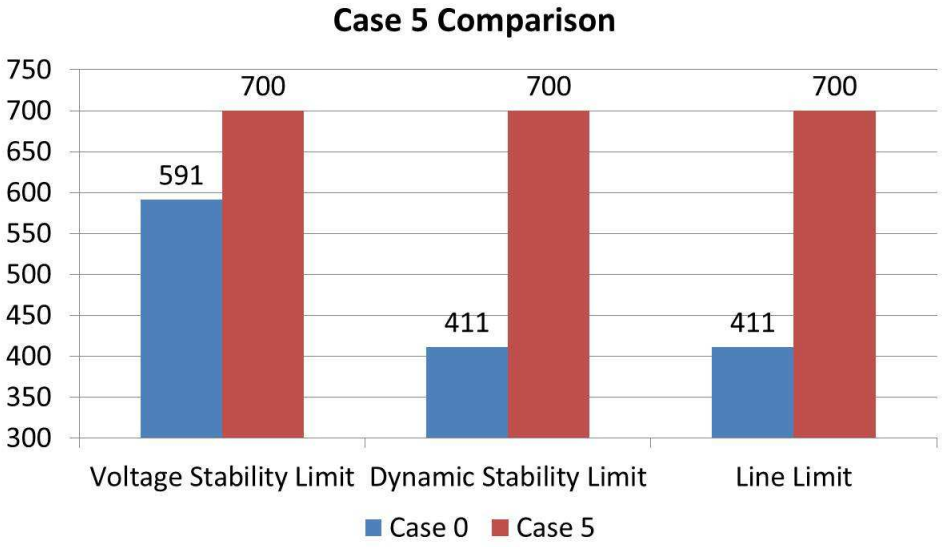

Figure 5.12: Case 5 vs Case 0.

The QSVS and small signal stability limits for Case 5 are shown compared to Case 0 in Figure 5.12. Since both the QSVS and small signal stability limit are 700 MW the line operating limit for the corridor is also 700 MW which is a 289 MW increase over Case 0. This means that the addition of a 100 MW VSC-HVDC system can improve the transfer capability of the corridor by 289 MW or 70%. Put another way, because of the multi-time scale technical abilities of the VSC-HVDC system, an addition of 25% steady-state transfer capability yields a corridor transfer limit increase of 70% or 2.8 times the actual installation.

6. MULTI-TIME SCALE TECHNO-ECONOMIC MAPPING: ECONOMIC CASE STUDIES

6.1 Introduction

In this chapter, the corridor limits found for each technical case are applied to the basic economic dispatch represented in Chapter 5. By first applying the technical features and then filtering the results through the given standard market system (in this case economic dispatch) the multi-time scale technical abilities of the given device can be translated into an economic effect. As discussed in the introduction to Chapter 5, this allows devices that render multi-time scale technical benefits to be faithfully compared to other devices without the need for markets for each time scale.

6.2 Basic Economic Dispatch Formulation

In this section a DC Optimal Power Flow (DCOPF) formulation is presented that will be used in the numerical case studies when the multi-time scale techno-economic mapping framework is applied. The development begins with the standard formulation for the reduced susceptance matrix in (6.1).

$$B_R = A \times diag(b) \times A^T \tag{6.1}$$

By combining the reduced susceptance matrix, the reduced incidence matrix and the branch susceptance vector in (6.2), the distribution factor matrix, H, can be obtained.

$$H = diag(b) \times A^T \times B_R^{-1} \tag{6.2}$$

The branch flow vector, F, is then obtained via (6.3) by multiplying the distribution factor matrix H by the nodal injection vector P.

$$F = H \times P \tag{6.3}$$

The economic dispatch of the mixed AC-DC system is formulated as follows:

$$\min_{x} \sum C \cdot x \tag{6.4}$$

s.t.

$$P_{Gi}^{MIN} \leq P_{Gi} \leq P_{Gi}^{MAX}, i \in G \tag{6.5}$$

$$P_{INJ,p} = -P_{EXT,q} \leq F_{DC}^{MAX} = F_i \tag{6.6}$$

$$|F| \leq F^{MAX} \tag{6.7}$$

$$\sum_{i \in G} P_{Gi} = \sum_{i \in L} P_{Li} \tag{6.8}$$

where, $x = [P_{Gi}, P_{inj}, P_{ext}, P_{AS,k}]$, $i \in G$ and $k \in A$, with G being the set of all generators, L being the set of all loads and A being the set of areas.

The dispatch is shown as a cost minimization with the decision variables being the real power generation of each generator, P_{Gi}, chosen from the set of all generators G and P_{INJ}, and P_{EXT}, the injection/extraction variables of the embedded VSC-HVDC system. Constraint (6.5) restricts the dispatch of the generators to a range in between their max and min operating limits. Constraint (6.6) restrict the steady-state flow of the VSC-HVDC to within limits. Constraint (6.7) restricts the branch flow to the limits of each branch based on the branch flow formulation presented. Constraint (6.8) maintains that the summation of the dispatched generation be equal to the scheduled load.

The two decision variables, P_{INJ}, and P_{EXT} are included at zero cost for the economic cases presented. This is considered sufficient for these trials but in further

work the cost can be used to incorporate the cost of losses on the DC line and any other marginal costs associated with the DC transmission.

6.3 Economic System for Economic Cases

In this section, parameters necessary for the economic dispatch scenario are created for the two area system in the technical cases. Table 6.1 shows the Capacity, Reserve Capacity, and Power Price for each of the 4 generators in the system. There

Table 6.1: Generator Economic Information

Generator Unit #	Capacity (MW)	Reserve Capacity (MW)	Power Price ($/MWh)
1	1200	400	35
2	700	0	28
3	1200	300	45
4	700	0	30

is also a demand response element in the system that can provide reserve capacity but does not provide power capacity. Table 6.2 shows the capacity of the demand

Table 6.2: Demand Response Information

Demand Response Unit #	Capacity (MW)	Reserve Capacity (MW)	Power Price ($/MWh)
1	0	50	2

response element to be 50 MW and the price of this reserve capacity should it be procured is $2/MW. Table 6.3 shows the demand and reserve requirements in each area.

6.4 Economic Case Results

6.4.1 Case 0

To create a base line by which to compare the multi-time scale techno-economic benefits of the added VSC-HVDC, the results of the Case 0 dispatch is found and shown in Table 6.4.

Table 6.3: Area Operational Information

Area	Load (MW)	Reserve (MW)
1	850	300
2	1900	350

Table 6.4: Case 0 Dispatch Results

Dispatched Unit	Power Dispatch (MW)	Capacity Available (MW)	Procured Reserve (MW)	Reserve Price ($/MW)	C_{EP} ($)	C_{AS} ($)
Gen 1	511	689	350	0	17,885	0
Gen 2	700	0	0	0	19,600	0
Gen 3	839	361	300	10	37,775	3,000
Gen 4	700	0	0	10	21,000	0
DR 1	0	0	0	2	0	0
Total	2750	1050	650	-	96,240	3000

Generators 2 and 4 have power prices of $28/MWh and $30/MWh, respectively. They are dispatched to their full capacity or 700 MW each. The next cheapest alternative is generator 1 with a power price of $35/MWh. It is dispatched only to 511 MW. The reason is that the inter-area power flow at this dispatched reaches the Case 0 tie line flow limit of 411 MW. Thus, the remaining generation must be produced by generator 3 at $45/MWh. It can already be seen that if the corridor transfer limit can be increased then economic value can be realized. The current dispatch results in a Cost of energy Procurement (CEP) of $96,240.

Generators 1 and 3 are the only units that can provide reserve. With the current power dispatch the reserve requirement in each area can be fulfilled by generator 1 and 3 for their respective areas. The price of this reserve is the incremental cost of the procurement of an additional unit of reserve. In area 1 an additional unit of reserve

can easily be served by generator 1 without a change in the power dispatch result, so the reserve price for area 1 is \$0/MW. For area 2 the only option for one additional unit of reserve is from generator 1. With the current dispatch the generator 1 cannot supply the additional unit because the corridor limit has already been reached. So, in order to supply one additional unit of reserve for area 2, the generator 1 power dispatch must be reduced by 1 MW to relieve the corridor congestion. Consequently the power dispatch of generator 2 must be increased. The net cost to the system is \$10. This is the price of reserve in area 2. So the total cost for reserve, the Cost of Ancillary Services (CAS) is \$3,000.

6.4.2 Case 1

In Case 1 with the addition of 100 MW steady-state power flow control via the VSC-HVDC system the corridor limit has increased to 482 MW. The redispatch of the system in Case 1, presented in Table 6.5, yields a slightly lower C_{EP} of \$95,530 and a slightly lower CAS of \$2,920. In Case 1 both generator 2 and 4 are fully dispatched in the same way they are in Case 0. The marginal units are still generator 1 and 3. The increase in the corridor limit allows for more power to be produced from generator 1 and transferred to area 2. Replacing MWs produced by generator 3 with ones produced by generator 1 is the cause for the decrease in CEP. The CAS also has decreased. The reason for this is that the VSC-HVDC system allows for a temporary overload of 10% which is sufficient for ancillary services. The cost of the demand response is only \$2/MW and can replace procurement of 10 MW of reserve from generator 3. This accounts for a decrease in CAS of \$100.

6.4.3 Case 2

The multi-time scale technical features utilized in Case 2 have increased the corridor limit to 633 MW. The dispatch results for Case 2 taking into account the

Table 6.5: Case 1 Dispatch Results

Dispatched Unit	Power Dispatch (MW)	Capacity Available (MW)	Procured Reserve (MW)	Reserve Price ($/MW)	C_{EP} ($)	C_{AS} ($)
Gen 1	582	618	350	0	20,370	0
Gen 2	700	0	0	0	19,600	0
Gen 3	768	432	290	10	34,560	2,900
Gen 4	700	0	0	10	21,000	0
DR 1	0	0	10	2	0	20
Total	2750	1050	650	-	95,530	2920

increased corridor limit is presented in Table 6.6. The same economic mechanism is at play in this dispatch as was in the Case 1 results. The increased line limit has allowed generator 1 to produce more thus decreasing the amount produced by generator 3. The cost delta for each MW is $10. The new dispatch is 733 MW for generator 1 and 617 MW for generator 3. The dispatch results for generators 2 and 4 are still the same at 700 MW. The total cost of energy procurement, CEP, in this case is $94,020 which a decrease of $2,220 versus Case 0 and a decrease of $1,510 for energy procurement. This cost decrease is an economic benefit that can be directly attributed to the additional small signal stability improvement ability of the added VSC-HVDC.

The ancillary services procurement result is the same in Case 2 as it was in Case 1. The decrease in the cost of ancillary services is $80 versus Case 0. This brings the total cost difference to $2,300 decrease in the operating cost of the system versus Case 0 for the addition of a VSC-HVDC line with 100 MW steady-state flow control and small signal stability enhancement capabilities.

Table 6.6: Case 2 Dispatch Results

Dispatched Unit	Power Dispatch (MW)	Capacity Available (MW)	Procured Reserve (MW)	Reserve Price ($/MW)	C_{EP} ($)	C_{AS} ($)
Gen 1	733	467	350	0	25,655	0
Gen 2	700	0	0	0	19,600	0
Gen 3	617	583	290	10	27,765	2,900
Gen 4	700	0	0	10	21,000	0
DR 1	0	0	10	2	0	20
Total	2750	1050	650	-	94,020	2920

6.4.4 Case 3

The dispatch results for case 3 are the same as those in Case 1. Technically, Case 3 is different than the other previous cases but the technical result with respect to the system is still the same as Case 1. Put another way, the technical feature that increases the QSVS limit does not actually improve the operation of the system. So although the feature can boast a MW increase in the QSVS limit it cannot boast a tangible improvement to the system. The techno-economic mapping framework makes this distinction clear.

Further, had there been a market for QSVS improvements, the technical feature employed in Case 3 would have be a beneficiary of this market. Its improvement, though, would not have a real tangible effect on the operation of the system. This is clear with the techno-economic mapping framework. Dispatching the system with the economic cause achieved by the technical feature employed in Case 3 leads to the same economic result. Thus, it can concluded that employing the SVS control for enhancing QSVS on top of the steady-state flow control has not economic value with respect to the steady-state flow control employed alone.

6.4.5 Case 4

Case 4 employs 3 time scale technical features: 1) flow control; 2) QSVS improvement; and 3) SSS performance enhancement. The results of employing all 3 technical features has no tangible difference when compared to the results of Case 2 which employs only the steady-state flow control and the SSS performance improvement. The resulting economic cause in Case 4 is the same at that in Case 2, so in the same way Case 3 will have the same economic effect as Case 1, Case 4 will have the same economic effect as that found in Case 2. The techno-economic mapping again makes this evident. The additional technical feature has no economic value with respect to those employed in Case 2.

6.4.6 Case 5

Case 5 employs the same technical features employed in Case 4 but does so with a slightly higher SSV threshold for the SVS control algorithm. This change allows for the QSVS technical feature to positively contribute to the improvement realized by the EIM control. So although in this case the change in threshold does not increase the QSVS limit, it contributes to increasing the SSS limit, which in this case is the binding limit. This contributes to increasing the corridor transfer limit to 700 MW which will create an improved economic cause. The results for the dispatch of Case 5 are presented in Table 6.7.

Table 6.7: Case 5 Dispatch Results

Dispatched Unit	Power Dispatch (MW)	Capacity Available (MW)	Procured Reserve (MW)	Reserve Price ($/MW)	C_{EP} ($)	C_{AS} ($)
Gen 1	800	400	350	0	28,000	0
Gen 2	700	0	0	0	19,600	0
Gen 3	550	650	290	10	24,750	2,900
Gen 4	700	0	0	10	21,000	0
DR 1	0	0	10	2	0	20
Total	2750	1050	650	-	93,350	2920

The new CEP is $93,350 which is a decrease of $2,890 versus the Case 0 CEP and a total COP cost decrease of $2,970. Thus, the addition of all 3 technical features (flow control, QSVS improvement, SSS performance enhancement) has an economic value of $2,970 to the system. Further, the addition of the QSVS improvement and SSS performance enhancement technical features, which result in technical improvements in two additional time scales, have an economic value of $2,180 (Case 5 versus Case 1). Finally, comparing Case 5 and Case 2, a value of $670 can be attributed to the addition of the SVS control with the adjusted SSV threshold.

6.4.7 Economic Case Result Summary

Table 6.8 compares all the economic results for the pertinent technical cases discussed above. The table displays the cost decrease with respect to the base cases in fifth column. The sixth column shows this cost decreases in a percentage of the original dispatch cost. Case 1 which only utilizes the steady-state flow control

ability of the VSC-HVDC obtains a dispatch cost decrease of $790 which represents a percentage decrease of .8%. Adding only the small signal impedance mimicry control technical feature increases cost savings to $2,300 or 2.32%.Utilizing all three technical features tested (steady-state flow control, small signal impedance mimicry, and QSVS enhancement) in a somewhat coordinated manner, the dispatch cost savings arrives at $2,970 or 2.99%.

Table 6.8: Economic Case Summary

	C_{EP} ($)	C_{AS} ($)	C_{OP} ($)	Decrease ($)	Decrease (%)
Case 0	96,240	3,000	99,240	0	0
Case 1	95,530	2,920	98,450	790	.8
Case 2	94,020	2,920	96,940	2,300	2.32
Case 5	93,350	2,920	96,270	2,970	2.99

From these results a few observations can be made:

1. It is evident that a considerable amount of savings is not being realized when a multi-scale technical device like the VSC-HVDC does not have its multi-time scale technical benefits fully utilized.

2. The economic benefit of a device with multi-time scale technical benefits may not be fully appreciated in planning scenarios if only steady-state impacts are considered. Cases 2 and Cases 5 show two fold economic improvements over Case 1 which only considers steady-state flow control.

3. The proposed techno-economic mapping framework makes clear the economic impact of each additional time-scale technical benefit which will aid in integra-

tion of flexible devices that may have additional costs for additional time-scale technical features.

7. CONCLUSIONS AND DIRECTIONS FOR FUTURE RESEARCH

In this chapter, the dissertation is concluded by 1) summarizing the research; and 2) discussing several directions for future work.

7.1 Dissertation Summary

To address improved integration of a new device like VSC-HVDC, one must address many aspects. One of the most important aspects addressed in this dissertation is integration within power system planning stages. We address this by proposing the Smart Targeted Planning (STP) algorithm. The algorithm utilizes a line shadow price-based weighting approach to rank the potential economic impact of incorporating a new VSC-based HVDC link along existing transmission lines. The economic benefit calculated by the proposed algorithm is compared to an exhaustive heuristic searching algorithm (EHS) and the results are presented. When applied to the ERCOT-equivalent 24 bus system and an IEEE 118 bus system, the proposed algorithm predicts absolute values for dispatch cost decrease that are very similar to that found by the time intensive EHS. Most importantly, the STP method suggests the same top ten candidates for line upgrades, many of which are non-intuitive choices.

The dissertation also presents several technological algorithms that take advantage of the VSC-HVDC systems ability to provided grid level technical benefits independently in multiple time scales. Along these lines, we first present an algorithm that utilizes this flexibility to improve voltage stability in the quasi-static time scale. The singular value sensitivity (SVS) based supplementary control algorithm for a VSC-HVDC system utilizes an approach to establish the sensitivity between the control input (i.e., the power injection at the VSC terminal) and voltage stability criteria (i.e., the smallest singular value of the load flow Jacobian). Based on the

sensitivity, an optimal control policy is obtained via a quadratic programming algorithm. We also propose an analysis framework called the singular value capability space of the embedded VSC-HVDC system, which aims to build intuition for system operators to visualize how much the embedded VSC-HVDC system can migrate the system away from voltage instability.

Results from case studies on the IEEE 118 bus system suggest that the proposed control algorithm can migrate the system to a more secure operating point with respect to voltage stability in the quasi-static time scale, while the voltage correction loop maintains local voltage magnitudes to be within acceptable ranges. Scalability is also suggested by results that show the computational complexity is linearly dependent on the order of the number of VSC embedded HVDC terminals and not the bus number of the system.

Another technological algorithm proposed that takes advantage of the VSC-HVDC system's ability to provide grid level technical benefits independently in multiple time scales is the small signal impedance mimicry control (SSIM). The proposed algorithm enhances grid level stability on the small signal time scale. It is presented as a novel control strategy based on an emulation of a well understood AC concept, impedance. This supplementary control utilizes the flexibility of a embedded VSC-HVDC system to independently control real and reactive power at its terminals. Utilizing this feature, SSIM control can mimic any given impedance. The flexibility of the VSC-HVDC system also allows for the impedance to be separated into steady-state and dynamic (small signal) impedance, freeing up control effort in the steady-state time scale for the VSC-HVDC system to participate in other grid enhancement strategies aimed at steady-state control such as voltage stability improvement [71].

Also presented is the Enhanced Small Signal Impedance Mimicry (ESSIM) which

builds on the intuitiveness of SSIM and finds an optimal set of parameters for the VSC-HVDC supplementary control particular to the given operating point. Case studies performed on both the two-area multi-machine system and the IEEE 39 bus New England system show promising results in utilizing the control for small-signal oscillation damping.

Lastly, a strong comparison framework is proposed that ends the apples to oranges comparison norm that occurs when different power system devices are compared that have differing multi-time scale technical ability portfolios. The multi-time scale techno-economic mapping framework helps to take the guess work out of power system device comparison. A case study is presented that shows how this framework is applied to the VSC-HVDC system. The case study begins with applying several of the multi-time scale grid enhancement algorithms proposed in this dissertation in order to provide technical benefits to the case study system. These technical benefits are then mapped to a standard economic framework. The result is a economic benefit analysis of the multi-time scale benefits of the VSC-HVDC system. The framework is developed such that it is generalizable and can be applied to any device with a multi-time scale portfolio with the resulting metric for comparison being the economic benefit to the system.

7.2 Future Research

A device like the VSC-HVDC system has a rich base that goes far beyond what can be presented in this dissertation. Several extensions to the work already presented in this dissertation are described below.

The line of research in Smart Targeted Planning can be extended to include other flow control devices. The focus will then move to incorporate advanced devices like VSC-HVDC and FACTS controllers into other times scales that may affect SCED

and provide not only system reliability and stability benefits but also monetary benefits via further dispatch cost decrease. Recommendations can also be provided for operation and policy regimes that will increase potential incorporation of these devices in such manners.

The SVS based control research can be extended in a way that it is applicable to other power system devices that have strong technical effects within the quasi-static time scale. The analysis framework of the singular value capability space can be applied to other devices and show their effects within the quasi-static voltage stability time scale. A coordinated approach to optimal control of these devices will also greatly benefit the power grid.

A worthwhile extension to the multi-time scale techno-economic mapping framework would be a larger techno-economic case study that applies the framework to several power system devices across several study systems. This would provide an even stronger case for the efficacy of the proposed framework.

REFERENCES

[1] CIGRE. (2005) B4 HVDC and Power Electronics, Working Group B4-37, VSC Transmission, CIGRE Tech. [Online]. Available: http://b4.cigre.org/Publications/Technical-Brochures/TB-269-2005-SC-B4-WG-B4.37-VSC-Transmission

[2] IIT. (2004) IEEE 118-bus Unit and Network Data. [Online]. Available: https://www.motor.ece.iit.edu

[3] P. Kumkratug, "Power-voltage characteristics of power system with the short transmission line," *American Journal of Applied Sciences*, vol. 9, no. 6, p. 906, 2012.

[4] ERCOT. (2013) System Operating Limit Methodology for Planning Horizon. [Online]. Available: https://www.ercot.com/

[5] ——. (2009) System Operating Limit Methodology for Operations Horizon. [Online]. Available: https://www.ercot.com/

[6] B. Lee and K. Lee, "Dynamic and static voltage stability enhancement of power systems," *IEEE Trans. Power Syst.*, vol. 8, no. 1, pp. 231–238, 1993.

[7] P. Kundur, N. J. Balu, and M. G. Lauby, *Power system stability and control*. McGraw-hill New York, 1994, vol. 7.

[8] Ueda. (2003) IEEE 10 Generator 39 Bus System. [Online]. Available: http://sys.elec.kitami-it.ac.jp/ueda/demo/WebPF/39-New-England.pdf

[9] C. Grigg, P. Wong, P. Albrecht, R. Allan, M. Bhavaraju, R. Billinton, Q. Chen, C. Fong, S. Haddad, S. Kuruganty *et al.*, "The ieee reliability test system-1996. a report prepared by the reliability test system task force of the application

of probability methods subcommittee," *Power Systems, IEEE Transactions on*, vol. 14, no. 3, pp. 1010–1020, 1999.

[10] R. Brown, "Planning a 13,800-volt subtransmission system," *Electrical Engineering*, vol. 69, no. 8, pp. 678–678, 1950.

[11] K. Smith and E. Michelson, "A 66-kv subtransmission plan," *Electrical Engineering*, vol. 68, no. 12, pp. 1059–1059, Dec. 1949.

[12] J.-C. Kaltenbach, J. Peschon, and E. Gehrig, "A mathematical optimization technique for the expansion of electric power transmission systems," *IEEE Trans. Power App. Syst.*, no. 1, pp. 113–119, Jan. 1970.

[13] C. Serna, J. Duran, and A. Camargo, "A model for expansion planning of transmission systems a practical application example," *IEEE Trans. Power App. Syst.*, no. 2, pp. 610–615, Apr. 1978.

[14] M. Farrag and M. El-Metwally, "New method for transmission planning using mixed-integer programming," in *Generation, Transmission and Distribution, IEE Proceedings C*, vol. 135, no. 4. IET, 1988, pp. 319–323.

[15] A. Meliopoulos, R. Webb, R. Bennon, and J. Juves, "Optimal long range transmission planning with ac load flow," *IEEE Trans. Power App. Syst.*, no. 10, pp. 4156–4163, Oct 1982.

[16] A. Seifu, S. Salon, and G. List, "Optimization of transmission line planning including security constraints," *IEEE Trans. Power Syst.*, vol. 4, no. 4, pp. 1507–1513, Oct. 1989.

[17] J. A. Momoh, Y. Wang, M. Elfayoumy, B. Mittelstadt, S. Agarwal, and R. Adapa, "A value-based reliability enhancement scheme for bulk transmis-

sion system planning," *IEEE Trans. Power Syst.*, vol. 13, no. 4, pp. 1541–1547, Nov. 1998.

[18] J. Dalton III, D. Garrison, and C. Fallon, "Value-based reliability transmission planning," *IEEE Trans. Power Syst.*, vol. 11, no. 3, pp. 1400–1408, Aug. 1996.

[19] A. Chowdhury and D. O. Koval, "Application of customer interruption costs in transmission network reliability planning," in *Industrial and Commercial Power Systems Technical Conference, 2001. Conference Record. Papers Presented at the 2001 Annual Meeting. 2001 IEEE*, 2001, pp. 53–60.

[20] G. Shrestha and P. Fonseka, "Congestion-driven transmission expansion in competitive power markets," *IEEE Trans. Power Syst.*, vol. 19, no. 3, pp. 1658–1665, Aug. 2004.

[21] FERC, *Transmission Planning and Cost Allocation by Transmission Owning and Operating Public Utilities.* FERC Order 1000, 2011.

[22] A. David and F. Wen, "Transmission planning and investment under competitive electricity market environment," in *Power Engineering Society Summer Meeting, 2001*, vol. 3. IEEE, 2001, pp. 1725–1730.

[23] ERCOT. (2013) ERCOT Planning Guide Section 3: Regional Planning. [Online]. Available: https://www.ercot.com/

[24] Z. Lu, M. Li, W. Tang, and Q. Wu, "Optimal location of facts devices by a bacterial swarming algorithm for reactive power planning," in *Evolutionary Computation, 2007. CEC 2007. IEEE Congress on*, 2007, pp. 2344–2349.

[25] P. Kuruganty and D. Woodford, "A reliability cost-benefit analysis for hvdc transmission expansion planning," *IEEE Trans. Power Del.*, vol. 3, no. 3, pp. 1241–1248, Jul. 1988.

[26] T. J. Overbye, X. Cheng, and Y. Sun, "A comparison of the ac and dc power flow models for lmp calculations," in *System Sciences, 2004. Proceedings of the 37th Annual Hawaii International Conference on.* IEEE, 2004, pp. 9–pp.

[27] ABB. (2011) Developments in Multiterminal HVDC. [Online]. Available: https://www.ieee.ca/epec11/admin/04-0800-hvdc_plenary_jacobson.pdf

[28] Tres Amigas LLC. (2013) The Tres Amigas Superstation. [Online]. Available: https://http://www.tresamigasllc.com/presentations-files.php

[29] H. Pang, G. Tang, and Z. He, "Evaluation of losses in VSC-HVDC transmission system," in *2008 IEEE Power and Energy Society General Meeting-Conversion and Delivery of Electrical Energy in the 21st Century*, 2008, pp. 1–6.

[30] R. Sellick and M. Åkerberg, "Comparison of HVDC Light (VSC) and HVDC Classic (LCC) site aspects, for a 500MW 400kV HVDC transmission scheme," 2012.

[31] O. Urquidez and L. Xie, "Targeted conversion of ac lines to dc lines for improved power system dispatch," in *North American Power Symposium (NAPS).* IEEE, 2012, pp. 1–6.

[32] Y. Gu, L. Xie, B. Rollow, and B. Hesselbaek, "Congestion-induced wind curtailment: Sensitivity analysis and case studies," in *North American Power Symposium (NAPS).* IEEE, 2011, pp. 1–7.

[33] ERCOT. (2010) ERCOT 2010 Capacity, Demand and Reserves Report. [Online]. Available: https://www.ercot.com/

[34] ——. (2010) ERCOT peak demand surpasses new June record. [Online]. Available: http://www.ercot.com/news/press_releases/show/26237

[35] ——. (2013) ERCOT 2013 Planning, Long-term Hourly Peak Demand and Energy Forecast. [Online]. Available: https://www.ercot.com/

[36] "Final report of the investigation committee of the 28 September 2003 blackout in italy," UCTE, Tech. Rep., 2004.

[37] J. Pan, R. Nuqui, K. Srivastava, T. Jonsson, P. Holmberg, and Y.-J. Hafner, "AC grid with embedded VSC-HVDC for secure and efficient power delivery," in *Energy 2030 Conference, 2008. ENERGY 2008. IEEE.* IEEE, 2008, pp. 1–6.

[38] S. G. Johansson, G. Asplund, E. Jansson, and R. Rudervall, "Power system stability benefits with VSC DC-transmission systems," in *CIGRE Conference, Paris, France*, 2004.

[39] I. Smon, G. Verbic, and F. Gubina, "Local voltage-stability index using Tellegen's theorem," *IEEE Trans. Power Syst.*, vol. 21, no. 3, pp. 1267–1275, 2006.

[40] C. Bai, M. Begovic, R. Nuqui, D. Sobajic, and Y. Song, "On voltage stability monitoring with voltage instability predictors," in *Bulk Power System Dynamics and Control - IX Optimization, Security and Control of the Emerging Power Grid (IREP), 2013 IREP Symposium*, 2013, pp. 1–8.

[41] D. Bedoya, C. Castro, and L. da Silva, "A method for computing minimum voltage stability margins of power systems," *Generation, Transmission Distribution, IET*, vol. 2, no. 5, pp. 676–689, 2008.

[42] A. Sode-Yome, N. Mithulananthan, and K. Lee, "A maximum loading margin method for static voltage stability in power systems," *IEEE Trans. Power Syst.*, vol. 21, no. 2, pp. 799–808, 2006.

[43] V. Ajjarapu and C. Christy, "The continuation power flow: a tool for steady state voltage stability analysis," *IEEE Trans. Power Syst.*, vol. 7, no. 1, pp. 416–423, 1992.

[44] M. K. Pal, "Voltage stability conditions considering load characteristics," *IEEE Trans. Power Syst.*, vol. 7, no. 1, pp. 243–249, 1992.

[45] P. Sauer and M. A. Pai, "Power system steady-state stability and the load-flow jacobian," *IEEE Trans. Power Syst.*, vol. 5, no. 4, pp. 1374–1383, 1990.

[46] P.-A. Lof, G. Andersson, and D. Hill, "Voltage stability indices for stressed power systems," *IEEE Trans. Power Syst.*, vol. 8, no. 1, pp. 326–335, 1993.

[47] L. Zhang, H.-P. Nee, and L. Harnefors, "Analysis of stability limitations of a VSC-HVDC link using power-synchronization control," *IEEE Trans. Power Syst.*, vol. 26, no. 3, pp. 1326–1337, 2011.

[48] B.-T. Ooi, "Feasibilty, stability, and voltage collapse in weak back-to-back HVDC links," *IEEE Trans. Power Del.*, vol. 1, no. 3, pp. 211–217, 1986.

[49] Y. Shao and Y. Tang, "Voltage stability analysis of multi-infeed HVDC systems using small-signal stability assessment," in *Transmission and Distribution Conference and Exposition, 2010 IEEE PES*, 2010, pp. 1–6.

[50] D. Aik and G. Andersson, "Use of participation factors in modal voltage stability analysis of multi-infeed HVDC systems," *IEEE Trans. Power Del.*, vol. 13, no. 1, pp. 203–211, 1998.

[51] X.-P. Zhang, L. Yao, B. Chong, C. Sasse, and K. Godfrey, "FACTS and HVDC technologies for the development of future power systems," in *Future Power Systems, 2005 International Conference on*, Nov 2005, pp. 6 pp.–6.

[52] Z. Huang, B. T. Ooi, L.-A. Dessaint, and F. Galiana, "Exploiting voltage support of voltage-source HVDC," *Generation, Transmission and Distribution, IEE Proceedings-*, vol. 150, no. 2, pp. 252–256, 2003.

[53] L. Nogal, "Damping of power swings in large-scale ac power system by simultaneous control of HVDC links and series FACTS devices," in *PowerTech (POWERTECH), 2013 IEEE Grenoble*. IEEE, 2013, pp. 1–6.

[54] ——, "Enhancing stability of a weakly connected ac power system by supplementary control of embedded HVDC lines," in *Environment and Electrical Engineering (EEEIC), 2013 12th International Conference on*. IEEE, 2013, pp. 64–71.

[55] T. Van Cutsem and C. Vournas, *Voltage stability of electric power systems*. Springer, 1998, vol. 441.

[56] R. D. Zimmerman, C. E. Murillo-Sánchez, and R. J. Thomas, "Matpower: Steady-state operations, planning, and analysis tools for power systems research and education," *IEEE Trans. Power Syst.*, vol. 26, no. 1, pp. 12–19, Feb. 2011.

[57] C. Fortescue, "Transmission stability analytical discussion of some factors entering into the problem," *American Institute of Electrical Engineers, Transactions of the*, vol. 44, pp. 984–1003, 1925.

[58] J. Conto, "Grid challenges on high penetration levels of wind power," in *Power and Energy Society General Meeting, 2012 IEEE*. IEEE, 2012, pp. 1–3.

[59] J. Adams, C. Carter, and S.-H. Huang, "Ercot experience with sub-synchronous control interaction and proposed remediation," in *Transmission and Distribution Conference and Exposition (T&D), 2012 IEEE PES*. IEEE, 2012, pp. 1–5.

[60] B. Badrzadeh, M. Sahni, D. Muthumuni, Y. Zhou, and A. Gole, "Sub-synchronous interaction in wind power plantspart i: Study tools and techniques," in *Power and Energy Society General Meeting, 2012 IEEE*. IEEE, 2012, pp. 1–9.

[61] M. Sahni, B. Badrzadeh, D. Muthumuni, Y. Cheng, H. Yin, S. Huang, and Y. Zhou, "Sub-synchronous interaction in wind power plants-part ii: an ercot case study," in *Power and Energy Society General Meeting, 2012 IEEE*. IEEE, 2012, pp. 1–9.

[62] S.-Y. Ruan, G.-J. Li, T. Lie, and S.-S. Choi, "Improving power system damping by utilizing vsc-hvdc," in *Power and Energy Society General Meeting, 2012 IEEE*. IEEE, 2012, pp. 1–6.

[63] J. Zhu, C. D. Booth, G. P. Adam, A. J. Roscoe, and C. G. Bright, "Inertia emulation control strategy for vsc-hvdc transmission systems," *Power Systems, IEEE Transactions on*, vol. 28, no. 2, pp. 1277–1287, 2013.

[64] K. Wang, J. Yao, J. Liu, S. Yang, and D. Zeng, "A generalized power control strategy with droop feedback for vsc-hvdc," in *Power and Energy Society General Meeting, 2012 IEEE*. IEEE, 2012, pp. 1–6.

[65] N. Prabhu and K. Padiyar, "Investigation of subsynchronous resonance with vsc-based hvdc transmission systems," *Power Delivery, IEEE Transactions on*, vol. 24, no. 1, pp. 433–440, 2009.

[66] A. Fuchs, S. Mariethoz, M. Larsson, and M. Morari, "Grid stabilization through vsc-hvdc using wide area measurements," in *PowerTech, 2011 IEEE Trondheim*. IEEE, 2011, pp. 1–6.

[67] R. Preece, A. Almutairi, O. Marjanovic, and J. Milanovic, "Damping of electromechanical oscillations by vsc-hvdc active power modulation with supplementary wams based modal lqg controller," in *Power and Energy Society General Meeting, 2011 IEEE*. IEEE, 2011, pp. 1–7.

[68] H. Latorre and M. Ghandhari, "Improvement of power system stability by using a vsc-hvdc," *International Journal of Electrical Power & Energy Systems*, vol. 33, no. 2, pp. 332–339, 2011.

[69] Y. Pipelzadeh, B. Chaudhuri, and T. C. Green, "Control coordination within a vsc hvdc link for power oscillation damping: A robust decentralized approach using homotopy," *Control Systems Technology, IEEE Transactions on*, vol. 21, no. 4, pp. 1270–1279, 2013.

[70] P. W. Sauer and M. Pai, *Power system dynamics and stability*. Prentice Hall Upper Saddle River, NJ, 1998, vol. 4.

[71] O. Urquidez and L. Xie, "Singular value sensitivity based optimal control of embedded vsc-hvdc for steady-state voltage stability enhancement," *Power Systems, IEEE Transactions on*, vol. PP, no. 99, pp. 1–10, 2015.

[72] ERCOT. (2013) ERCOT Operations Report - August 2013 ROS & OWG. [Online]. Available: https://www.ercot.com/

[73] ITC Midwest. (2012) Transmission Planning Criteria - 100kV and Above. [Online]. Available: http://www.itc-holdings.com/itc-midwest/projects/planning-criteria.html